COMPUTATIONAL STUDIES OF C-B BOND FORMATION REACTIONS

Ana Mateo Martínez

UNIVERSITAT ROVIRA i VIRGILI

Computational studies of C-B bond formation reactions

ANA MATEO MARTÍNEZ

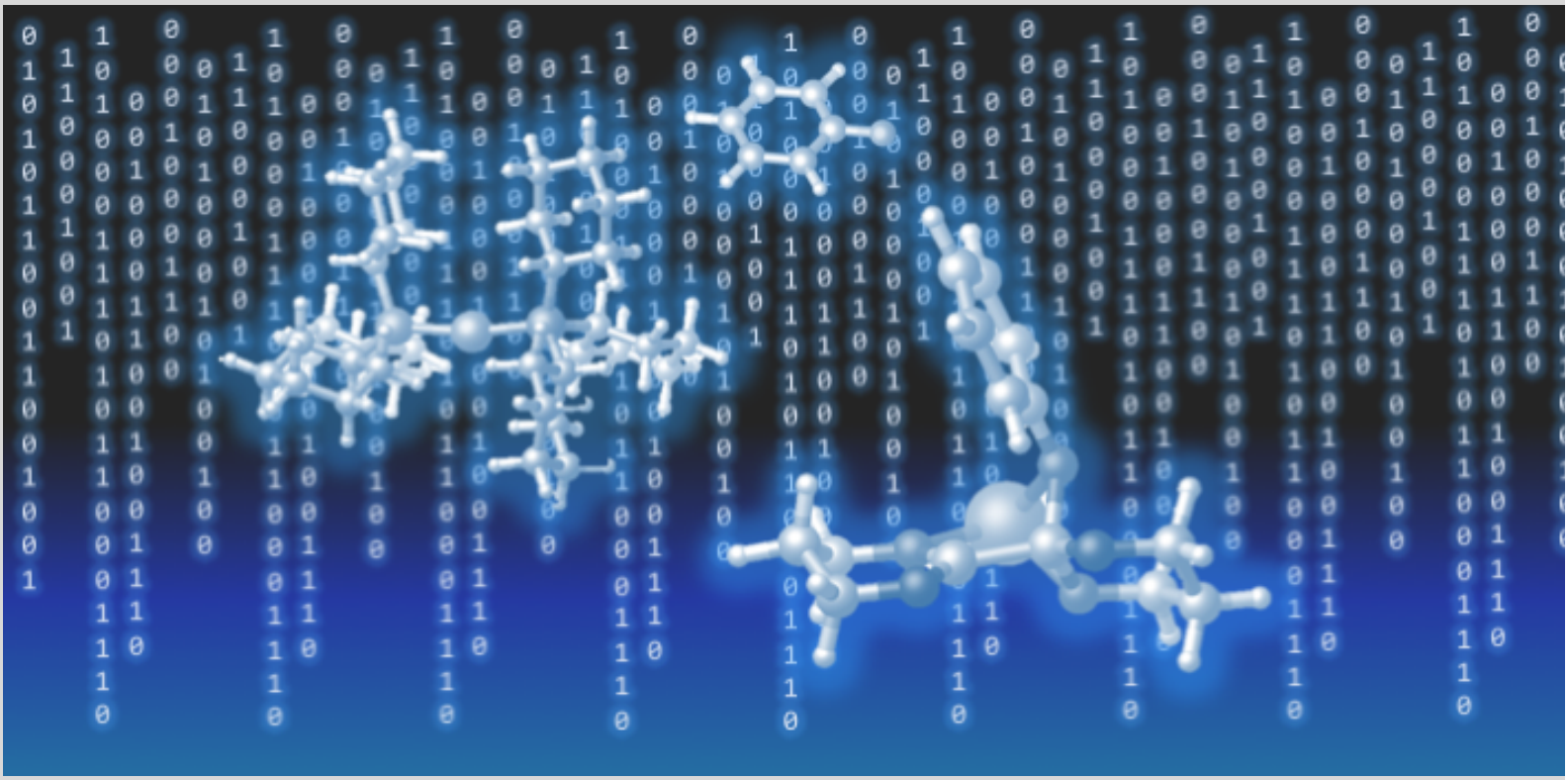

DOCTORAL THESIS
2019

DO

Compu **An**

2018

Ana Mateo Martínez

Computational studies of C-B bond formation reactions

Ph.D. Thesis

Supervised by Dr. Carles Bo Jané

UNIVERSITAT
ROVIRA i VIRGILI

Tarragona

2019

UNIVERSITAT
ROVIRA i VIRGILI

Dr. Carles Bo i Jané, professor titular de Química Física de la URV i investigador a l'Institut Català d'Investigació Química,

FAIG CONSTAR que aquest treball, titulat *"Computational studies of C-B bond formation reactions"*, que presenta Ana Mateo Martínez per a l'obtenció del títol de Doctor, ha estat realitzat sota la meva direcció als laboratoris del meu grup a l'Institut Català d'Investigació Química.

Tarragona, 2 de Setembre de 2019

El director de la tesi doctoral

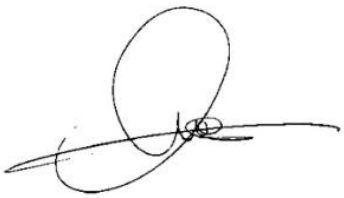

Dr. Carles Bo i Jané

ACKNOWLEDGEMENTS

Primero me gustaría agradecer a Guillermo Carrera, que desde pequeña me animé a seguir una carrera científica, allá dónde estés gracias, esta Tesis es en parte gracias a tus ánimos y hacerme ver que una mujer puede ser una buena investigadora.

También quiero agradecer a mi directora de Tesis de Master Lourdes Vega, que en momentos que yo no confiaba en mi misma me hizo ver que yo era capaz de conseguir el Doctorado. Gracias también a su ejemplo de como una mujer puede combinar perfectamente ser madre, científica y tener éxito.

I com no, a en Carles Bo, el meu director i tutor durant aquesta etapa del PhD. Gràcies per guiar-me i fer-me veure que la feina no és només feina, sinó també treball en grup i fer pinya. Per fer-me descobrir nous skills que no sabia que tenia i potenciar-los. També per ensenyar-me que un bon cap entén els mals moments dels treballadors però sap pressionar en els bons. GRÀCIES!

Però els agraïments no acaben aquí. Aquesta Tesi, ni cap de les dels grups de teòrics, no podria haver estat possible sense els dos pilars del nostre laboratori, el Martin i la Núria Vendrell. Martin gràcies per la teva eterna paciència, per mantenir-nos el clúster viu i arreglar coses que ni tan sols et toca fer-ho a tu. Núria, som les cuquis del laboratori, gràcies per la gran feina que fas i els bons moments que hem passat juntes al laboratori i al Twitter, prometo no aparcar l'alemany.

Vull agrair al Grup Bo, antics i nous. Dolores por enseñarme qué es la sororidad, Nuno i Stefano por ayudarme en mis inicios. Joan per ser company i amic, ajudar-me quan l'he "liat parda",

ensenyar-me sobre el Delta que en aquest tema era una ignorant i ajudar-me amb tota la paperassa de la Tesi. Mire, gràcies per ser tan bona companya, m'emporto una amiga. Enric, gràcies per ajudar-me sobretot amb el Python, que sóc una negada i tu ets un crack! Segueix així, arribaràs lluny. Moisès, gràcies per la paciència que has tingut a l'hora de resoldrem els dubtes del ioChem-BD i ara al final per donar-me un cop de mà amb l'html, sense jo hagués estat perduda. Y el último en llegar, pero no el menos importante Diego, gracias por las sonrisas que regalas, ya he descubierto un eurofan como yo.

Vull agrair els bons moments passats a l'Avant i la furgoneta de l'ICIQ amb els que cada dia veníem de Barcelona: Gabriel, Fernando, Dani, Marçal, Núria, Feliu i Sergio. M'ha encantat les nostres converses, els comentaris de Game of Thrones i quan ens donava per cantar... Gràcies, sense vosaltres aquesta etapa hauria estat molt avorrida.

También quiero agradecer el apoyo al grupo comedor. Los que ya no están, Neyvis, por nuestras conversaciones no científicas y Victor por tu siempre serenidad. Los que continúan, como Marcos, siempre chinchándome, pero gracias por hacerme reír tanto. Y a los que acaban de llegar, los ñus, Lucia, Sara, Jordi, Raul, Andrea y Albert, es muy guay el grupo que habéis formado, es muy importante que sigáis así, os ayudará mucho en los momentos más duros. Y a Ángel, contigo empecé, pero tu seguirás aquí un poco más. Gracias por esta siempre ahí, por escucharme y por hacerme reír.

Ja fora de l'ICIQ, m'agradaria agrair tot el suport i la confiança que m'han donat i han sabut fer-me tocar de peus a terra quan tocava, les Mosqueteres, Montse i Carol, que encara que no parlem diàriament sempre estem disposades a ajudar-nos encara que sigui a distància. I també vull agrair a la resta de grup de químics, Jorge, Alberto, Eloy, Eloi, Albert, Aymà, Joan, Sara, perquè veu fer la carrera molt més lleugera i vam viure i viurem molts bons moments.

Por último, y los más importantes, gracias a mis padres Conchi y Alejandro, por creer en mi, por darme apoyo, por centrarme cuando tocaba, por creer que soy la mejor y la más guapa. Por enseñarme que lo importante es hacer lo que te gusta, que la vida es muy larga para dedicarte a lo que no te gusta. Gracias, os quiero.

Funding Agencies

LIST OF PUBLICATIONS

RELATED WITH THIS THESIS

Tools in ioChem-BD for Studying Chemical Reactivity: Nickel-Catalysed Borylation of C-F Bonds as a Case Study. Mateo, A.; Álvarez, M.; Bo, C. *International Journal of Quatum Chemistry*. **2019.** https://doi.org/10.22541/au.156701017.73932549.

On the Mechanism of the Nickel-Catalyzed Boron insertion into C-O bond of Benzofuran. Mateo, A.; Saito, H.; Hayate, Y.; Bo, C. *Organometallics.* **2019**. https://doi.org/10.26434/chemrxiv.8306057.v1

DFT study of the participation of Copper on Ni -Catalysed Aryl Borylation. Mateo, A.; Bo, C. (*Manuscript in preparation*)

NO RELATED WITH THIS THESIS

Coupling the anionic closodecahydrodecaborate cluster with Anderson-type polyoxometalates: A marriage against nature? Manal Diab, Ana Mateo, Joumada El Cheikh, Mohamed Haouas, Alireza Ranjbari, Flavien Bourdreux, Daoud Naoufal, Emmanuel Cadot,a Carles Bo, Sébastien Floquet. *Dalton Transactions*. (*Submited*).

Wedding of anionic closo-decahydrodecaborate derivative clusters with Keggin and Dawson-type polyoxometalates. Manal Diab, Ana Mateo, Mohamed Haouas, Joumada El Cheikh, Alireza Ranjbari, Vincent Guérineau, David Touboul, Nathalie Leclerc, Zeinab El Hajj, Emmanuel Cadot, Daoud Naoufal, Carles Bo, and Sébastien Floquet. *Chemistry European Journal.* (*Submited*).

Clone-Report: Python code for the automatization of DFT calculations from ioChem-BD. Mateo, A.; Bo C. (*Manuscrip in preparation*).

TABLE OF CONTENTS

ABSTRACT

Fluorine is the 13th most abundant element on earth. Fluorine applications have grown enormously in the last 80 years especially in pharmaceuticals, agrochemicals and materials science.[1] This is a consequence of the special properties of fluorine and its compounds given the strong C-F bond. Because of these properties, chemists are interested in finding ways to form and to cleave, C-F bonds. Regarding the lack reactivity of the C-F bond, finding an economical reaction that could take place under mild conditions to carry out the C-F bond scission is a challenging task. As the same way, scientists are interested in aryl esters as a substituents of aryl halides to avoid fluorine waste and its high availability. As C-F, C-O has low reactivity and it is also challenging find the way for C-O cleavage. Organoboron compounds are also of high interest as intermediate compounds in synthesis, as functional materials, and as bio-agents, that link the C-F bond cleavage through a borylation reaction to obtain compounds with C-B bonds. Further functionalisation of C-B bonds opens a wide range of transformations.

In 2015, Martin and Hosoya groups per separate, present a Nickel catalysed borylation on the aryl C-F bond. And later, Yorimitsu's group present the borylation into a C-O bond of a benzofuran. Since that many scientist present different borylation into C-F or C-O bonds with multiple metal catalyst. This topic is far to be finished an it still awake interest into the scientist. Borylation of C-X bonds is therefore a topic of current interest that makes a computational study attractive. There are plenty of open questions regarding the mechanism, the role of the base, and the reaction conditions.

For this reason, in this Thesis, we present the computational study of borylation of C-F and C-O bonds. Concretely, to the Martin's, Hosoya's and Yorimitsu's reactions. The main objective

is to shed light into the mechanism of the three reactions and find common points for a general explanation.

The first chapter contains the state-of-art of C-X borylations, since the reactions presented by Martin and Hosoya until current days. Additionally, the chapter contains the theory of cross-coupling reactions and the main objectives of the Thesis.

In Chapter 2, we explain the theory of the computational methods used in the thesis. We describe the DFT and how it is used in computational homogeneous catalysis. Moreover, we explain how we can run a kinetical analysis from a DFT study and the different factors that could affect to the rate reaction. Additionally, we explain which information can be taken from DFT and the kinetical analysis of a reaction.

The Chapter 3 presents the results of the computational analysis of the C-F borylation reaction of Martin. The computational study indicates that the reaction follows a modified cross-coupling reaction. The participation of the salt is the key of the reaction, because activates the B-B bond of the diboron reagent and helps the transmetalation step. Moreover, the ligand catalyst, phosphine, due its lability triggers the presence of the mono-phosphine compounds, such that the isomerization is more effective in mono-phosphine compounds.

In Chapter 4, we present the computational study of the reaction presented in the previous chapter. The kinetical study show that the diffusion and competitive reactions are a key for the kinetic analysis. Thanks, to the kinetic study we can see that the bi-phosphine compounds are present in the reaction although, the mono-phosphine compounds present less energetic barriers. Moreover, the study demonstrates that the initial concentration of phosphine modifies considerably the rate reaction because affects the catalyst formation reaction.

Chapter 5 collects the results of the C-F borylation presented by Hosoya in 2015 where it is surprising the presence of the iodine

copper as a reactant. As in Martin reaction, uses the CsF salt that activates the diboron reagent, however it is not clear the role of the copper. The results show that this copper can break the B-B bond and after that it coordinates to the nickel intermediates for make it possible the transmetalation step. The transmetalation without the participation of CuI is not reachable. After that, in this Chapter we present another Hosoya's reaction study, where the nickel is not present as a catalyst and the reaction works with only copper. The computational study refuses the hypothesis of Hosoya and confirms the formation of a Cu^{III} specie after the B-B bond break. This compound with the aryl fluroine can realize a direct transmetalation for the boryl-fluorine exchange.

The Chapter 6 presents computational study the most different reaction a first glance, the borylation into a C2-O bond of a benzofuran. However, the results demonstrate that the reaction follow the basic principal steps of the previous reactions. The participation of the carbonate salt also activates del B-B bond of the diboron reagent. Moreover, the oxidative addition is present in the reaction. However, the transmetalation and the reductive elimination steps change. In the cross-coupling reaction in the trasmetalation step there are a leaving group in that case would the oxygens, but in this reaction the oxygen remains. Additionally, the last step is not a reductive elimination, actually is a boron carbon nucleophilic attack, because the nickel remains with the same oxidation state.

Finally, the last chapter collects the main conclusions of this Thesis: the need of a salt in the presence of diboron reagents in the borylation; the similarities between the C-F and the C-O bonds; and the possibility of use copper based catalyst instead of a nickel catalyst.

"In science, we must be interested in things, not in persons." Marie Skłodowska-Curie

CHAPTER 1

1. INTRODUCTION

1.1. THE IMPORTANCE OF C-F/C-O BONDS

Fluorine is the 13th most abundant element on earth.[1] Fluorine applications have grown enormously in the last 80 years especially in pharmaceuticals, agrochemicals and materials science.[1] This is a consequence of the special properties of fluorine and its compounds given the strong C-F bond. The high availability of fluorine-containing molecules in nature make it attractive for use them as a starting point in organic synthesis. Because of these

features, chemists are interested in finding ways to form and to cleave C-F bonds. Regarding the lack of reactivity of the C-F bond, finding an economical reaction that could take place under mild conditions to carry out the C-F bond scission is a challenging task.

On the same wise, in recent years, C-O electrophiles has arisen as an alternative to aryl halides in cross-coupling reactions.[2–9] Avoid the halogenated waste is one of the reasons for the increasing interest to use them instead of aryl halides. Activated aryl esters, carbamates and sulfonates are commonly used in cross-coupling reactions, however aryl esters are not used as usually as we expect. This is because the lack of reactivity of C-O bond. As C-F bonds, C-O bond cleavage has high activation energy, and consequently, they are not good leaving groups. For these reasons, it is challenging to find ways for the C-O bond scission.

Here comes to play organoboron compounds that are also of high interest as intermediate compounds in synthesis, as functional materials, and as bio-agents.[10] Due its pivotal role, organoboron compounds awake interest in both industrial and academic laboratory as a starting point for synthetic organic chemistry. For this reason, it would be interesting to find C-F bond and C-O bond cleavage reactions through borylation reactions to obtain compounds with C-B bonds. Further functionalisation of C-B bonds opens a wide range of transformations. Organoboron compounds allow to obtain new compounds as new drug candidates and molecular proves. The nickel catalysed borylation reactions of C-F and C-O bonds are an alternative to other borylations on other more reactive aryl-halide bonds.

1.2. BORYLATIONS OF C-F /C-O BONDS FROM ARYL

The Suzuki-Miyaura reaction was the first borylation reaction of an organohalide with a palladium catalyst reported in the year

1979.[11] Akira Suzuki shared the 2010 Nobel Prize in Chemistry with Richard F. Heck and Ei-ichi Negishi for their discovery and development of palladium-catalysed cross-coupling reaction in organic synthesis. The Suzuki-Miyaura reaction is catalysed by a Pd organometallic complex and the reactants are a boronic acid and an organic halide. Suzuki demonstrates that the reaction follows a Cross-Coupling mechanism. This mechanism consists in three steps: oxidative addition, transmetalation and reductive elimination. We will go into details in section 1.3.

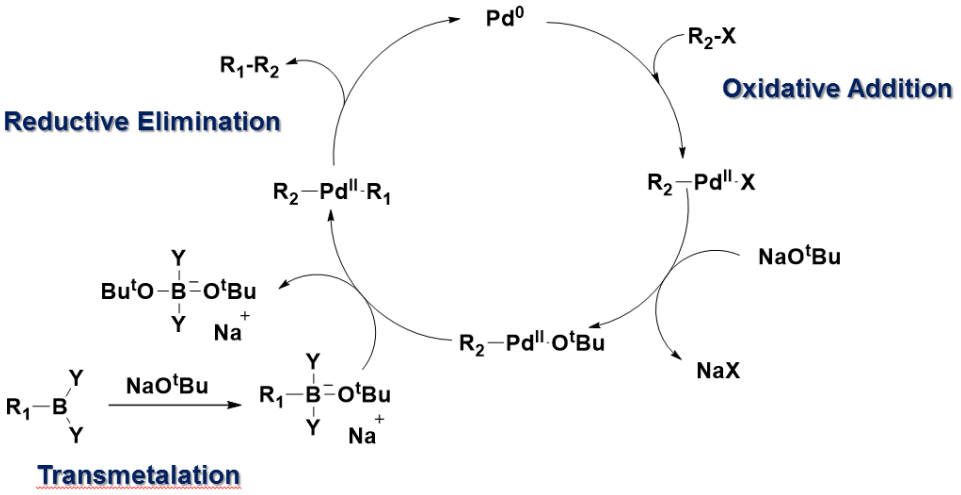

Figure 1-1. Suzuki-Miyaura Reaction.[12]

The main limitation of the Suzuki-Miyaura reaction is the low availability and the high cost of Palladium,[13] which challenged scientists to explore other metals in order to make the reaction more sustainable and cost-effective. Finding cheap metals as a catalyst is more challenging because the selectivity of this cheap metals is not as good as with palladium catalysts. Moreover, cheap metal catalysts are less tolerant to functional groups and reactants. Additionally, Palladium based catalysts work with a wide range of starting molecules. It was cost-effective found cheap metal catalyst that works for both borylation of C-F and of C-O bond in aryls.

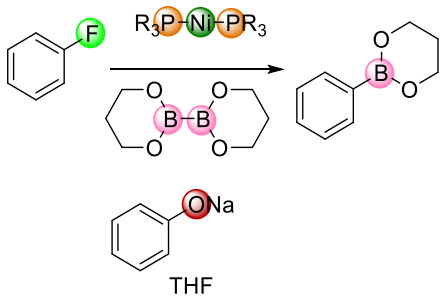

Figure 1-2. Martin's reaction.

In this sense, on the same day in 2015, August 2nd, both Martin's and Hosoya's groups independently reported to the Journal of the American Chemical Society on a novel borylation reaction of aryl fluorides catalysed by a nickel/phosphine complex [$Ni(PCy_3)_2$]. Martin's group used B_2nep_2 as the boron agent and the reaction was assisted by NaOPh salt in Tetrahydrofuran (THF) at 110ºC[14] (Figure 1-2). On the other hand, Hosoya's group used B_2pin_2 as borylation agent, assisted by CsF and CuI salts, with toluene as solvent, and they achieved good yields at lower temperature 80ºC[15] (Figure 1-3). A few months later, Radius and Marder's group presented the borylation of aryl fluorides catalysed by a nickel catalyst also, but with a carbene (IMes) ligand instead of the phosphine, with B_2pin_2 as the diboron, assisted by CsF and NMe_4F salts, in THF as solvent at 80ºC.[16]

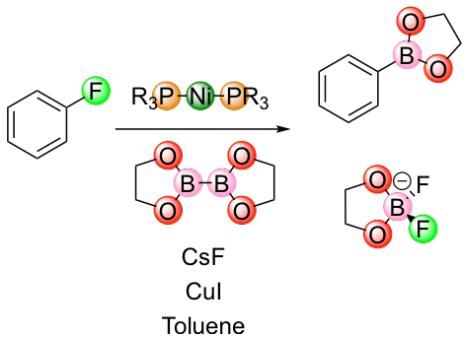

Figure 1-3. Hosoya's reaction

It is worth highlighting that Martin's group[17] had previously reported that, under the same reaction conditions, aryl ethers could be borylated with B_2nep_2 via C-O bond cleavage. Indeed, Yorimitsu and coworkers[18] found later that this chemistry could be also applied to obtain organoboron compounds by activating the C-O bond in benzofuran: the catalyst could break the heterocyclic C-O bond and insert one boron from B_2pin_2 by using a nickel/carbene(IMes) catalyst assisted by the base Cs_2CO_3 (Figure 1-4).

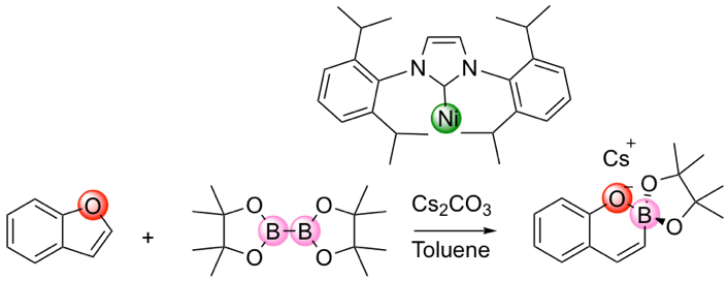

Figure 1-4. Yorimitsu's reaction.

At this stage, it is noteworthy that C-F and C-O bonds can undergo similar transformations regarding borylation reactions when they are exposed to that unique catalyst, diboron agent and base/salt combination. Note that the diboron agent, the ligand of the nickel catalyst, and the base allow for some variations, and are the key reactants for the C-F/C-O cleavage although no clear explanation as to why those combinations has been provided yet. For instance, the activity or inactivity of boron agents, and the role of the salt and of the solvent are aspects that are not yet fully understood.

This chemistry is far from being fully explored and still awakens interest nowadays. Several research groups are currently trying to develop C-X (X= F, Cl, Br, I, O, S) borylation reactions by exploring different metals and different ligands, the scope of substrates, and different reactions conditions to obtain good yields in milder

conditions. Table 1 collects the latest new borylation reactions of aryl halides and aryl ethers that have been reported over the last years.

Table 1 C-X borylation reactions catalysed by metal catalyst (ML) and assisted by a base or a salt from 2015 until now.

	M	L	C-X	Boron	Base	Solvent	T(°C)
Zarate 2015	Ni	PCy_3	C-O	B_2nep_2	HCO_2Na	PhMe	95
Liu 2015	Ni	PCy_3	C-F	B_2nep_2	NaOPh	THF	110
Niwa 2015	Ni	PCy_3	C-F	B_2pin_2	CsF / CuI	toluene	80
Zhou 2016	Ni	IMes (NHC)	C-F	B_2pin_2	CsF / NMe_4F	THF	80
Saito 2016	Ni	IPr (NHC)	C-O	B_2pin_2	Cs_2CO_3	toluene	100
Zhang 2017	Cu	Xantphos	C-F (alkenes)	B_2pin_2	NaO^{t}Bu	DMF	room
Niwa 2017	Cu	PCy_3	C-F	B_2pin_2	CsF	Toluene	80
Lee 2017	Free	Free	C-I	Bpin-R-Bpin	NaO^{t}Bu	toluene/THF	120
Sakaguchi 2017	Cu	PCy_3	C-F	B_2pin_2 / B_2nep_2	KOAc	THF	40
Schwarzer 2017	Ni	PCy_3, ICy	C-O	Aryl-boronic ester	CsF	toluene	120
Lim 2018	Co	β-diketiminate	C-F	HBpin	Mg?	THF	60
Zhao 2018	Pd or Fe	dba(Pd) or Cl (Fe)	C-F	B_2pin_2	LiHMDS	toluene	80
Tian 2018	Rh/Ni	Imes (NHC)	C-F	B_2pin_2	CsF	photocatalytic	25
Minami 2018	Pd	OAc	C-S	B_2pin_2	K_3PO_4	THF	80
Verma 2018	Co	Imes (NHC)	C-Cl / C-Br	B_2pin_2	KOMe	MTBE	50
Hu 2018	Cu	Xantphos	C-F	B_2pin_2	LiOMe	THF	40
Kuehn 2019	Ni	ICy (NHC)	C-Cl	B_2pin_2 / B_2neop_2	NaOAc	Mecyclohexane	100
Lu 2019	Ag	$OOCF_5C_2$	C-O	B_2pin_2	LiO^{t}Bu	1,4-dioxane	60

Copper, firstly introduced by Niwa[19] in the form of CuI with the nickel/phosphine/CsF system, was found to be active by itself. Hosoya's group reported that the reaction with copper(I) assisted by CsF only needed lower temperature, and that it worked with both B_2pin_2 and B_2nep_2 diboron reagents, using KOAc in THF.[20] Cao and coworkers presented a C-F bond cleavage of alkene halides using a copper(I) catalyst with a Xantphos ligand, with B_2pin_2 as a diboron agent, and assisted by tert-butoxide salts at room temperature.[21]

Few computational studies on related systems have been carried out.[9,22–28] Mori's group presented a combined experimental and computational study on the C-O bond cleavage borylation reaction of aryl-boronic ester, using a nickel catalyst assisted by CsF.[29] A related case is the metal-free borylation of aryl and vinyl halides with 1,1-Bis[(pinacolato)boryl]alkanes.[30] It must be said

that this C-I bond cleavage, which is the weakest of all aryl halide bonds, additionally required high temperatures (120°C).

Borylation reactions via C-F bond cleavage with a wide range of metals have been reported very recently. All these reactions require lower reaction temperatures than those indicated in Table 1. Lee's group showed that a cobalt catalyst with a β-diketiminate ligand can activate the HBpin boron agent.[31] Cao's group performed another C-F borylation that uses a two metal-catalyst system, palladium with dba ligand and iron tricloride, the boron agent was B_2pin_2, and assisted by LiHMDS in toluene at 80°C. Another example is the photocatalic C-F scission described by Marder and Radius, in which they combined a nickel/carbene catalyst with rhodium for the borylation with B_2pin_2 and CsF at 25°C. Finally, Shi's group used a similar procedure to Cao's in 2017 to cleave the C-F bond cleavage of alkene fluorides with a copper/Xantphos catalyst, B_2pin_2 and LiOMe as base, in THF at 40°C.

C-Cl, C-Br and C-S bonds can also undergo borylation reactions under very similar procedures.[32,33]So far this year, we have found two contributions on this topic. In the first one, the C-Cl bond is cleaved with a nickel catalyst, borylated with B_2pin_2 or B_2neop_2, and assisted by a NaOAc base in methylcyclohexane at 100°C.[34] In the other case, the C-O bond borylation is carried out with a silver catalyst, B_2pin_2, and tert-butoxide salts in 1,4-dioxane at 60°C.[35]

Borylation of C-X bonds is therefore a topic of current interest that makes a computational study attractive. There are plenty of open questions regarding the mechanism, the role of the base, and the reaction conditions. A good starting point for the study of this reactions is the cross-coupling mechanism explanation because as we explained before, borylation of C-X bonds are similar to Suzuki-Miyaura reaction. [11] We explain bellow extensively the cross-coupling reaction mechanism in detail.

1.3. CROSS-COUPLING REACTIONS

All the reactions for the Borylation of C-X bonds are homogeneous catalytic reactions. A homogeneous catalytic reaction is a chemistry process catalysed by a soluble catalyst. They are called homogeneous because catalyst and reactants are in the same phase, usually liquid phase. Due the Borylation of C-X bonds are similar to Miyaura reaction,[11] we would describe it as a cross-coupling reaction. The cross-coupling mechanism consists in the exchange of two fragments (**X** and **Y** in Figure 1-5) between two different reactants (**R-X** and **R'-Y**) assisted by a metal complex **ML_2** as catalyst. Figure 1-5 shows the scheme of the classical cross-coupling reaction mechanism that comprises three main steps. These steps are: oxidative addition, transmetalation and reductive elimination.

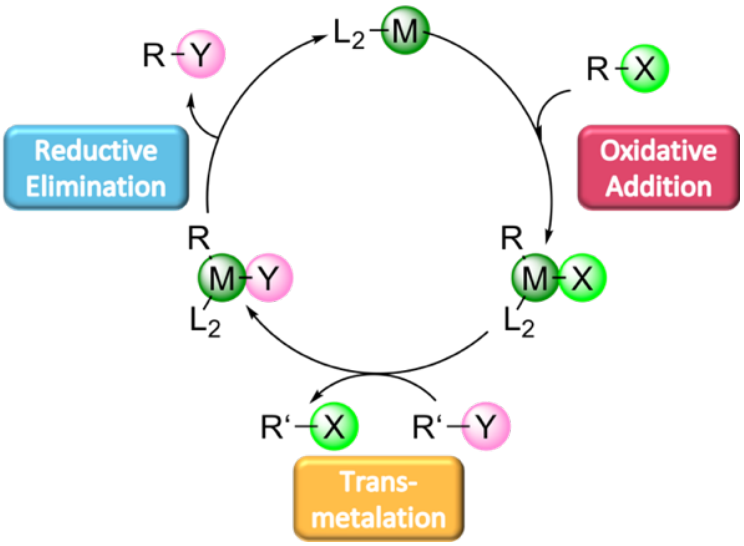

Figure 1-5. Classical Cross-Coupling mechanism scheme.

The first step, the oxidative addition, is the linkage between a molecule of one reactant **R-X** and the catalyst. At this step the catalyst is oxidized and the **R-X** bond in the reactant molecule is broken. The next step is the one where the second reactant **R'-Y**

reacts with the intermediate exchanging substituents. At this step we obtain a sub-product of the reaction, **R'-X**. Finally, the reductive elimination takes place, the catalyst is reduced and goes back to its initial configuration, and we obtain the desired product **R-Y**.

The main participants in a cross-coupling reaction are three, the two reactants and the catalyst. However, the C-X borylations mentioned above, they have an additional participant, the base. This fact makes us suspect that these reactions are quite more sophisticated than classical cross-coupling reactions. For this reason, it is of interest the study of this reactions, to know how they works.

The study of this reactions experimentally is quite difficult due to the practically impossible isolate each intermediate of each catalytic step. Here comes into play computational chemistry. In the recent years, computational chemistry has become a key tool for the study of homogenous catalysis reactions. The classical procedure for its computational study is via Density Functional Theory (DFT). DFT calculations allow us to determine the electronic structure of each reactant, product, intermediates and transition states (TS) and the corresponding energy. With the energy of each element in the catalytic cycle we can construct the potential energy surface and, evaluating it determine which is the most efficient mechanism for the reaction. Moreover, with DFT studies we can obtain different properties of the system: topological analysis, charge analysis, etc. More recently, some computational scientists demonstrates that a kinetic study of a reaction could give more information of the system.[36] These topics will be further explained in the next Chapter.

Borylation of C-X bonds is therefore a topic of current interest that makes a computational study attractive. There are plenty of open questions regarding the mechanism, the role of the base, and the reaction conditions. This Thesis aims at unravelling computationally the atomistic details that those reactions have in

common, and at finding general rules to understand this reactivity. Concretely, we will shed in light into the mechanism of the Martin[14], Hosoya[15] and Yorimitsu[18] reactions.

1.4. AIMS AND OBJECTIVES

The main goal of this Thesis is to investigate computationally the mechanistic pathways of C-B bond forming reactions. Concretely, in this Thesis we study the borylation of C-O and C-F bonds with Ni and Cu catalysts. Next, we will summarize the objectives of each chapter of the Thesis.

In Chapter 3 we will study computationally the aryl C-F cleavage with a nickel catalyst assisted by sodium phenolate and a diboron. One of the goals of this Chapter is finding the role that the sodium phenolate plays and how it modifies the classical cross-coupling mechanism. The second objective is to investigate the relevance of the relative presence of mono-phosphine and bi-phosphine compounds in the mechanism, how affects the thermochemistry and the kinetics of the reaction.

In Chapter 4, we present a detailed kinetical analysis of the reaction presented in Chapter 3. The main goal in this Chapter is to go one step further the classical computational study and obtain more information about this reactive system by using kinetic modelling. We want to investigate how diffusion, competitive reactions and different initial concentrations affect the reaction rates. The objective of the kinetic study is also to investigate the need to include off-cycle reactions in the kinetic models, such are the mono-phosphine/bi-phosphine exchange processes, in order to get better agreement with experiments.

Chapter 5 details the computational study of the C-F bond cleavage with a nickel catalyst assisted by a CsF and CuI, a very similar process to that studied in Chapter 3. As in the previous Chapter, the objective is finding the role of the additives in the catalytic process, in this case iodine copper and the caesium

fluorine. The objective is demonstrating that the caesium fluoride activates the diboron agent. Moreover, we aim at proving whether copper complexes may be the real catalyst.

The last chapter, Chapter 6, we present the computational study of the borylation of benzofuran into C2-O bond assisted by Na_2CO_3. This is a different reaction, but similar to the C-F borylations also presented in this Thesis. The main objective in this chapter is demonstrating that C-O and C-F bonds present similar reactivity under particular reaction conditions. As Chapter 3 and Chapter 5, the goal in this chapter is to determine the role of the salt Na_2CO_3, whether it can activate the diboron reagent modifying the classical cross-coupling reaction mechanism. This chapter has an additional objective, which is to demonstrate that, after the oxidative addition, the next steps are intramolecular reactions. As intramolecular reactions, there is not a leaving group, therefore there is no transmetalation step, and only a simple boryl transfer takes place. Moreover, the nature of the reductive elimination, the final step, is interesting to study since a priopi it seems more a nucleophilic attack than a reductive process,

"Don't spend time beating on a wall, hoping to transform it into a door." Coco Chanel

CHAPTER 2

2. COMPUTATIONAL METHODS IN CATALYSIS

2.1. INTRODUCTION

"Homogeneous catalysis, by definition, refers to a catalytic system in which the substrates for a reaction and the catalyst components are brought together in one phase, most often the liquid phase."[37]

In the past few years, computational chemistry has become a key tool for the study of many chemical processes. Catalysis is one of the fields where computational chemistry has improved its application, by obtaining relevant results. Computational

chemistry is a useful tool to unravel reaction mechanisms. Thanks to computational methods we are able to analyse each step of the mechanism and define with enough accuracy the reaction pathway. Moreover, these tools allow us to reproduce experimental results and understand the role that plays the catalyst in the reaction. In the long run, we are able to predict the experimental results and select the best/more suitable catalyst.

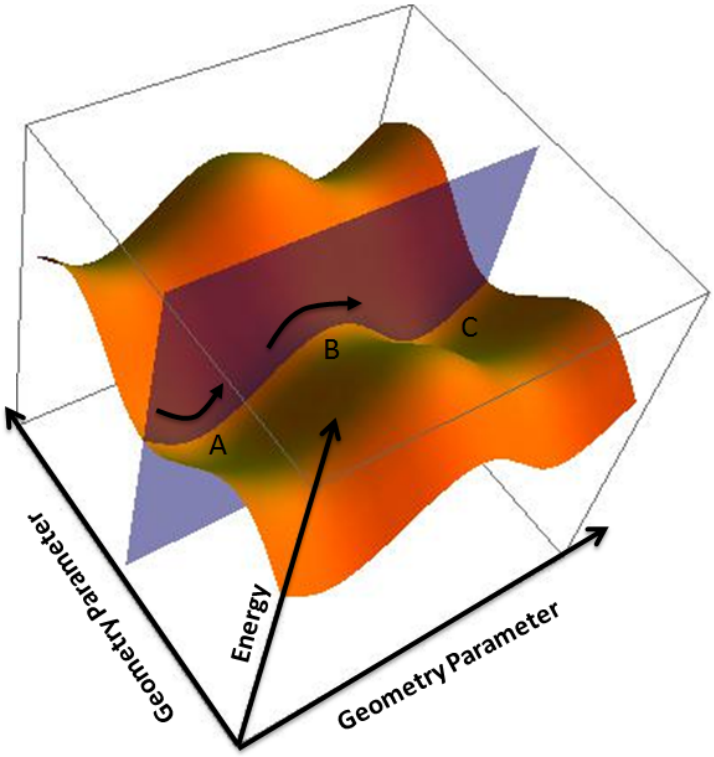

Figure 2-1. An example of Potential Energy Surface. Taken from Creative Commons.[38]

The comprehension of reactivity requires exploring of the potential energy field that governs the evolution of the molecular geometry. Separation of the electronic and nuclear motions within the Born-Oppenheimer (BO) approximation leads to the natural appearance of the potential field. These surfaces are called Potential Energy Surfaces (PES). The PES is probably one of the major achievements of the BO approximation, because many chemical processes can be rationalized in terms of minima,

transitions states (TS) and products. These PES allows us to compare the different possible pathways for a catalytic cycle and decide which one is the most favoured. Figure 2-1 depicts a simple example of a PES, where it can be observed the mechanism of less energy and goes from the intermediate A to intermediate C through transition state B. In this surface, we can observe that there are other possible ways that the reaction can follow. These alternative paths have to be taken into account because they can affect the evolution of the catalytic cycle. These facts will be discussed below in section 2.3.2.

2.2. DENSITY FUNCTIONAL THEORY

Homogeneous catalysis reactions are studied computationally by determining the substrates, the products, the intermediates and the transition states (TS) using electronic structure methods. Nowadays, the most popular way to achieve this is by using Density Functional Theory (DFT) based methods.[39] DFT-based methods describe the system by its electron density as the Hohenberg & Kohn theorem[40] states; the electron density determines all properties of the system.

However, this theorem does not give the solution on how to construct the functional of the ground state energy. For this reason, Kohn & Sham formalism[41] proposed a non-interacting reference system built by a set of orbitals which its kinetic energy can be calculated with accuracy, so the energy can be determined by an approximation of a functional with the Kohn & Sham equations. The accuracy of density functional approach depends of the chosen approximation for the exchange-correlation functional. It is where local density approximation (LDA) comes into play: where the functional depends only on the electron density. In general, LDA gives good results for structure properties, however, overestimates the binding energy. For this reason, the generalized gradient approximation (GGA) development changes the situation for the study of chemical reactions, because gives better results for the energy

determination compared to LDA. Examples of GGA functionals are the PBE and BP86. The hybrid-GGA functionals improve the results because combines the exchange-correlation terms from GGA with the Hartree-Fock exchange. An example of this type of functionals is the well-known B3LYP,[42–44] which is the most popular hybrid-GGA. Newly, Truhlar and co-workers developed a family of meta-hybrid functionals called Minnesota functionals, which its use has been growing in the last years. Examples of Minnesota functionals are M06, M06-2X, M05, etc.

2.2.1. Empirical Dispersion Corrections

An alternative for improving functionals is the use of empirical dispersion correction (DFT-D). Dispersion energy is a long-ranged electron correlation effect that contemplates the short-medium interatomic distances, London dispersion energies between the nearly non-bonded atoms in a molecule. It is crucial to compute the non-bonding interactions between atoms. On the one hand, there are functionals that not consider dispersion corrections. These corrections can be added with the dispersion correction developed by Grimme that is added as an additional term in the final energy. On the other hand, there are functionals with implicit dispersion corrections as the mentioned M06 or M06-2X, as well, ωB97XD functional.[45]

2.2.2. Model of Solvation Effects

Homogeneous catalytic reactions occur in condensed phase, and solute-solvent interactions can have a dramatic effect in molecular properties. There are computational strategies to allow the use of electronic methods with models of solvation. In this work we have used a continuum model of solvation in conjunction with density functional based methods.

Polarizable continuum model (PCM)[46] is a commonly used method for considering solvation effects. The molecular free-energy of solvation is computed with the Poisson-Boltzmann

equation as the sum of three terms: electrostatic, dispersion-repulsion and cavitation. This method creates the solute cavity via a set of overlapping spheres. Another option for considering solvation effects is the Solvation Model based on Density (SMD)[47] which solves the Poisson-Boltzmann equation analogously to PCM, but does so using a set of specifically parametrised radii which construct the cavity.

In this Thesis, we have used the hybrid-GGA B3LYP functional with Grimme's dispersion correction (D3), the meta-hybrid M06-2X and the long-range corrected hybrid functional ωB97XD. B3LYP, provably, is the most used functional. It was proposed by Becke for a parameterized hybrid approximation involving the Perdew correlation functional, which lately was substituted by the LYP correlation functional. B3LYP has not implicit dispersion correction, however, M06-2X and ωB97XD have implicit dispersion corrections. M06-2X is one of the meta-hybrid-GGA functional developed by Truhlar, who, as we mentioned before, develop the called Minnesota functionals. These functionals are constructed by empirically fitting their parameters, while being constrained to a uniform electron gas. ωB97XD is a long-range corrected functional that is a subgroup of hybrid functionals as B3LYP. This long-range functionals contemplates the HF short-range contribution as hybrid functionals and include the HF long-range contribution, concretely, G2 in ωB97XD functional.

Moreover, all the calculations presented in this thesis consider solvation effects using the SMD model.[47] Along this Thesis we have compared the three functionals, in order to optimize which one describes more accurately each system under study.

Until now, the energies obtained are calculated with DFT-based methods. However, different molecular properties can be determined from DFT electron density. In the following lines we will focus on the properties studied in this Thesis.

2.2.3. TOPOLOGICAL ANALYSIS WITH DFT

From electron density we are able to construct the electron density map (ρ) of a molecule. This map gives information about the bond's nature of the molecule. Thanks to the Laplacian of the electron density we can observe the bonding and non-bonding interaction between atoms. The Laplacian of the electron density is the scalar derivative of the gradient vector field of the charge density, the quantity $\nabla^2\rho$, and indicates where the charge is concentrated, $\nabla^2\rho<0$, and depleted, $\nabla^2\rho>0$, the local charge concentrations providing a map of the electron pairs of Lewis model.

Here is another way for the analysis of the structure introduced by Bader[48] with its topological analysis of the electron density. In this analysis, the eigenvalues and eigenvectors of the Hessian of the electron density at the critical point permits its characterization. By this way, we found absolute maxima critical points CP (3,-3) for the atoms, the saddle point (3,-1) corresponds to a bond; the (3,+1) critical points correspond to rings in the molecule; and absolute minimum CP (3,+3) indicate the presence of a cage.

In addition, the non-bonding interactions could be analysed thanks to noncovalent interactions (NCI) theory introduced by Yang and collaborators.[49] The areas of NCI can be recognized by a low value of the electron density and a negative (or a small positive) value of the second eigenvalue of the Hessian of the electron density. The regions of significant hydrogen bonding are recognized by strictly negative, while in the regions of Van der Walls (VdW) interactions it may be slightly positive.

2.2.4. CHARGE ANALYSIS

With the DFT calculations we are able to do a charge analysis of a system. In this Thesis, we use the Mulliken population analysis[50] and Natural Bond Orbitals (NBO) analysis[51]. While Mulliken population analysis provide a mean of estimating partial

atomic charges, NBO analysis concerns with the distribution of electrons into atomic and molecular orbitals, and thus with the derivation of atomic charges and molecular bonds. Two analysis derive from NBO method; the natural population analysis (NPA) is used for assignment of atomic charges. In Chapter 7 we have use NPA and Mulliken population analysis for analysis of the charge system.

2.3. MICROKINETIC ANALYSIS

As mentioned in the introduction of this Chapter, in Computational Homogeneous Catalysis, the classical way of studying a reaction is through the calculation of the energy of reactants, products, all possible intermediates, and the corresponding TS for each single chemical transformation, so for each reaction step. The connections between species define the reaction mechanism, or in other words, the reaction map or the PES as we mentioned in the introduction. As it was exemplified by Besora et al.[36] in a recent review, further kinetic modelling provides additional insight and understanding. After a reaction mechanism has been proposed, running a kinetic analysis could be considered as a stress-test for the mechanism. Those authors[36] showed that micro-kinetic modelling could be implemented from static DFT-based calculations and using the Eyring equation.

The Eyring Equation permits to obtain the kinetic constant of each single reaction step, and it can be calculated easily with the activation energy of each reaction step from previously constructed reaction mechanism.

$$k_i = \frac{\kappa k_B T}{h} e^{-\frac{\Delta G^{\ddagger}}{RT}} \qquad \textit{Eq. 1}$$

In the Eyring Equation (Eq. 1), k_i is the kinetic constant, κ corresponds to the transmission coefficient (usually set to 1), k_B is the Boltzman's constant, T refers to the temperature in K, and h is the Plank's constant. Additionally, $\Delta G^{\ddagger}$ is the Gibbs activation energy, which is the difference in energy between an intermediate

and the next corresponding TS, and *R* is the ideal gas constant. Then, given that we obtained all the relative barriers ($\Delta G^{\ddagger}$) for our mechanism, we can solve the Eyring equation and obtain the rate constants for each of the steps of the reaction mechanism. This could be a good procedure for mechanisms, where we have all the TS barriers. However, sometimes there are other issues that could affect the reaction rate, as the diffusion and the presence of competitive reactions.

2.3.1. Diffusion Effects in Rate Reaction

It is important to mention that, in bimolecular reactions, diffusion may be a key component of the rate of a reaction, especially in very fast bimolecular reactions. As an example of diffusion-controlled reactions are the well-known S_N2-type reaction mechanisms. Probably, the first person who observed this effect was Smoluchowski,[52] in his experiments with colloidal aggregations, noted that, in fast reactions, the diffusion can limit the rate. Smoluchowski study is discussed below. For this reason, given that in our kinetic study the overall computed rate was much larger than the experimental value, we thought in applying corrections for diffusion in the barrier-less and fast bi-molecular elemental steps. A reaction is usually considered fast when its rate constant is larger than 10^8.[53–56]

To include diffusion effects, we need to quantify the approximation rate for the two molecules involved. This is achieved by the *encounter ion model,* which introduces the following equation:

$$\frac{1}{k_{app,+}} = \frac{1}{k_+} + \frac{1}{k_{diff}} \qquad \textit{Eq. 2}$$

where $k_{app,+}$ is the apparent rate constant, in which we add the diffusion effects k_{diff} and the rate constant $k_{+,}$ which was calculated with the Eyring equation (Eq. 1) above. *kdiff* constant can be calculated thanks to Smoluchowski's equation, which was

obtained from its experimental observations that we mentioned before:

$$k_{diff} = 4\pi N_A \sigma D_{i,j} \qquad \textit{Eq. 3}$$

Smoluchowski's equation implies that the diffusion constant is directly proportional to the diffusion coefficient ($D_{i,j}$), while σ is the encounter distance between the two atoms that are reacting in the Transition State (TS). The diffusion coefficient can be easily calculated from the self-diffusion coefficients of species *i* and *j*, by using the equation:

$$D_{i,j} = \frac{D_{i,solv} D_{j,solv}}{D_{solv,solv}} \qquad \textit{Eq. 4}$$

where $D_{i,solv}$ is the self-diffusion coefficient of the first reactant (i) in the solvent (solv), $D_{j,solv}$ corresponds to the self-diffusion coefficient of the second reactant (j) in solvent (solv), and $D_{solv,solv}$ is the self-diffusion coefficient of the solvent (solv) itself. The self-diffusion coefficient can be obtained by several means. The first one, and the most used, is from the slope of Mean Square Displacement (MSD) function versus time obtained in a molecular dynamics (MD) simulation.

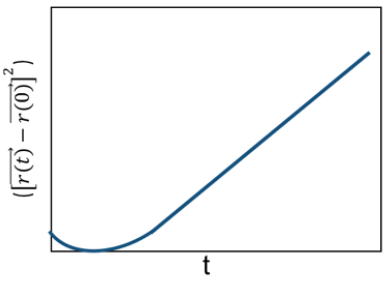

$$D_{i,solv} = \frac{1}{6} \lim_{t \to 0} \frac{d}{dt} \left(\left[\overrightarrow{r(t)} - \overrightarrow{r(0)} \right]^2 \right)$$

Figure 2-2. Mean Square Displacement versus time and the expression of the self-diffusion coefficient.

As showed in Figure 2-2, at short simulation times, the MSD graph refers to the time needed to achieve the thermal equilibrium, and that has nothing to do with diffusion. After that period, the MSD becomes linear with time, then, the graph describes the diffusion phenomena. So, the self-diffusion coefficient is the slope of the MSD function versus time at long simulation times.

The other way for obtaining the self-diffusion coefficient of a molecular system is by solving the Stokes-Einstein equation:

$$D_{i/solv} = \frac{k_B T}{6\pi\eta R} \qquad \textit{Eq. 5}$$

where the k_B is the Boltzmann's constant, T the temperature, R the so-called hydrodynamic radius of the molecule, and η is the viscosity constant of the solvent. With this equation, we can calculate the self-diffusion coefficient without the need to run any MD simulation, but we need the radius R of the molecule.

2.3.2. Competitive Reaction Effects in Kinetics

As mentioned above, diffusion could modify the reaction rate, however the competitive reaction could affect too. In a DFT study we found the most efficient mechanism, however other possible mechanisms could take part in the reaction as competitive reactions, thus modifying the global reaction rate. When we add new reactions in our system, the system becomes more sophisticated and checking how the species are interconnected could be tedious. A good way for visualizing the complication of the system and its species interconnection is the use of a Chemical Reaction Network (CRN), in which we can represent all species that participate in the system as well as the connections between them. This is not only a good way to see the reaction map, but also a good way for automatizing the kinetic simulations.

Once we have calculated all the rate constants of the different elemental reactions of our system, is time to write a script to solve the corresponding differential equations. Luckily, there are many

available software packages that solve these differential equations. The advantages of using these packages is avoid the programming errors when we are constructing the script and save time computing. We have proven two of these packages, Tenua[57] and Copasi[58]. The Tenua package is very easy to operate, however, it can get slow for sophisticated mechanisms, when we contemplate competitive reactions, as we mentioned above. Copasi is fast and offers different mathematical options for the solution of the system of equations. As weak points, the set-up may be rather slow for new users unlike Tenua.

Current investigations aim to automatise the reaction networks because most of the reactions catalysed homogeneously have large reaction networks.[59–62] The research in this topic is growing and it awakens interest nowadays.

In 2015, Professor Martínez-Núñez design a software package[59] that automatically find the transition states (TSs) of a molecular system, with an IRC search the calculations and construct the CRN that can be used for the kinetic analysis. Later, Morokuma's group develop the artificial force induces reaction (AFIR),[60] which locates the local minima and the TSs of a reaction without the need of a scientist guess, therefore finds reactions that could guessed by scientist and other that are unexpected. In the same year, the Zimmerman group's most recent reaction exploration tool, ZStruct2[61], combinatorically samples driving coordinates (DC), which are bond-addition or bond-breaking vectors that describe elementary reactions. More recently, Wheeler group presents An Automated Reaction Optimizer for New catalysts (AARON)[62] that generates automatically initial TS structures based on a library of TS templates. It optimizes the corresponding TS and after that, find the corresponding local minima.

It is clear, automated finding mechanism is a topic growing thanks to the improvements in computational sources and for this reason awakens interest in computational scientists.

"I don't believe in collective guilt, but I do believe in collective responsibility."
Audrey Hepburn

CHAPTER 3

3. *NI-CATALYSED ARYL BORYLATION*

3.1. INTRODUCTION

Aryl fluorides have the strongest C-heteroatom single bond in nature. The strength of the C-F bond arises from the small size and high electronegativity of the fluorine atom that makes fluorocarbons less reactive. This lack of reactivity[63] is the most relevant and characteristic chemical property of fluorocarbons. Remarkably aryl fluorides show an extraordinary metabolic activity, and this makes them especially attractive in the

pharmaceutical industry.[64] Replacement of hydrogen by fluorine in organic molecules can lead to useful pharmaceuticals and agricultural chemicals. The role of fluorine in medicinal chemistry has been reviewed recently,[64] and shows a wide variety of new drugs containing aryl fluorine or $-CF_3$ groups.

All these facts encouraged chemists to design catalytic C-F bond forming, but also bond cleavage, protocols. Very recently, Martin's[14] and Hosoya's groups reported an efficient C-F bond cleavage reaction via Ni-catalyst borylation, incited by the versatility and pivotal role of organoboron reagents (Figure 3-1). Posteriorly, other groups present different variations of borylations testing different salts, catalyst, ligand and different diboron agents.[18–21,29–31,65] Borylation of C-X bonds is therefore a topic of current interest that makes a computational study attractive. There are plenty of open questions regarding the mechanism, the role of the base, and the reaction conditions.

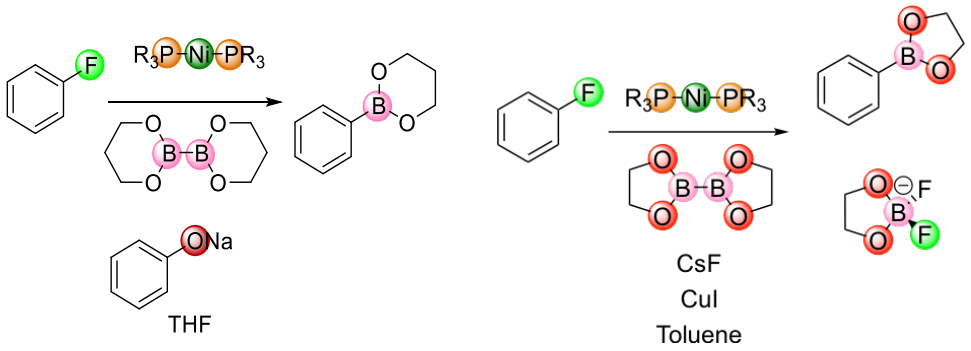

Figure 3-1. Scheme of the Martin (left) and Hosoya (right) reactions.

It was proposed that Martin's reaction follows a classical cross-coupling mechanism, as rational explanation for the products obtained. Cross-coupling reactions are processes in which two reactants, usually holding an activating group, react together with the aid of a metal catalyst.[37] This mechanism comprises three elementary steps: oxidative addition, in which one of the reactants react with the metal atom, which undergoes a formal 2-electrons

oxidation; transmetalation, where the second reactant exchanges with the activating group and adds itself to the catalyst; and finally in the reductive elimination the product is formed, and the catalyst recovered.

However, what surprises the most in the reactions in Figure 1 is the critical presence of a base, such is sodium phenolate, which a priory has any role in the mechanism. Thus, the participation of the diborane reagent and a base made us to think in the possibility of a more complex mechanism in which the base plays some role. Herein we present a detailed computational study aiming to shed light into the mechanism of this reaction.

3.2. COMPUTATIONAL DETAILS

All the calculations in this chapter were carried out using the Gaussian09[66] program package revision D.01. Several Density Functional Theory (DFT) based methods were used: the range separated functional ωB97XD[45] was used as primary method. All the geometry optimizations, harmonic vibrational frequencies and energies were calculated using the 6-311G** basis set[67] for C, H, B, O, F and N atoms; for Ni and Cs atoms we used the LANL2DZ basis set[67], which includes the corresponding effective core potentials. The SMD[47] solvent model was chosen to include THF solvent effects implicitly. Thermal and entropic corrections were evaluated at 298K. Also, we used M06-2X[68] and B3LYP[43,44,69] functional with Grimme's empirical dispersion corrections D3[70] (B3LYP-D3) to compare with ωB97XD[45] . In all the calculations we included entropy corrections as introduced by Martin.[71] IRC calculations were carried out to verify the nature of all the TSs structures. A data set collection of computational results is available in the ioChem- BD repository [72] and can be accessed via http://dx.doi.org/10.19061/iochem-bd-1-35.

3.3. Results and Discussion

The optimal geometries and relative energies of all possible intermediates and transition states (TS) were evaluated by means of DFT based methods. These energies were used for constructing the reaction energy map with all different possible reaction pathways. These results were used to carry out a kinetic study, in which we treated the different possible mechanisms separately in order to observe their kinetic significance. This study is presented in the next Chapter.

As mentioned before, the borylation reaction via C-F bond cleavage was firstly described as following a classical cross-coupling mechanism. The cross-coupling mechanism consists in the exchange of two fragments (**X** and **Y** in Figure 2) between two different reactants (**R-X** and **R'-Y**) assisted by a metal complex **ML_2** as catalyst. Figure 3-2 shows the scheme of the classical cross-coupling reaction mechanism that comprises three main steps. These steps are: oxidative addition, transmetalation and reductive elimination.

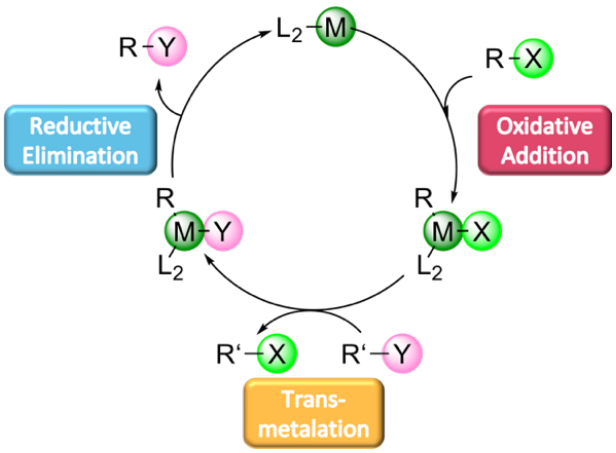

Figure 3-2. Classical Cross-Coupling mechanism scheme.

The first step, the oxidative addition, is the linkage between a molecule of one reactant **R-X** and the catalyst. At this step the catalyst is oxidized and the **R-X** bond in the reactant molecule is broken. The next step is the transmetalation where the second reactant **R'-Y** reacts with the intermediate exchanging substituents. At this step we obtain a sub-product of the reaction, **R'-X**. Finally, the reductive elimination takes place, the catalyst is reduced and it goes back to its initial configuration, and we obtain the desired product **R-Y**.

In the Martin's reaction, the $Ni(PCy_3)_2$ complex plays the role of catalyst and the two reactants that exchange fragments are aryl fluoride and the diboron 5,5-dimethyl-1,3,2-dioxaborolane (B_2nep_2). Therefore, there is any reason preventing this reaction to follow a classical cross-coupling mechanism. Also, that the oxidative addition and the reductive elimination are the first and last steps seem to be well accepted. However, the recipe contains a fourth participant, the sodium phenolate, which its role is unraveled yet. In order to understand the basics of the reaction mechanism, we outlined three possible scenarios for the transmetalation step: (a) absence of base, (b) presence of the phenolate ion, (c) participation of both the phenolate ion together with its Na^+ counter-ion. Also, considering the labile character of the metal-phosphine bonds, we plan to examine the reactivity of both mono- and bis-phosphine complexes in each reaction step.

3.3.1. Oxidative Addition

As in the case of a classical cross-coupling, the reaction starts with the oxidative addition reaction. The nickel catalyst reacts with the aryl fluoride by breaking the C-F bond, so by inserting the metal between these two atoms. At this point, the nickel atom evolves from a linear coordination geometry to a square-planar coordination, and it is oxidised from Ni(0) to Ni(II). Taube and his group reported the high lability of Ni(II)/phosphine complexes,[73] what opens the possibility that both bis-phosphine complexes and mono-phosphine complexes could be present in the reaction

media. Consequently, we guessed that nickel bis-phosphine complexes could experience a sort of dephosphination process in some steps of the mechanism.

3.3.1.1. OXIDATIVE ADDITION WITH $Ni(PMe_3)_2$

As mentioned above the oxidative addition could occur either on the bis-phosphine complex or on the mono-phosphine one. We start describing the oxidative addition with the participation of bis-phosphine compounds by considering first a model ligand, trimethyl-phosphine (PMe_3), instead of bulkier tricyclohexyl-phosphine (PCy_3) used in the experiments.

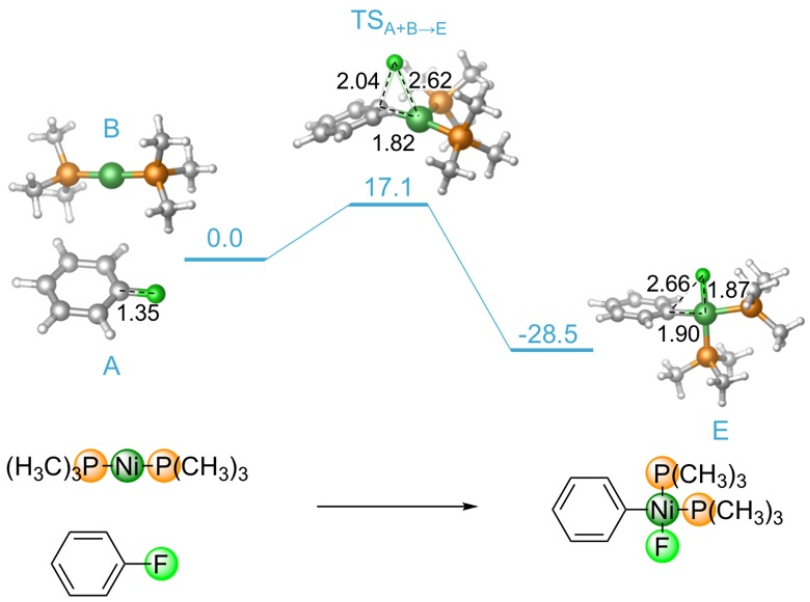

Figure 3-3. Relative Gibbs energies, molecular structures for the oxidative addition step for bis-phosphine complexes and selected geometrical parameters. All energies in kcal·mol^{-1}. Bond distances in Å.

We characterized the reactants, the transition state (TS) and the products of the bis-phosphine oxidative addition. In Figure 3-3 the molecular models and the corresponding bond distances of the reactants (**A**, **B**), transition state ($\mathbf{TS_{A+B->E}}$) and product (**E**) of this reaction step are presented. As it can be seen in Figure 3-3 the TS

consists in the nickel insertion into the C-F bond, so this bond elongates from 1.35Å in the reactant to 2.04Å in the TS. This insertion shapes a triangle C-Ni-F (**$TS_{A+B\rightarrow E}$** in Figure 3-3), where the shortest edge is C-Ni bond and the longest one is Ni-F with 2.62Å. This TS evolves to the square-planar compound **E**, where the two phosphines lie in *cis* disposition. Herein, the C-F bond is completely broken (2.66 Å interatomic distance). Curiously, the distance C-Ni is a bit longer in the product than in the TS, 1.90Å vs 1.82 Å.

Figure 3-3 collects also the relative Gibbs energies for the species involved in this reaction step, which show that the oxidative addition for $Ni(PCH_3)_2$ is exergonic by 28.5 $kcal{\cdot}mol^{-1}$, with an activation energy of 17.1 $kcal{\cdot}mol^{-1}$.

3.3.1.2. OXIDATIVE ADDITION WITH NI(PME_3)

As introduced above, Ni(II)/phosphine compounds are labile, therefore, it is reasonable to anticipate the presence of mono-phosphine compounds. Herein, we present the results of the oxidative addition step with the participation of mono-phosphine compounds.

As for the bis-phosphine compound we characterized the reactants, transition state and product, whose molecular structures are shown in Figure 3-4 together with their most significant bond distances. As the reader can observe, the structure of the TS mono-phosphine differs with respect the TS bis-phosphine. The angle and the bond distances are quite different. Whereas in the TS bis-phosphine the C-F distance is quite long, in the mono-phosphine TS the distance is shorter, so the C-F bond cleavage is only slightly advanced with a bond distance of 1.51Å. However, the Ni-C distance for mono-phosphine TS is smaller than in the TS bis-phosphine. This TS gives rise to a T-shape product **EM** (Figure 3-4). Both the Ni-C and Ni-F bond distances of the mono-phosphine product are shorter than in the bis-phosphine product, but the angle C-Ni-F is wider because the absence of the second phosphine ligand.

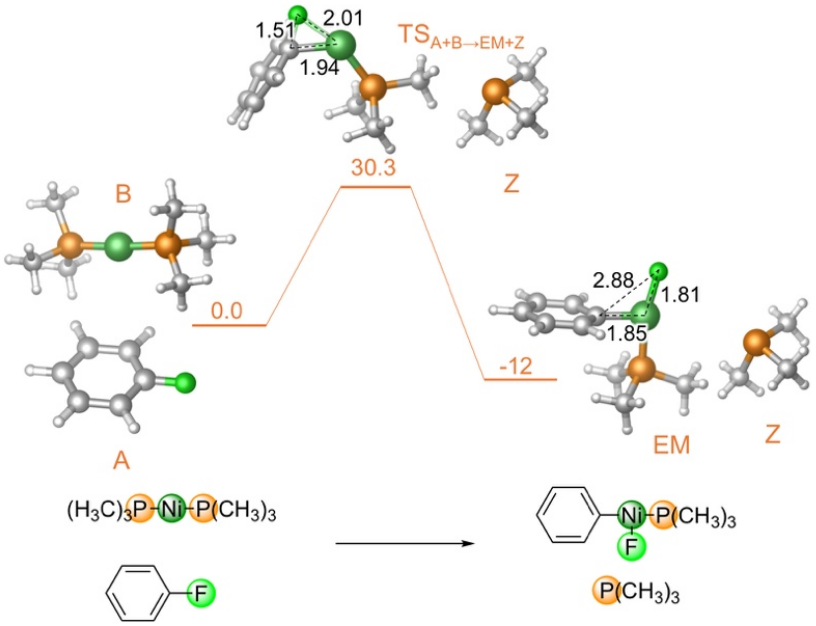

Figure 3-4. Relative Gibbs energies and molecular structures for the oxidative addition reaction of mono-phosphine Ni complexes and selected geometrical parameters. Energies are in kcal·mol^{-1}. Bond distances in black and in angstrom (Å).

As for the bis-phosphine oxidative addition we constructed the reaction energy profile in order to compare the energies. Figure 3-4 shows also the relative Gibbs energy of this TS and product. It can be observed that the energy barrier of this reaction is 30.3 kcal·mol^{-1}, higher than the bis-phosphine oxidative addition. The product obtained, **EM**, is less stable than the product of the bis-phosphine oxidative addition.

3.3.1.3. Oxidative addition with Ni(PCy$_3$)$_2$ and Ni(PCy$_3$)

In computational sciences is it usual to start studies by considering a simple model of the real system, because this sort of strategy supposes saving computing time and resources. In our case, we simplified the real ligand, PCy$_3$, by the smaller PMe$_3$. Once the reaction in the model system is clarified, we computed the Gibbs energy profile for the real ligand. These results are

presented in Figure 3-5, where the molecular models of the reactants, TS and products are also shown. The main geometrical features of the new TSs, **$TS_{A+O\rightarrow P}$** and **$TS_{A+O\rightarrow PM}$**, are conserved, so almost no relevant changes were observed with respect to its analogous characterized with the model ligand, **$TS_{A+B\rightarrow E}$** and **$TS_{A+B\rightarrow EM}$**. The same happens with the molecular geometries of the intermediates obtained in this step.

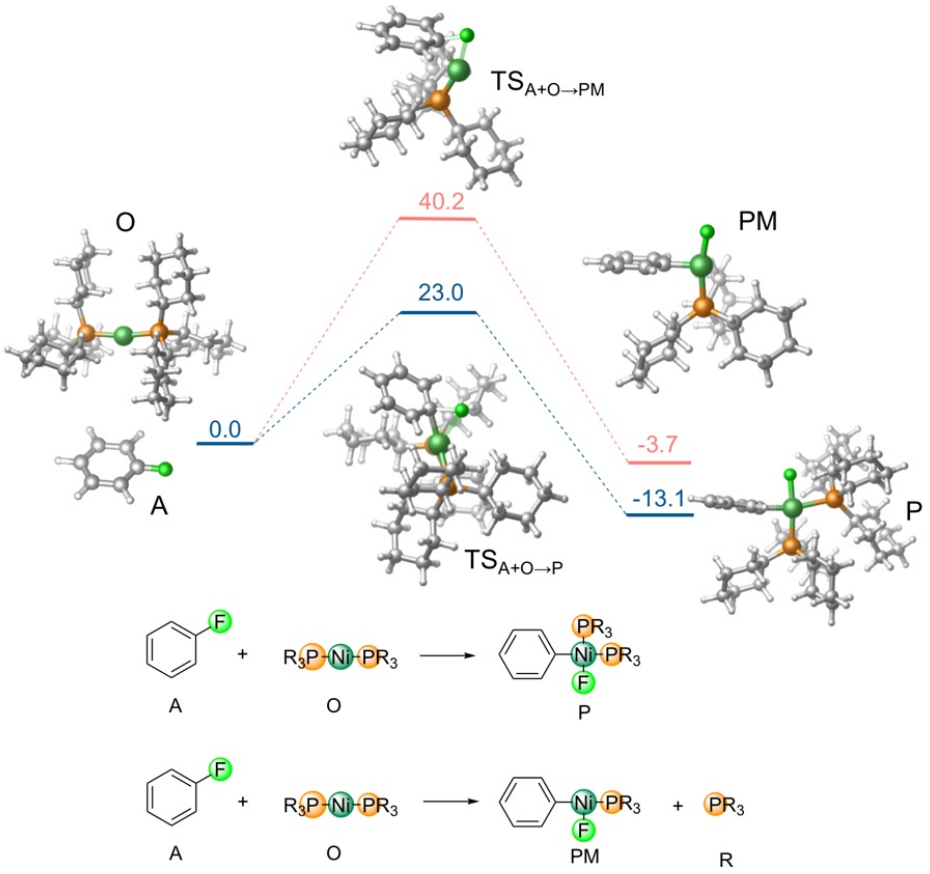

Figure 3-5. Oxidative addition Gibbs energy profile for tricyclohexyl-phosphine Ni(0) complex. Dark blue line corresponds to bis-phosphine compounds and the coral line to the mono-phosphine ones.

Regarding the energies of the TSs with the real ligand, we observed a significantly increase of about 10 kcal on both cases. Therefore, the oxidative addition reaction on the bis-phosphine complex is more favourable than on the mono-phosphine one.

3.3.2. ISOMERIZATION

The next step in the mechanism is the isomerization of the intermediates, **E** and **EM**, obtained in the oxidative addition reaction step. Square-planar complex **E** could experiment a *cis/trans* isomerization process regarding the mutual disposition of the two phosphines. We studied this step taking into account the lability of the Ni(II) complexes, as mentioned above in section 3.3.1, thus considering bis- and mono-phosphine intermediates as well.

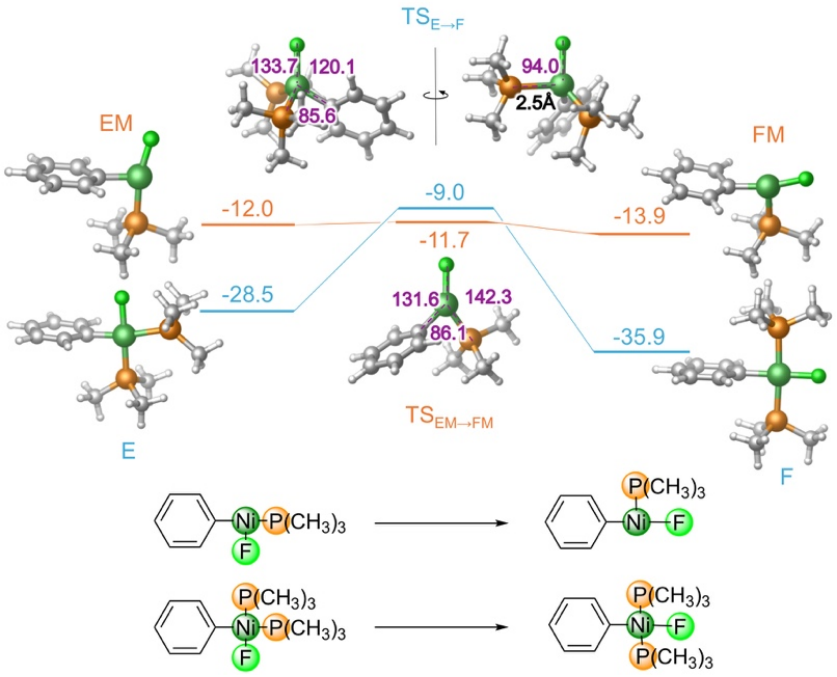

Figure 3-6. Gibbs free energies and molecular models for the cis/trans isomerization step with the model ligand. Blue line is for the bis-phosphine and the orange line for the mono-phosphine compounds. All energies are in kcal·mol^{-1}. Angles in TSs are in purple and in degrees.

Likewise, in previous section we have characterized the species that participate in this reaction step. Figure 3-6 collects molecular models of the reactants, first intermediates **E** and **EM**; the TSs, **TS$_{E\rightarrow F}$** for bis-phosphine intermediate and **TS$_{EM\rightarrow FM}$** for mono-phosphine ones; and the products which are the corresponding trans isomer of the first intermediate, **F** and **FM** (M in a label

indicates mono-phosphine compounds). Whereas the TS of this kind of isomerization in tetra coordinated complexes has tetrahedral shape, a close look at the $\mathbf{TS_{E\rightarrow F}}$ shows that it presents a distorted geometry. That is because the $\mathbf{TS_{E\rightarrow F}}$ has one phosphine ligand lying perpendicular to the Ni-F bond, being the P-Ni-F angle 94.0°. Additionally, this phosphine ligand presents a quite long bond with nickel atom, longer than Ni-P bonds in other complexes. For these reasons, the angles are like $\mathbf{TS_{EM\rightarrow FM}}$ which has a trigonal shape. These TSs give as products the corresponding intermediates **F** and **FM**.

Additionally, Figure 3-6 shows the energies for this *cis/trans* isomerization. Although the Gibbs energy of the reactants and products of this reaction are lower for bis-phosphine compounds, the energy barrier is lower for mono-phosphine TS. There, we could visualize the isomerization process occurring in a concerted manner with phosphine decoordination: the product bis-phosphine of the oxidative addition (**E**) loses a phosphine and becomes a mono-phosphine *cis* intermediate (**EM**). Then, the isomerization takes place giving a mono-phosphine intermediate (**FM**), which can evolve to the bis-phosphine compound (**F**) easily.

3.3.3. ISOMERIZATION WITH PCY_3 LIGAND

As for the oxidative addition, in this *cis/trans* isomerization step we also considered the real ligand used experimentally, and collected the results in Figure 3-7. It is important to remark that it was not possible to characterize the corresponding transition state for the isomerization in the bis-phosphine compound because the steric hindrance between the phosphine substituents. All the attempts failed and lead to discoordination of one of such voluminous phosphine ligands. Thus, Figure 3-7 displays the results for mono-phosphine compounds only.

Although we could not determine the TS of the bis-phosphine isomerization, the study in the mono-phosphine it is of interest, since we can compare it with the results just obtained for the

model ligand. Analysing the molecular model of the TS for the isomerization (**$TS_{PM→QM}$**) in Figure 3-7 , and comparing with its analogous in Figure 3-6 (**$TS_{EM→FM}$**), we could not detect significant differences. Regarding the activation energy of this step, data in Figure 7 indicates that $\Delta G^{\neq}$ is about 2 kcal·mol^{-1} higher than the value computed for the model ligand.

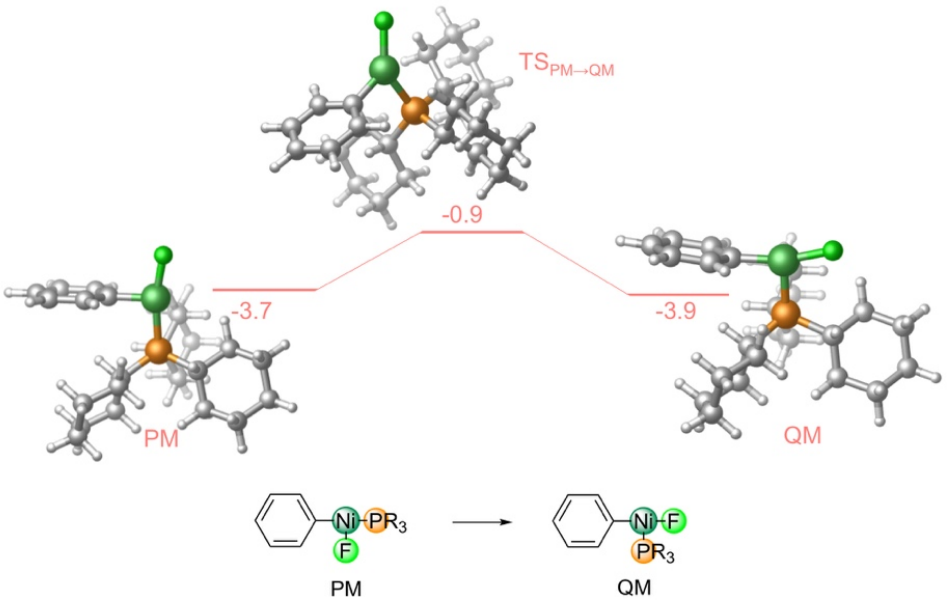

Figure 3-7. Gibbs free energies and molecular models of the isomerization path with the real ligand.

3.3.4. TRANSMETALATION

After the oxidative addition reaction and isomerization steps, the next logical transformation is the transmetalation step. In the present case, the transmetalation consists in the reaction between the intermediate obtained after the isomerization (**F** or **FM**) and the diboron (**C**). In this step, both the Ni-F bond and the diboron B-B bond break, the boryl boron moiety will end up coordinated to the nickel atom whereas the other boron eliminates together with the fluorine ligand. This is what we call the classical transmetalation mechanism. However, as we mentioned above,

the participation of the sodium phenolate is not clear and could modify this step precisely. For this reason, we considered three possibilities: (i) the classical transmetalation; (ii) a non-classical transmetalation, with the participation of one molecule of the neutral base, NaOPh; and (iii) a non-classical transmetalation with the anionic phenoxide base, as Figure 3-8 schematically shows for both bis- and mono-phosphine complexes.

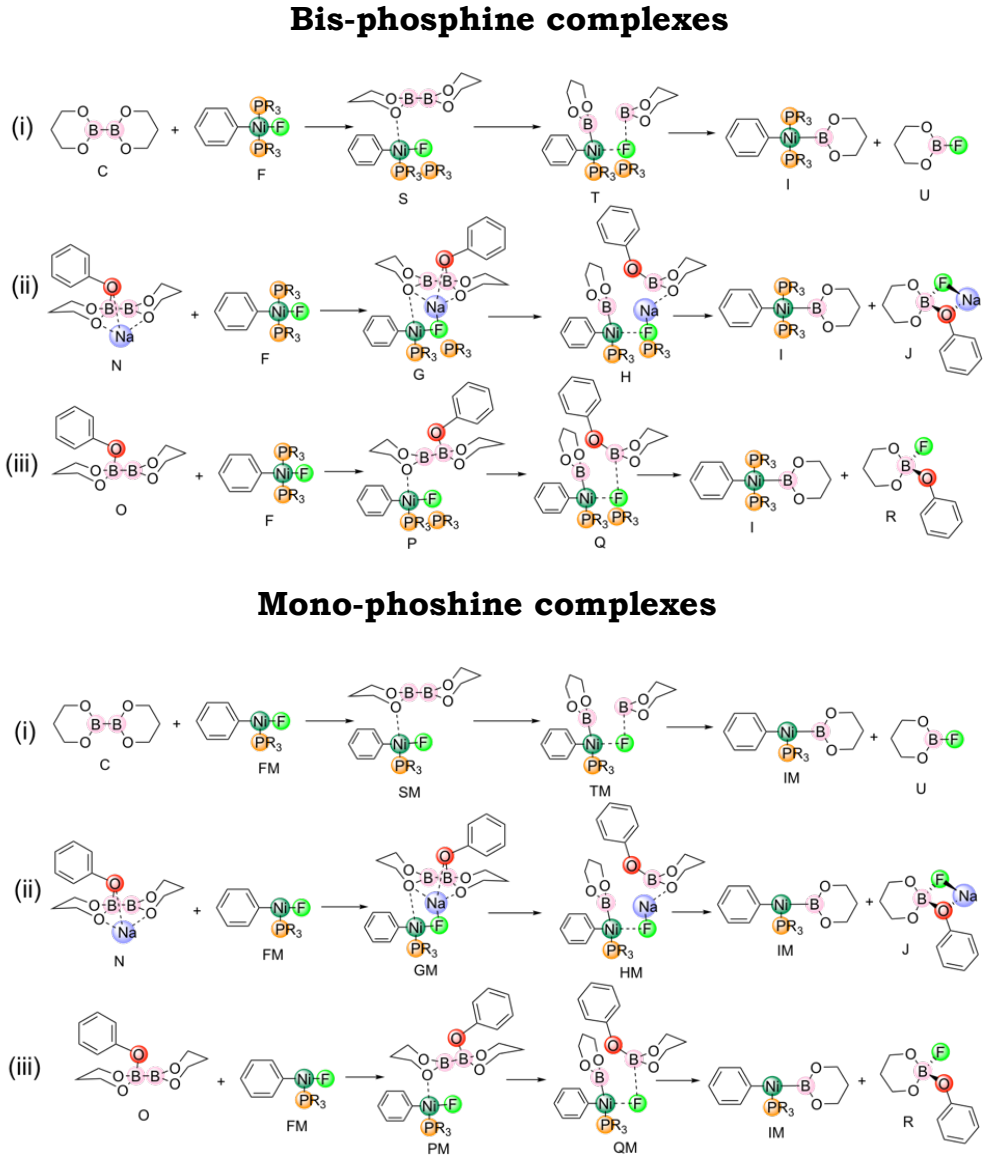

Figure 3-8. Schematic representation of possible transmetalation mechanisms.

3.3.5. PARTICIPATION OF NAOPH

As just mentioned, the participation of the sodium phenolate make us suspect that the transmetalation step might not follow the classical way. Bo's group demonstrated the metal-free activation of diboron compounds by means of a Lewis bases, that may interact with one boron atom and form a stable sp^2-sp^3 diboron/base adduct[74]. This type of adducts have been reported by other groups[75,76]. Lewis acidic sp^2 boron compounds can interact with a Lewis base to form a sp^3 Lewis-acid/Lewis-base adduct. In the case of a diboron compound having a B-B single bond, coordination of a Lewis base would be expected to form sp^2-sp^3 diboron compounds[77]. The recent report by Marder and co-workers on the formation and X-ray characterization of such Lewis base/diboron adducts confirmed the structures predicted teoretically .[78] Therefore, we guessed that the transmetalation step might follow a non-classical pathway, in which the base reveals itself as an essential player. We thus considered that sodium phenolate, (**D**), interacts directly with one boron atom of B_2nep_2 (**C**) giving an adduct (**N**), whose molecular structures are represented in Figure 3-9.

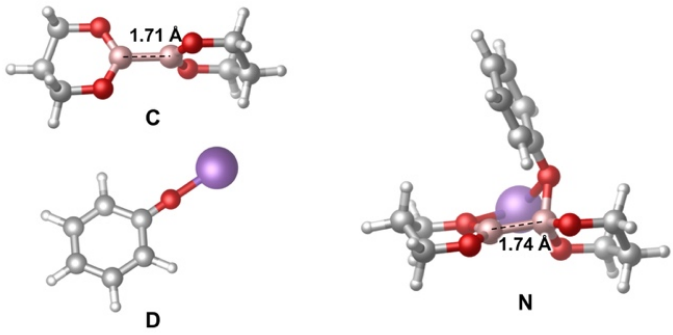

*Figure 3-9 Molecular models of the diboron **C**, sodium phenolate **D** and base/diboron adduct **N**. B-B bond distances in Å.*

The interaction of the diboron organocompound and the base affects only slightly the B-B bond distance, from 1.71 Å in **C** to

1.74 in the adduct (**N**), but it largely affects the B-B bond electronic character indeed. Whereas in **C** both boron atoms hold the same MPA charge (+0.30), the B-B bond appears strongly polarized in **N** (B_{sp2}:+0.11; B_{sp3}:+0.56). Therefore, the B-B bond of **C** is activated by the interaction with the phenolate (**D**). Another curiosity of this adduct (**N**) is the sodium cation, which remain coordinated to three oxygen atoms, two of the diboron and the one in the phenolate. The computed geometry is in very good agreement with the X-ray geometries characterized by Marder's group.[78] Additionally, the adduct **N** was found to be 30 kcal·mol^{-1} more stable than the separated diboron and sodium phenolate species. This fact indicates that the interaction between the phenolate and the diboron is rather strong, and given that the base is in excess in the experimental setup, all diboron persists in the adduct form. Actually, fully equivalent species were recently considered by Chen et al.[79] in a computational study on the Ni-catalysed Miyaura borylation reaction. In that case, B_2pin_2 and the base K_3PO_4 formed a pre-adduct, which also triggered the transmetalation step.

3.3.5.1. TRANSMETALATION OPTIONS

Since we characterized the transition states and their corresponding products for both the bis-phosphine (Figure 3-10) and mono-phosphine (Figure 3-11) reaction pathways, first we present the results corresponding to the bis-phosphine transmetalation scenario. Figure 3-10 shows the molecular models of the TSs that were found starting from the bis-phosphine intermediate **F**. Actually, our starting point for studying this step is not **F**, but its molecular complex with the diboron. We were forced to take this into consideration because the TSs would be more stable than the sum of **F** and the diboron. Therefore, in the classical transmetalation, the initial intermediate is **S** and it gives as product **T** (see Figure 3-10), while **G** and **P** correspond to supramolecular complexes with the diboron activated by NaOPh and OPh^-, respectively.

The geometric features of the TS for the classical transmetalation (**$TS_{S\rightarrow T}$** in Figure 3-10) indicate that the two new bonds, B-F and B-Ni, are formed and the B-B bond is broken. **T** actually evolves to the products represented in Figure 3-8, namely **I**, ready to undergo reductive elimination, and sub-product **U**, the boron ester fluoride FBnep.

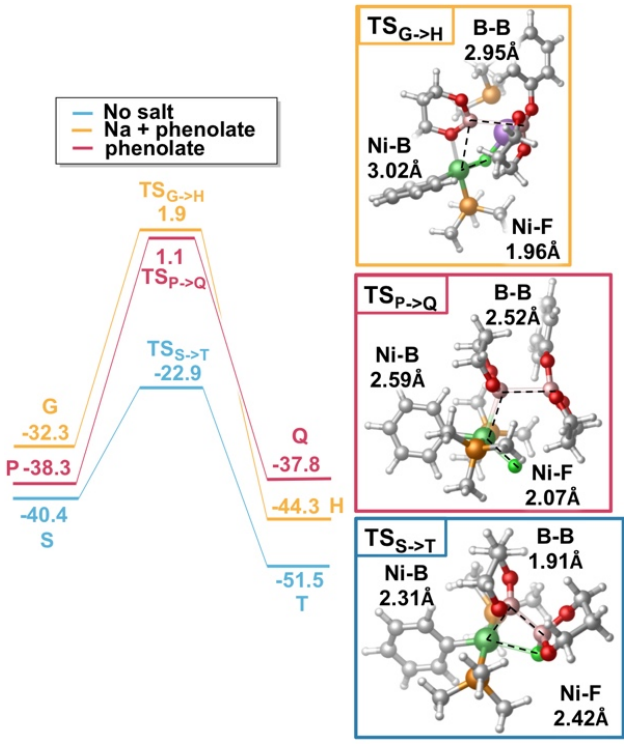

Figure 3-10. Relative Gibbs energies (in kcal·mol^{-1}) and molecular models for species involved in the bis-phosphine transmetalation step.

We collected in Figure 3-10 the Gibbs Energies of the corresponding bis-phosphine TSs and in Figure 3-11 the corresponding values of mono-phosphine TSs. As mentioned above, in the construction of these REPs we had to include the previous adducts **G**, **P**, **S** in Figure 3-10 and **GM**, **PM**, **SM** in Figure 3-12, and later adducts **H**, **Q**, **T** in Figure 3-10 and **HM**, **QM** ,**TM** in Figure 3-11, because the potential energy of some TSs were found smaller than the sum of the previous intermediates. The

calculation of these adducts increase the energy activation of this step. The REP of the classic transmetalation step (blue line for bis-phosphine TSs in Figure 3-10 and light purple of mono-phosphine TS in Figure 3-11 show that both transmetalation reactions are favourable. However, the activation energy of the classic transmetalation bis-phosphine TS (blue line in Figure 3-10) is smaller (17.5 kcal·mol^{-1}) than for the mono-phosphine TS (light purple line in Figure 3-11) activation energy (19.7 kcal·mol^{-1}). Additionally, the classic transmetalation of bis-phosphine compound give more stable products than in the mono-phosphine transmetalation step. The presence of the sodium phenolate thus open other options.

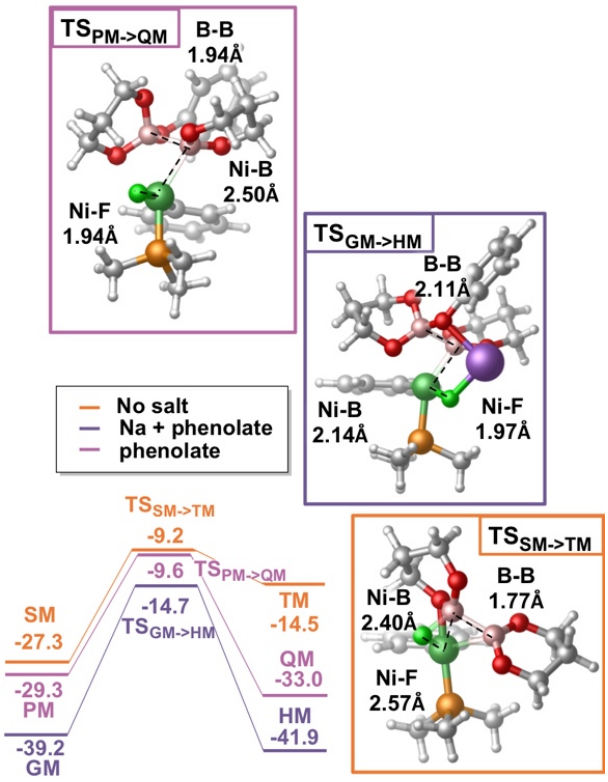

Figure 3-11. Relative Gibbs energies (in kcal·mol^{-1}) and molecular models for species involved in the mono-phosphine transmetalation step.

The formation of the diboron/NaOPh adduct can modify the energetics of the transmetalation step. That adduct might react with intermediates **F** and **FM**. For the study of this reaction we characterized the TSs and the corresponding products, in the same way as for the classic transmetalation. At this point, we considered two possibilities, either the sodium phenolate is dissociated or it is not. If the phenolate salt is dissociated (fully solvated) then the sodium cation does not participate in the reaction, but if it is not, the sodium ion is included in the model.

All the three transition states $\mathbf{TS_{S\rightarrow T}}$, $\mathbf{TS_{P\rightarrow Q}}$ and $\mathbf{TS_{G\rightarrow H}}$ in the bis-phosphine path, and also the three in the mono-phosphine path, present as common feature the fact that the imaginary vibrational frequency clearly corresponds to the breaking of the B-B bond. The Ni-F bond is only slightly activated when the phenolate is present. Note that in $\mathbf{TS_{G\rightarrow H}}$ the sodium cation interacts with the fluorine and one phosphine ligand was decoordinated, probably because steric congestion. Since this was observed in a model ligand, much smaller than the real PCy_3, we can guess that this path would be hardly reachable. The presence of the base clearly activates the B-B bond, since its bond distance in $\mathbf{TS_{S\rightarrow T}}$ and in $\mathbf{TS_{SM\rightarrow TM}}$ are the smallest, being the biggest the for B-B distance in $\mathbf{TS_{G\rightarrow H}}$.

In the case of bis-phosphine complexes, the two TSs $\mathbf{TS_{P\rightarrow Q}}$ and $\mathbf{TS_{G\rightarrow H}}$ presented quite high activation energies, therefore it seemed that based on this result, the participation of sodium phenolate salt would not benefit the reaction. However, the scenario for mono-phosphine complexes is different. The activation barrier for the classic transmetalation through $\mathbf{TS_{SM\rightarrow TM}}$ is the lowest, but the product is rather unstable. The presence of phenolate $\mathbf{TS_{PM\rightarrow QM}}$ does not largely modify the barrier but makes the product stable. The presence of the NaOPh salt, so counting with the additional stabilization of the Na cation, provides the most stable intermediate **GM**. Although, the barrier through $\boldsymbol{TS_{GM\rightarrow HM}}$ is the highest, this transition state is the lowest in energy.

All these results make to think us that after the isomerization path, the mono-phosphine trans intermediate (**FM**) reacts with the adduct **G** forming the pre-adduct **GM** which is more stable than the other pre-adducts (**G**, **P**, **S**, **PM** and **SM**). Then, the transmetalation goes through the $\mathbf{TS_{GM\rightarrow HM}}$ giving the **HM** post-adduct. This **HM** post-adduct decomposes giving the third intermediate **IM** and a sub-product **J**.

3.3.6. Reductive Elimination

Finally, we reach the last step of the mechanism. As for the cross-coupling mechanism, the last step is the reductive elimination reaction, in which the new C-B bond is formed and the catalyst recovered by the formal reduction of the metal atom. As in previous sections we studied this step for mono and bis-phosphine compounds.

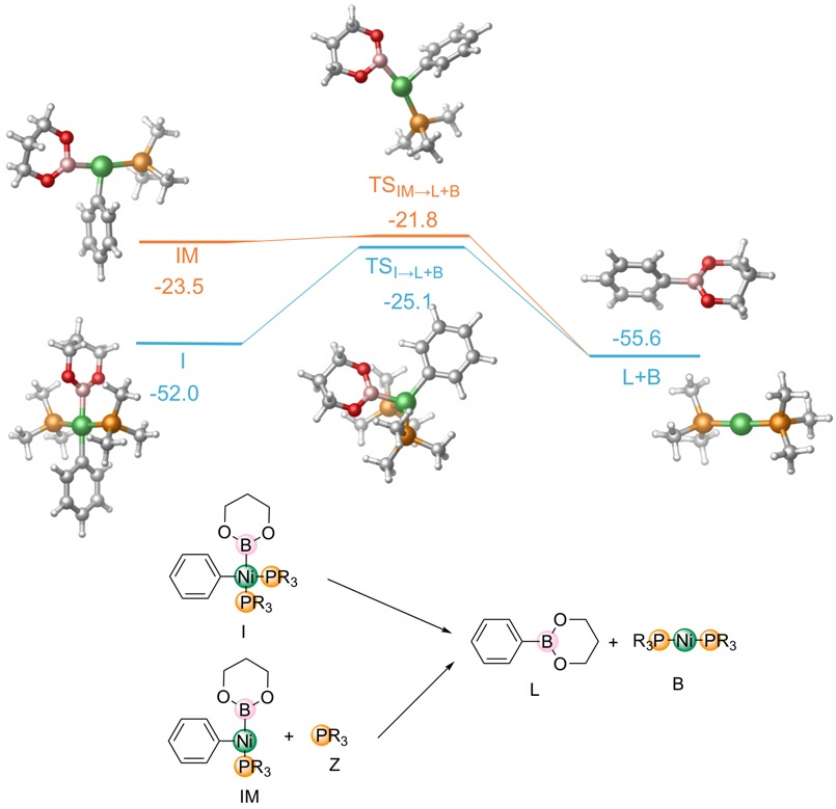

Figure 3-12 Relative Gibbs energies for and reactants, TSs and products molecular models. Bis-phosphine compounds are indicated in blue and ono-phosphine ones are in orange.

Figure 3-12 shows the molecular models for the reductive elimination TSs: $\mathbf{TS_{I\rightarrow L+B}}$ for bis-phosphine compounds and $\mathbf{TS_{IM\rightarrow L+B}}$ for mono-phosphine compounds. We found that the bis-phosphine trans complex **I** can directly undergo the reductive elimination without the need of a prior *cis/trans* isomerization. The Nickel atom in $\mathbf{TS_{I\rightarrow L+B}}$ in Figure 3-12 present a tetrahedral coordination sphere, similar to an isomerization TS, but the B-C attraction makes that at this distance these two atoms can react. As regards $\mathbf{TS_{IM\rightarrow L+B}}$, its geometry is similar to an hypothetic **IM** trans isomer. Figure 3-12 shows also the free energies of species involved in this step, indicating that the reductive elimination through mono-phosphine compounds is more favorable than thorough bis-phosphine species.

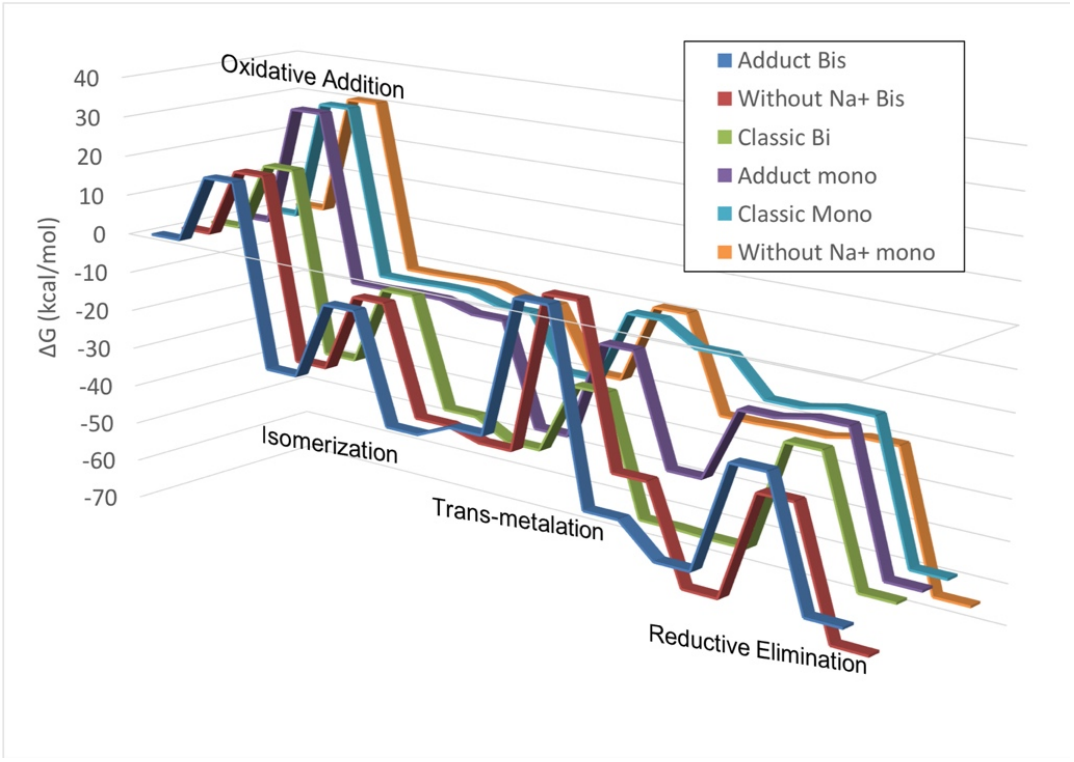

*Figure 3-13. Reaction free energy profiles of all the studied reaction pathways for the nickel catalysed aryl-F borylation reaction. Blue: with adduct **N** in bis-phosphine compounds; red: with adduct **O** (Figure 3-8) in bis-phosphine compounds; green: classic cross-coupling mechanism for bis-phosphine compounds; purple: with adduct **N** in mono-phosphine compounds; cyan: with adduct **O** (Figure 3-8) in mono-phosphine species; orange: classic cross-coupling in mono-phosphine compounds.*

Once the thermodynamic study of all steps is completed, all species and possible reaction paths were plotted together in Figure 3-13. It permits seeing the differences between the different reaction pathways in global manner.

Figure 3-13 depicts the six free energy profiles, so six catalytic cycles for the Martin's reaction. It can be clearly observed that the most effective oxidative addition is the one occurring on the bis-phosphine complex. However, after that, the *cis/trans* isomerization is well-defined and is more favorable for mono-phosphine compounds. In the transmetalation reaction pathway, the most stable pre-adducts are **S** and **GM**, and are the precursors of the transmetalation. The transmetalation path happens through $\mathbf{TS_{GM \rightarrow HM}}$ giving the post-adduct **HM**. Finally, the adduct decomposes to give **IM** and the reductive elimination reaction takes place easily through the mono-phosphine complex for obtaining the desired product **L**.

3.3.7. Comparison of DFT Methods

Once the mechanism is completely studied and the the most thermodynamically favorable mechanism is determined, it is interest evaluating the differences between few of the most popular DFT levels[80]: B3LYP, B3LYP-D3, M06-2X and the used in this chapter ωB97xD. This was achieved by using Clone-Report, a Python code developed during the course of this thesis. This code uses Fireworks[28] -a workflow manager- and ioChem-BD database,[81] and is a tool to help recalculating any reaction energy profile report constructed within ioChem-BD. This code takes the geometries of all species, and their relationships, resubmits all calculations needed to reconstruct a new ioChem-BD report in the data base, and controls the correctness of all calculations. Basically, this program saves time constructing the new inputs, resubmitting jobs, and recollecting the results, so it avoids possible errors.

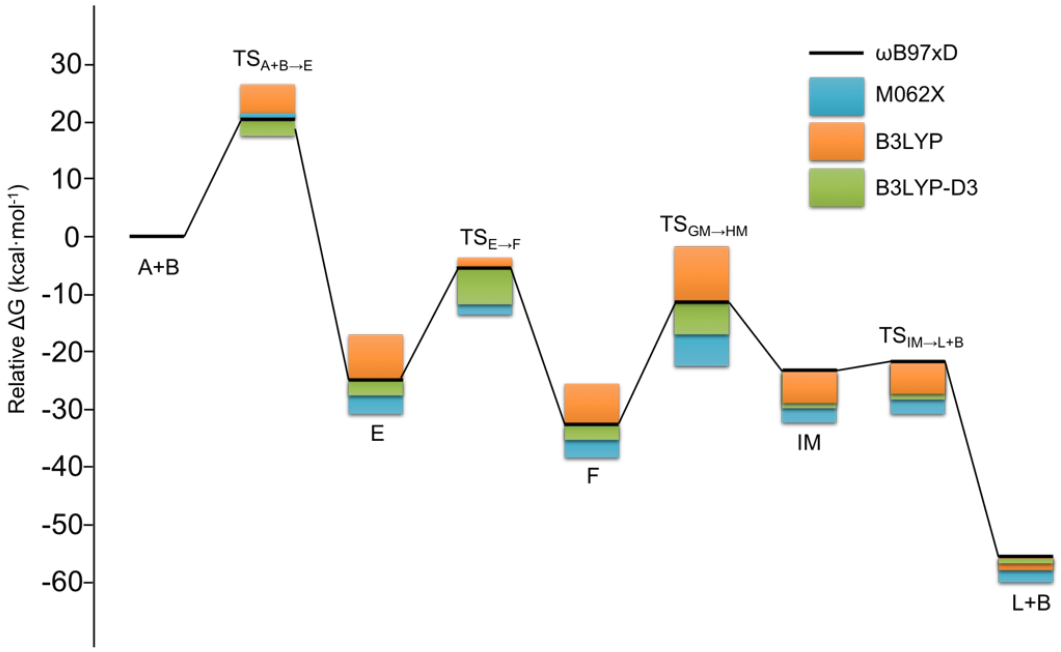

Figure 3-14. Reaction Free Energies for some species involved in one the studied reaction mechanisms. Black: ωB97XD. Blue: M06-2X; orange: B3LYP; green: B3LYP-D3.

Figure 3-14 represents the REP of one of the possible mechanisms for the aryl borylation at the ωB97XD level (black line), and the differences between this method and some others (B3LYP, B3LYP-D3 and M06-2X) with colored bars. We could not see big differences between the different DFT methods. The method which differs more is B3LYP, for the reason that it does not include dispersion terms that contemplate the non-bonding interactions. In general, B3LYP-D3 and M06-2X gives relative energies lower than ωB97XD. Because the minimal differences between DFT methods, we present in Figure 15 an ωB97XD/M06-2X/B3LYP-D3 averaged-profile, so the mean and the standard deviation for each reaction state. Note the including B3LYP increases the deviation in all the cases, and should not be taken to calculate such DFT averaged-profile. In any case, we think that by using this combination of tools (ioChem-BD, Fireworks, Python) it is now easier to elaborate the data in Figure 15, so to assess the goodness of the DFT methods in use.

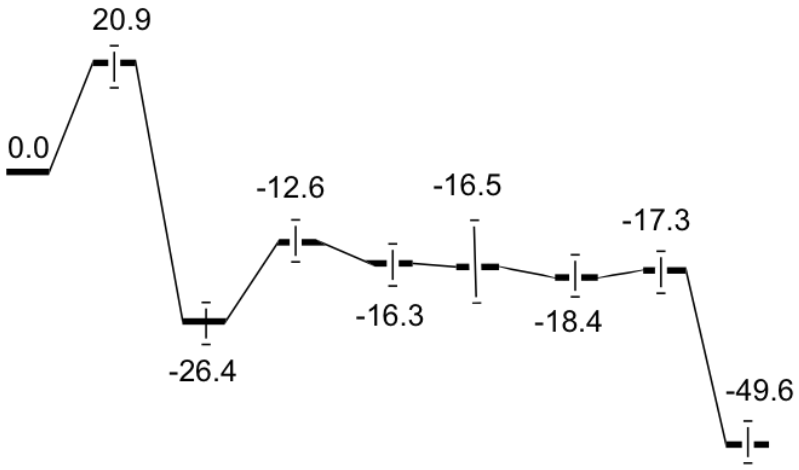

Figure 3-15. Reaction Free-energy Profile with the mean of the three methods and the standard deviation with error bar.

3.4. CONCLUSIONS

In this chapter was treated the study of the aryl borylation assisted by nickel catalyst studied experimentally by Martin. In a first glance, we thought that the reaction could follow a classic cross-coupling mechanism. However, the presence of the sodium phenolate changes the classic mechanism introducing a new participant. Additionally, the classical mechanism could be modified by the dephosphination considering the lability of the phosphine ligand.

The mechanism of the borylation reaction of aryl fluoride assisted by a nickel catalyst and base was unraveled by means of DFT based methods. The presence of the sodium phenolate activates the diboron and modifies the classic cross-coupling mechanism. The reaction starts with the oxidative addition, where the metal catalyst breaks the C-F bond, followed by a *cis/trans* isomerization. This isomerization is more favourable for the mono-phosphine nickel compounds because steric effects. Then the *trans* intermediate reacts with the adduct B_2nep_2/NaOPh forming an stable pre-transmetalation species, which evolves to the first product of this reaction and an intermediate. This last one

complex finally undergoes the reductive elimination, generating products and recovering the active catalytic species.

As a summary, we the most favourable thermodynamic mechanism of this aryl borylation reaction is presented in Figure 3-16 in the form of a catalytic cycle scheme, which is based on the most favourable thermodynamic mechanism.

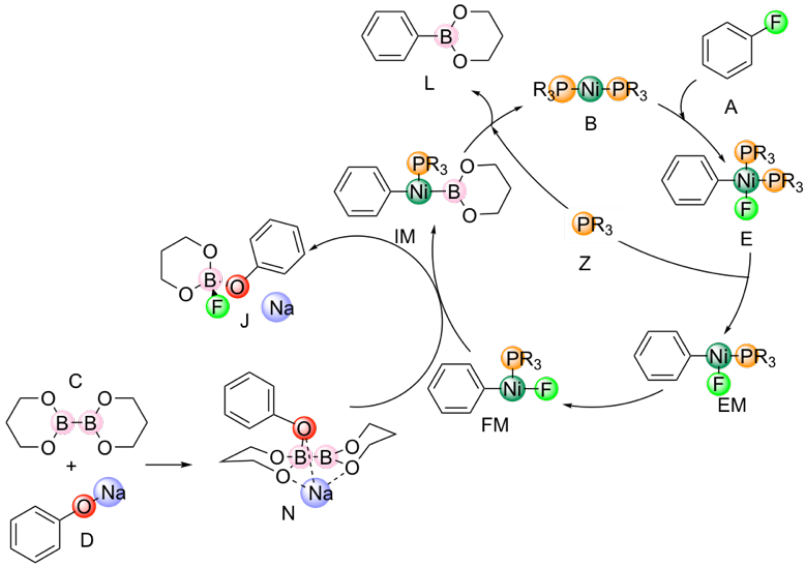

Figure 3-16 Thermodynamic mechanism scheme with the most relevant participating compounds.

"De nada valdría un movimiento femenino en un mundo sin justicia social." Evita Perón

CHAPTER 4

4. *KINETIC STUDY OF THE NI-CATALYSED ARYL BORYLATION*

4.1. INTRODUCTION

The computational study of a catalytic homogenous reaction is made through the electronic structure calculation of the reactants, intermediates, transition states (TS) and products of the reaction. The Gibbs energy of each specie calculated from the outputs of the

DFT calculation is taken. Then, Reaction Energy Profile (REP) can be constructed and evaluated if the TS barriers are reachable (less than 20 kcal·mol^{-1})[82] and make their conclusions. This is the traditional procedure for the computational study of a reaction.

In recent years, computational chemistry went further in their study with the kinetical analysis of the system. Not long ago, Maseras and Besora release a review[36] about different homogenous catalytic reactions studied kinetically. All the studies presented have in common the calculation of the rate constants from DFT previous studies. The principal reasons for the kinetic studies are the evaluation the effect of the use different initial concentration[83–89] and the key species at low[90–92] and high[93] concentrations.

Since in the DFT study of the borylation of aryl halide catalysed by nickel (Chapter 3) we found multiple possible reaction pathways and parallel reactions, it could be of interest the microkinetical study of the reaction. Moreover, it is interesting see the effect that could have the different concentrations of the phenolate salt that, as seen in previous Chapter, is a key reactant. Moreover, kinetic study could demonstrate how the phosphine concentration could modify the mechanism due the multiple of dephosphination reaction takes place. All these facts only could be evaluated with a microkinetic analysis. In this chapter, we present the results of the microkinetic analysis of the borylation of aryl halide catalysed by nickel Martin's reaction[14].

4.2. Computational Details

All the rate constants presented in this chapter were calculated using the Eyring equation. For calculating the rate constants, we need activation Gibbs energies values, which we actually computed in the DFT study presented in the previous chapter. The system of kinetic equations was solved by using the COPASI program.[58] It is worth mentioning that at earlier stages of this study, the Tenua[57] program was used too. Tenua works fine for

simple systems and allows plotting the reaction map. However, the program becomes slow and the solver fails when the system of equations becomes sophisticated. Although Tenua is as easy to use as to COPASI, this algorithm is significantly faster while giving the same results.

Barrier-less reactions, such are those with no activation energy barrier, deserves particular attention. In homogeneous catalysis at low pressures, which is precisely our case, so in the liquid state, perfect mixture ensures the diffusion limit. One way to take diffusion phenomena into account is to rely in the *Encounter Ion Theory* and its equation [53–55]. For solving it, we calculated the diffusion constants by making use of the Smoluchowski equation[52], which requires the self-diffusion coefficient of each species. Those the self-diffusion coefficients were obtained from the Stokes-Einstein equation using hydrodynamic radius derived from DFT optimized geometries.

4.3. Results and Discussion

In Computational Homogeneous Catalysis, the classical way of studying a reaction is through the calculation of the energy of reactants, products, all possible intermediates, and the corresponding Transition States (TS) for each single chemical transformation, so for each reaction step. Connections between species define the reaction mechanism, or in other words, the reaction map. As it was exemplified by Besora et al.[36] in a recent review, further kinetic modeling provides additional insight and understanding. After a reaction mechanism has been proposed, running a kinetic analysis could be considered as a stress-test for the mechanism. Those authors[36] showed that microkinetic modeling could be implemented from static DFT calculations and using the Eyring equation and presented different examples of recent kinetic studies likewise.

Herein, we present a kinetic analysis of the Martin's reaction[94] relying on the results of the DFT based studies presented in the

previous chapter. This catalytic process comprises multiple reaction steps, ligand exchange processes involved in simultaneous equilibria, and particular reaction conditions that we would like to understand in connection with the microscopic understanding of the reaction mechanism. We aimed at unravelling different aspects that affect the reaction outcome, the yield at a given time or the effect of the concentrations of the reactants, thus properties that could not be studied from a classical static study.

4.3.1. Kinetic modeling of Catalytic Reaction Mechanisms

As mention above, the Eyring Equation[95] permits to obtain the kinetic constant of each single reaction step, and it can be calculated easily with the activation energy of each reaction step from previously constructed reaction mechanism. In Eyring Equation (Eq. 6), k_i is the kinetic constant, κ corresponds to the transmission coefficient (usually set to 1), k_B the Boltzman's constant, T refers to the temperature in K, and h is the Plank's constant. Additionally, $\Delta G^{\ddagger}$ is the Gibbs activation energy, which is the difference in energy between an intermediate and the corresponding TS, and R is the ideal gas constant. Then, given that we obtained all "$\Delta G^{\ddagger}$'s" for our mechanism, we can apply the Eyring equation and obtain the rate constants for each of the steps in the reaction mechanism.

$$k_i = \frac{\kappa k_B T}{h} e^{-\frac{\Delta G^{\ddagger}}{RT}} \qquad \textit{Eq. 6}$$

As a first attempt, we considered all the elemental reaction steps of the most favourable mechanism, this is nine reactions which we depicted in Figure 1. This includes nine transformations:

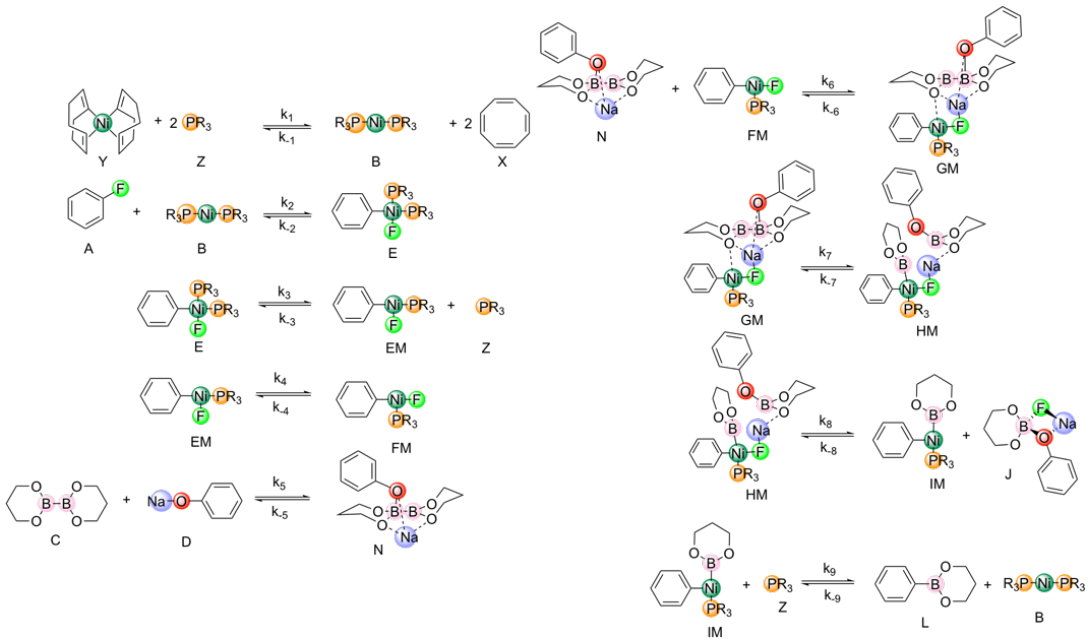

Figure 4-1. Elemental reactions of the most favourable thermodynamic mechanism.

1. The initial form of the catalyst $Ni(COD)_2$ evolves to $Ni(PR_3)_2$, the catalytically competent species.
2. Oxidative Addition, where the catalyst reacts with the aryl fluorine.
3. Dephosphination
4. Isomerization of the mono-phosphine complex.
5. Sodium phenolate activates the diboron compound forming an adduct.
6. Formation of a supramolecular complex between the diboron adduct and the *trans* mono-phosphine complex.
7. Transmetalation, where a boron takes the place of the fluorine ligand.
8. In this step we obtain the first product, with a tetrahedral boron, and the second mono-phosphine intermediate.
9. Reductive elimination step, where the desired product is obtained and the catalyst recovered.

Initial concentrations of the species taken for the kinetical analysis were for substrate (**A**): 0.25mol·dm^{-3}, for phosphine (**Z**):

0.05mol·dm^{-3}, for pre-catalyst (**Y**): 0.0125mol·dm^{-3}, for diborane (**C**): 0.75mol·dm^{-3} and for sodium phenolate (**D**): 0.75mol·dm^{-3}

Table 2. Activation Gibbs energies (kcal·mol^{-1}) and rate constants for the nine most favorable steps.

Reaction	$\Delta G^{\ddagger}$	K_i		$\Delta G^{\ddagger}$	K_{-i}	
R1	14.5	k_1	$4.28 \cdot 10^{04}$	0.00	k_{-1}	$7.984 \cdot 10^{12}$
R2	17.10	k_2	$1.408 \cdot 10^{03}$	45.60	k_{-2}	$7.804 \cdot 10^{-14}$
R3	16.50	k_3	$3.096 \cdot 10^{03}$	0.00	k_{-3}	$7.984 \cdot 10^{12}$
R4	0.30	k_4	$5.384 \cdot 10^{12}$	2.20	k_{-4}	$4.440 \cdot 10^{11}$
R5	0.00	k_5	$7.984 \cdot 10^{12}$	15.20	k_{-5}	$1.707 \cdot 10^{04}$
R6	0.00	k_6	$7.984 \cdot 10^{12}$	25.30	k_{-6}	$2.960 \cdot 10^{-02}$
R7	24.50	k_7	$8.465 \cdot 10^{-02}$	27.20	k_{-7}	$2.441 \cdot 10^{-03}$
R8	18.40	k_8	$2.553 \cdot 10^{02}$	0.00	k_{-8}	$7.984 \cdot 10^{12}$
R9	1.70	k_9	$8.561 \cdot 10^{11}$	33.80	k_{-9}	4.19710^{-07}

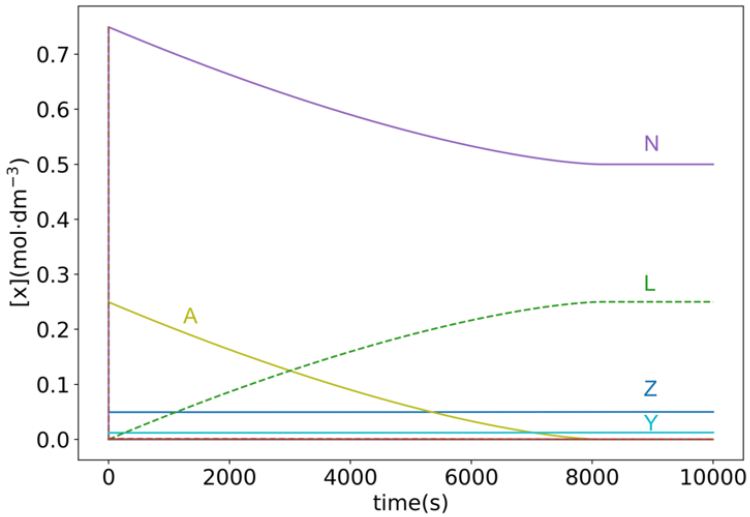

*Figure 4-2 Concentration versus time graph of the favourable thermodynamic mechanism kinetic study. **N**: B_2nep_2: NaOPh adduct. L: fluoroborane; **A**: fluorobenzene; **Z**: phosphine; **Y**: $Ni(COD)_2$. $[A]_0$=0.25M; $[Z]_0$=0.05M; $[Y]_0$=0.0125M; $[C]_0$=0.75; $[D]_0$=0.75.*

According to the experimental reports, the reaction provided 80% of the product after 12 hours.[14] This is thus the target that we aim that our mechanism could fulfil. In Figure 4-2 we present the results of solving the system of kinetic equations described

above in Figure 4-1, so concentration versus time profiles for all the species under the nine kinetic equations regime. By analyzing this data, the total conversion time is as short as 8000 seconds. This result is by far to be close to the reaction time reported experimentally. This raises issues about the accuracy of our calculations but also about the simplicity of the nine-steps mechanism. In the previous chapter we found other species, which could actually play some role. Also, other factors that might influence the reaction rates are the diffusion of the fastest barrier-less bi-molecular reactions, the co-existence of competitive reactions, or the solubility of reactants. All these factors will be treated in the following sections. Additionally, including or not entropy corrections could modify the rates, and last but not least, the DFT level used also matters. As we have seen in the previous chapter, the use of different DFT functionals affect differently the energy barriers.

In the previous chapter, we found that the B3LYP method gives, in general, higher barriers than ωB97XD. This means that the rates calculated from B3LYP activation energies will be lower so the overall reaction will be slower indeed. Our analysis indicates that, using B3LYP results, the total conversion time increases till 10000 seconds, instead of 8000 seconds. There is, therefore, no major difference between the use of B3LYP instead of ωB97XD, as mentioned in the previous chapter. For this reason, we will keep working at ωB97XD level for the rest of this chapter.

4.3.2. Treatment of Barrier-less and Faster bi-molecular reactions in Kinetic Studies

As mention above, considering diffusion could be crucial in the kinetic analysis of a reaction. It is important to mention that, in bimolecular reactions, diffusion may be a key component for the rate of a reaction, especially in very fast bimolecular reactions. Probably, the first person who observed this effect was, in 1917, Smoluchowski,[52] in his experiments with colloidal aggregations, noted that, in fast reactions, the diffusion can limit the rate. For

this reason, given that in our kinetic study the overall computed rate was much larger than the experimental value, we thought in applying corrections for diffusion in the barrier-less and fast bi-molecular elemental steps. A reaction is usually considered fast when its rate constant is larger than 10^8.[53–56]

To include diffusion effects, we need to quantify the approximation rate for the two molecules involved. This is achieved by the *encounter ion model,* which introduces the following equation:

$$\frac{1}{k_{app,+}} = \frac{1}{k_+} + \frac{1}{k_{diff}} \qquad \textit{Eq. 7}$$

where $k_{app,+}$ is the apparent rate constant, in which we add the diffusion effects k_{diff} and the rate constant $k_{+,}$ which were calculated with the Eyring equation (Eq. 6) above. k_{diff} constant can be calculated thanks to Smoluchowski's equation, developed by the homonymous scientist as a result of its observation which we mentioned before:

$$k_{diff} = 4\pi N_A \sigma D_{i,j} \qquad \textit{Eq. 8}$$

Smoluchowski's equation implies that the diffusion constant is directly proportional to the diffusion coefficient ($D_{i,j}$), and σ is the encounter distance, that is the distance between the two atoms that are reacting in the Transition State (TS). The diffusion coefficient can be easily calculated from the self-diffusion coefficients of species *i* and *j*, by using the equation:

$$D_{i,j} = \frac{D_{i,solv} D_{j,solv}}{D_{solv,solv}} \qquad \textit{Eq. 9}$$

where $D_{i,solv}$ is the self-diffusion coefficient of the first reactant (i) in the solvent (solv), $D_{j,solv}$ corresponds to the self-diffusion coefficient of the second reactant (j) in solvent (solv), and $D_{solv,solv}$ is the self-diffusion coefficient of the solvent (solv) itself. The self-

diffusion coefficient can be obtained by several means. The first one, and the most used, is from the slope of Mean Square Displacement (MSD) function versus time obtained in a molecular dynamics (MD) simulation.

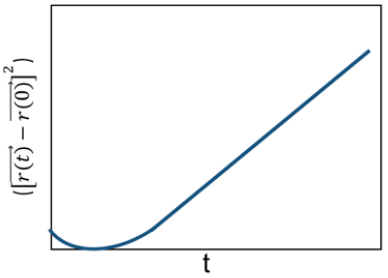

$$D_{i,solv} = \frac{1}{6}\lim_{t\to 0}\frac{d}{dt}([\overrightarrow{r(t)} - \overrightarrow{r(0)}]^2)$$

Figure 4-3. Mean Square Displacement versus time and the expression of the self-diffusion coefficient.

Figure 4-3 provides an example of MSD versus time graph. At short simulation times, the MSD graph refers to the time needed to achieve the thermal equilibrium, and that has nothing to do with diffusion. After that period, the MSD becomes linear with time, then, the graph describes the diffusion phenomena. So, the self-diffusion coefficient is the slope of the MSD function versus time at long simulation times.

The other way for obtaining the self-diffusion coefficient of a molecular system is by solving the Stokes-Einstein equation:

$$D_{i/solv} = \frac{k_B T}{6\pi\eta R} \qquad \textit{Eq. 10}$$

where the k_B is the Boltzmann's constant, T the temperature, R the so-called hydrodynamic radius of the molecule, and η is the viscosity constant of the solvent. With this equation, we can calculate the self-diffusion coefficient without the need to run any MD simulation, but we need the radius R. For this reason, using

the Stokes-Einstein equation could be a good and fast way for obtaining the self-diffusion coefficient.

In order to check for the differences between the two procedures, we decided to compare self-diffusion coefficients calculated by these two methods. For this, we took the self-diffusion coefficients calculated by Desmet et al.[56] using the MSD for a set of small molecules (THF, EA: Diethylamine, EAc: Ethyl Acrylate). Then, we proceeded to derive the corresponding radius R with the Stokes-Einstein equation (Eq. 10). We then obtained DFT fully optimized geometries for those species in Desmet paper[56], and take as a radius (R in equation Eq. 10) half of the farthest distance between any two atoms, plus 1% more to contemplate the electronic shell of the molecule.

Table 3. From left to right: self-diffusion coefficients (D_{ij}) obtained by Desmet [56]; hydrodynamic radius from Eq. 10; . d: dist two farthest atoms; r: radius of the molecule (r=d/2); r+10%; self-diffusion coefficient computed from r+10% and eq. 5. THF: tetrahydrofuran; EA: Diethylamine; EAc: Ethyl Acrylate:

	From Desmet MD simulations		From optimized geometries(2)			
	$D_{ij}(m^2 \cdot s^{-1})$	R(Å)(1)	D farthest atoms (Å)	R(Å)	R+1%core	$D_{ij}(m^2 \cdot s^{-1})$ (1)
THF	$2.01 \cdot 10^{-09}$	2.26	4.107	2.0535	2.25885	$2.01 \cdot 10^{-09}$
EA	$4.22 \cdot 10^{-09}$	1.08	3.62	1.81	1.991	$2.28 \cdot 10^{-09}$
EAc	$3.24 \cdot 10^{-09}$	1.40	6.16	3.08	3.388	$1.34 \cdot 10^{-09}$

(1) Calculated with Stokes-Einstein equation
(2) Calculated using B3LYP functional and dispersion D3, and 6-311G** as a basis set.

Table 3 collects the self-diffusion coefficients calculated by Desmet, the radii, and the coefficients calculated with the Stokes-Einstein equation. The results in Table 3 indicate we can calculate the self-diffusion coefficient in an approximate way. For THF, our results match those from Desmet. However, for EA and EAc, the computed radii are larger than those extracted from *Dij*, and consequently, the diffusion coefficients are smaller. Nonetheless, the order of magnitude of the values computed in such a way is correct, thus we decided to use them.

Once we proved that the Stokes-Einstein equation could be used for obtaining the self-diffusion coefficients from DFT geometries, we will include such corrections in our microkinetic modeling. First of all, we needed to locate the fastest and barrier-less bi-molecular reactions.

In Table 2 it is easy to identify that these reactions are **R5**, **R6**, and **R9** because they have a rate constant higher than 10^8. Note that **R4** is excluded from this treatment since its unimolecular character. **R5** and **R6** both correspond to barrier-less processes in which adducts form, while **R9** is the very low barrier reductive elimination reaction. Then, we can apply the procedure described above for calculating the diffusion rate constant.

Table 4. Rate diffusion calculation for the faster bi-molecular reactions ($k_{app,+}$). R: radius of each molecule; $D_{i/THF}$: Self-Diffusion coefficients; D_{ij}: Diffusion Coefficient; σ: distance between the two atoms that are reacting in the TS; k_{diff}: diffusion rate constant. $\Delta G^{\ddagger}$: new activation energy.

		R(m)	Di/THF(m²/s)	D_{ij}(m²/s)	σ(m)	k_{diff}	$1/k_{app}$	$k_{app,+}$	$\Delta G^{\ddagger}$
R5	C	$4.63\cdot10^{-10}$	$1.26\cdot10^{-09}$	$4.01\cdot10^{-10}$	$3.3\cdot10^{-10}$	$1.00\cdot10^{09}$	$9.98\cdot10^{10}$	$1.00\cdot10^{09}$	6.84
	D	$3.65\cdot10^{-10}$	$1.60\cdot10^{-09}$						
R6	N	$5.40\cdot10^{-10}$	$1.08\cdot10^{-09}$	$5.12\cdot10^{-10}$	$2.14\cdot10^{-10}$	$8.29\cdot10^{08}$	$1.21\cdot10^{09}$	$8.28\cdot10^{08}$	6.98
	FM	$4.35\cdot10^{-10}$	$1.35\cdot10^{-09}$						
R9	IM	$5.40\cdot10^{-10}$	$1.08\cdot10^{-09}$	$5.23\cdot10^{-10}$	$2\cdot10^{-10}$	$7.92\cdot10^{08}$	$1.27\cdot10^{09}$	$7.90\cdot10^{08}$	7.02
	Z	$4.25\cdot10^{-10}$	$1.38\cdot10^{-09}$						

Table 4 gathers all the values, i.e., self-diffusion coefficients ($D_{i/THF}$) calculated with Stokes-Einstein equation (Eq. 10), the diffusion coefficient obtained with the Smoluchowski equation (Eq. 8), the diffusion rate (k_{diff}) and the new rate constants ($k_{app,+}$). Also, we can observe in Table 4 that the new energy barriers $\Delta G^{\ddagger}$ are not as high, so these corrections do not change significantly our REP. However, the effect on the overall kinetics is not negligible. We carried out the kinetic simulation with these new rate constants, and Figure 4-4 shows the results of this kinetic analysis. Under this new scenario, the reaction achieves full conversion at 40000

seconds, this is about 11 hours. This result is more similar to the experimental outcome, but still the overall kinetics is too fast. These concentrations actually affect the overall kinetics, but there are many uncertainties in the evaluation of the diffusion rates. We noted that **R9** is the reaction that is most affecting the rate since it involves mono-phosphine/bis-phosphine exchange, and as we will see bellow, taking into account these processes are essential.

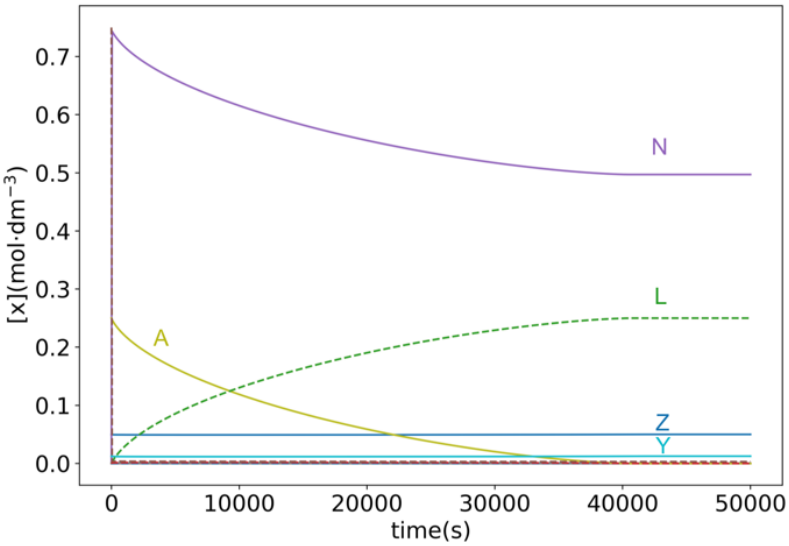

Figure 4-4. Concentration vs time profile of relevant species in the aryl borylation reaction considering diffusion effects $[A]_0$=0.25M; $[Z]_0$=0.05M; $[Y]_0$=0.0125M; $[C]_0$=0.75; $[D]_0$=0.75.

4.3.3. Kinetic Effects considering Competitive Reactions

In the previous chapter, we described several reaction pathways that the aryl borylation reaction can follow. We explored all possible intermediates involving bis-phosphine and also mono-phosphine complexes, and also some neutral and ionic species. All those species could thus be present in the reaction media and exchange rapidly. In the kinetic modelling presented above in this chapter, we only considered the most favourable of the

mechanisms among all other pathways. However, those other alternative pathways actually involve equilibria with most of the species already included in the kinetic modeling above, so they must be viewed as competitive reactions. Inclusion of these competitive reactions might modify the concentration of the intermediate species and, consequently, affect the overall rate of the reaction. For these reasons, we decided to consider in the kinetic analysis those competitive reactions, and analyse how they influence the kinetics.

To see clearly which reaction influences the most the reaction rate, we proceeded by adding, one-by-one, additional equilibria to the kinetic simulation. We started with the bis-phosphine/mono-phosphine exchange, and then we added the other reactions with the different possible transmetalation steps. The additional reactions are listed in Figure 4-5. Reaction **R10** is the *cis/trans* isomerization of the oxidative addition bis-phoshine product; reactions **R11-R12** correspond to phosphine decoordination; reaction **R13** is the reductive elimination in the bis-phosphine complex; reaction **R14** oxidative is the addition coupled with phosphine decoordination; reaction **R15** is an adduct formation; **R16** is boryl transfer with Na^+; **R17** describes the decoordination of the by product to bis-phosphine; reaction **R18** forms first adduct without Na^+; reaction **R19** forms the second adduct without Na+ in mono-phosphine complex; reaction **R20** is a boryl transfer without transmetalation in mono-phosphine complex; reaction **R21** is by product formation; reaction **R22** forms the second adduct without Na^+ coupled with phosphine dissociation; reaction **R23** boryl transfer without Na^+ coupled in bis-phosphine; **R24** describes another formation of the product to bis-phosphine; reactions **R25**, **R26** and **R27** corresponds to the first diboron adduct formation, boryl transfer and reductive elimination in mono-phosphine complexes, respectively; and reaction **R28**, **R29** and **R30** are equivalent reactions to the latest but in the presence of phosphine.

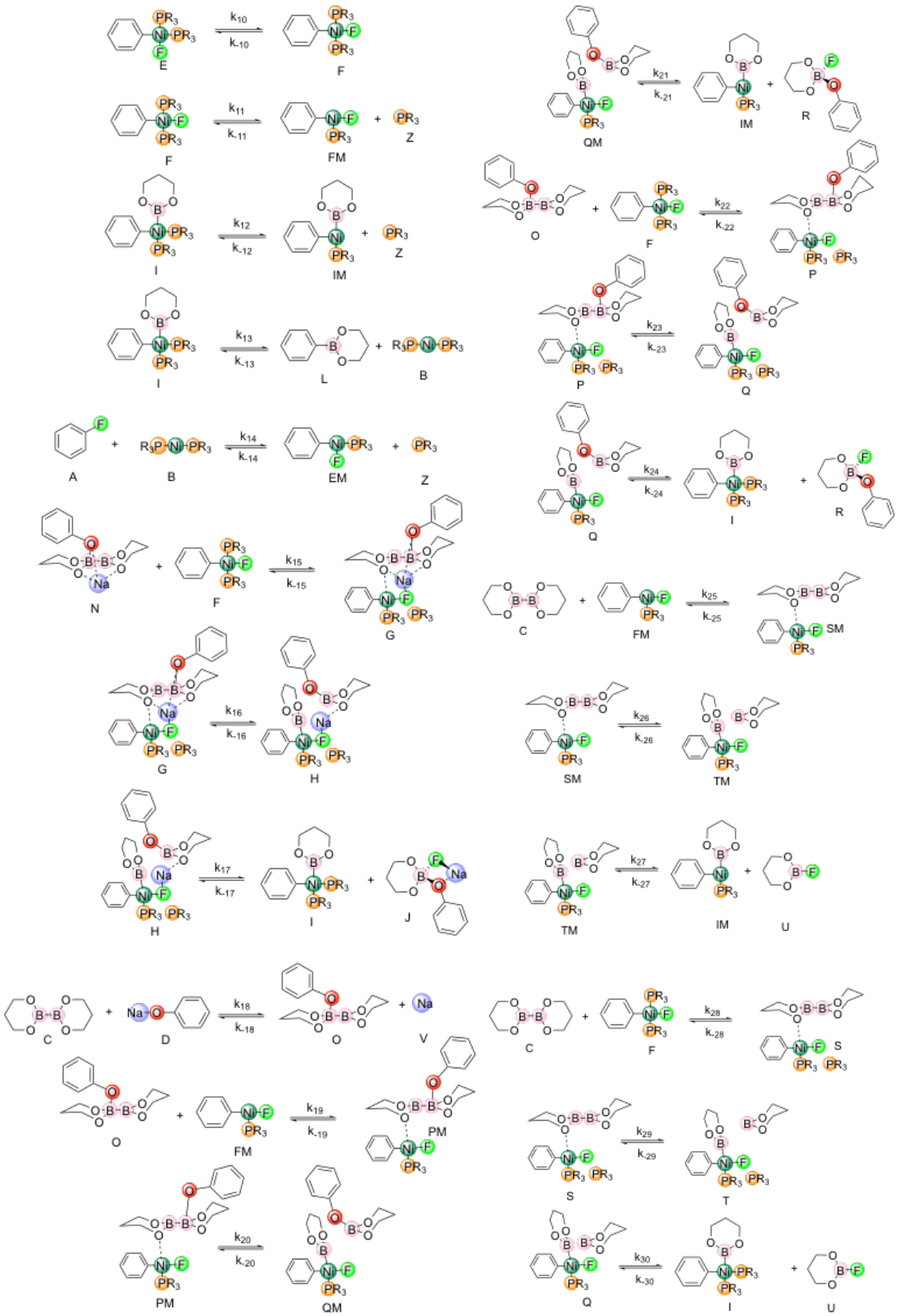

Figure 4-5. Additional elemental reactions included in the kinetic modeling.

Then, the kinetic modeling was carried out by including successively all the reactions ordered by groups. Firstly, reactions **R10-R13**, which describe the main exchange between mono- and bis-phosphine complexes. These strongly influenced the computed total conversion time. In fact, when we considered the bis-phosphine/mono-phosphine exchange, the computed total conversion time increases from 8000s (2.2 h) till 64000s (17.8 h). That could be explained since first *cis/trans* isomerization barrier is higher in the bis-phosphine than in the mono-phosphine complex because the bis-phosphine compounds are more stable than the mono-phosphine species.

Additionally, phosphine is in high concentration, in excess actually, in the reaction media thus favouring the formation of bis-phosphine compounds. Consequently, the reaction becomes slower because dephosphination has a high barrier to go from a stable species to a less stable one.

Table 5. Time of total conversion of the kinetic analysis adding possible competitive reactions.

Alternative Reaction Considered	Reactions Added	Time Total Conversion (s)
Mono-Bi-phosphine interchange	R10-R13	64000
Oxidative Addition Mono-phosphine	R14	65000
Adduct Bis-phosphine	R15-R17	65000
Adduct without Na+ (mono+bis-phosphine)	R18-R24	65000
Classic trans-metallation (mono+bis-phosphine)	R25-R30	65000

Adding **R14** to the kinetic modelling, this the oxidative addition reaction to the mono-phosphine complex, just increase the total conversion time 1000s more. Contrarily, the additional competitive reactions **R15-R17**, **R18-R24** and **R25-R30** does not alter the kinetics. These results show that the only competitive reactions that affects the overall reaction rate is the bis-

phosphine/mono-phosphine exchange. This is so because those other additional reactions have high energy barriers so they do not take place in a significant extend actually.

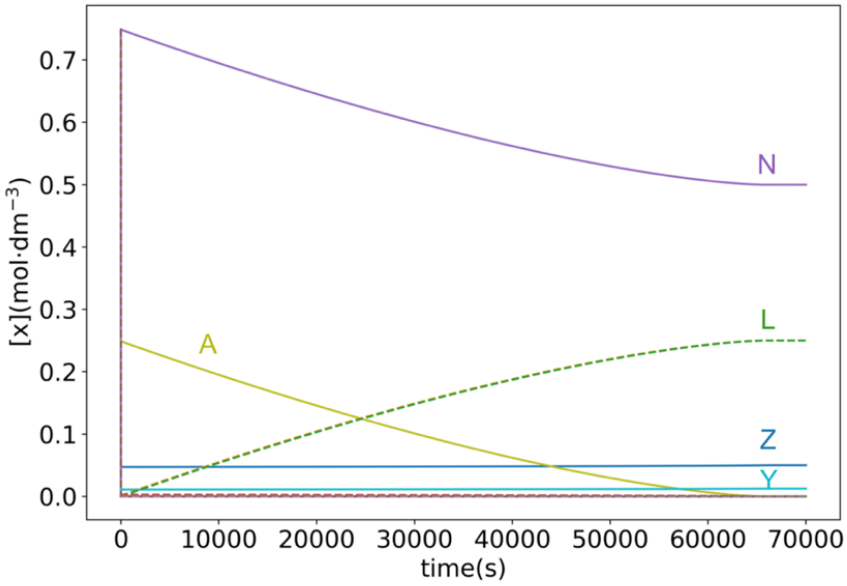

Figure 4-6. Concentration vs time profile of relevant species in the aryl borylation reaction considering reactions ***R1-R13****. $[A]_0$=0.25M; $[Z]_0$=0.05M; $[Y]_0$=0.0125M; $[C]_0$=0.75; $[D]_0$=0.75.*

Figure 4-6 plots the concentration versus time graph of the aryl borylation reaction considering the bis-phosphine mono-phosphine exchange reactions reactions **R1-R13**. It is important to note that after 12h (43200s) the product yield reaches 80%, a value very close to that reported in literature.[14] These results are much closer to the experimental data than the results obtained considering the diffusion effects.

As mentioned above, and as we have seen in Figure 4-5, the kinetic modeling of such a system becomes more and more complex as the connections among species increases. A good way for visualizing the complexity of the system and its species interconnection is the use of a Chemical Reaction Network (CRN), in which we can represent all species that participate in the system as well as the connections between them. Figure 4-7 is an example of a CRN of our system when we contemplate the 30 reactions in the system (Figure 4-5). In Figure 4-7 the species are represented

with circles and the reactions with squares. Also, a CRN indicates if the species participate in the reaction as reactants or as products. If the species is a reactant the line that connects it with the square is a dashed line. If, on the other hand, the species is a product, the line connecting to the square is a solid line. This is not only a good way to see a map of the reaction, but also a good way for automatizing the kinetic simulations.

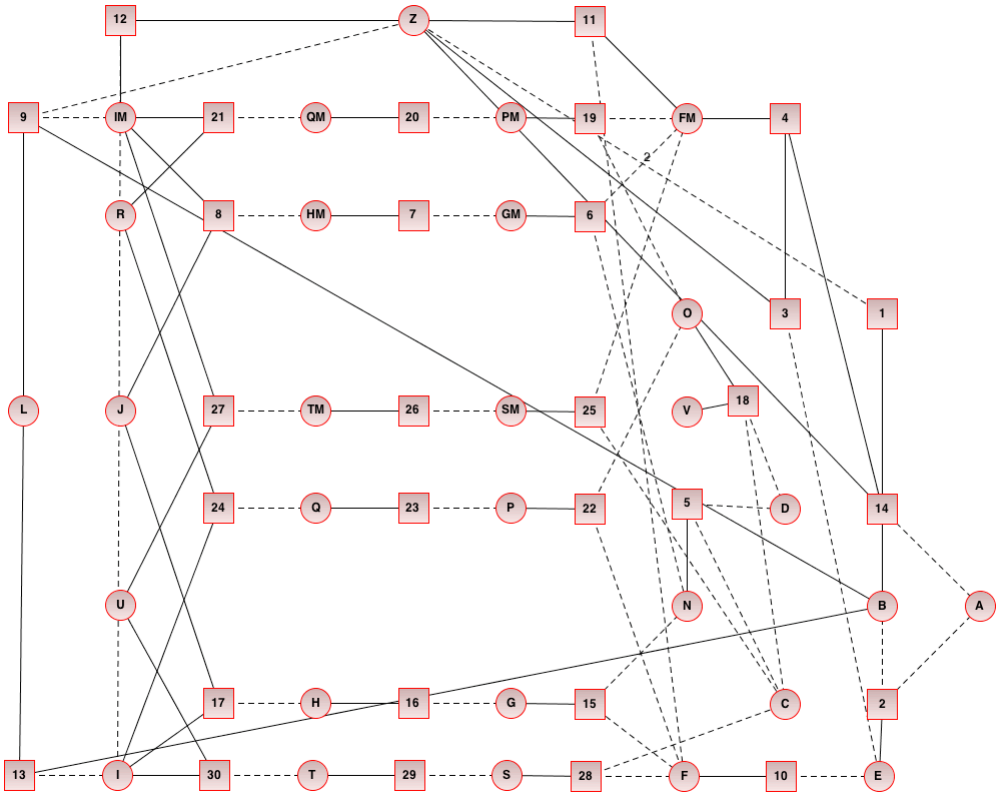

Figure 4-7. Chemical Reaction Network constructed using CoNtroL tool.[96] *Circles represent the species that participate in the reaction. Squares indicate reactions, which connect reactants (dash lines) with products (solid lines).*

Given that the bis-phosphine/mono-phosphine exchange affected significantly the overall reaction rate, it is interesting to study how the initial concentrations of phosphine, and of the base, push the reaction and force the displacement of the chemical equilibria. This effect will be studied in the next section along.

4.3.4. Effect of the Concentration of Ligand and Reactants

As we just mentioned, changes in the initial phosphine concentration are expected to modify the overall reaction rate. We can study these effects by implementing different initial concentrations in the kinetic modelling. In particular, we think that is even more interesting to see how the rate is affected by changes in concentrations of those reactants in excess. Clearly, modifying the concentration of limiting reagents will affect the rate. However, it is not obvious how the initial concentration of reagents in excess will affect the rate. Besides phosphine concentration, in this reaction it also matters the concentration of the sodium phenolate.

For investigating how concentrations affect the rate, we took the model of the favourable mechanism without diffusion effects but taking into a count the bis-mono-phosphine exchange, so reactions **R1-R13**, as reported in the previous section (4.3.3) and we change the concentration of the specie of interest. Initial concentrations of the species were for substrate **A**: 0.25mol·dm^{-3}, for phosphine **Z**: variable from 0.1mol·dm^{-3} to 0.01mol·dm^{-3}, see more details at Table 6, for pre-catalyst **Y**: 0.0125mol·dm^{-3}, for diboron **C**: 0.75mol·dm^{-3}, and, finally for sodium phenolate **D**: 0.75mol·dm^{-3}.

*Table 6. Total conversion time for different initial concentrations of phosphine (**Z**), concentration of **B** at different reaction times (t=54s and at total conversion), and concentration of **F** at t=54s.*

[Z] (mol·dm^{-3})	Time total conversion (s)	[B] at 54s (mol·dm^{-3})	[B] total conversion (mol·dm^{-3})	[F] at 54s (mol·dm^{-3})
0.1	40000	$4.24 \cdot 10^{-08}$	$5.49 \cdot 10^{-05}$	$1.36 \cdot 10^{-06}$
0.075	50000	$3.53 \cdot 10^{-08}$	$4.53 \cdot 10^{-05}$	$8.72 \cdot 10^{-07}$
0.05	65000	$2.71 \cdot 10^{-08}$	$3.46 \cdot 10^{-05}$	$4.71 \cdot 10^{-07}$
0.025	100000	$1.86 \cdot 10^{-08}$	$2.18 \cdot 10^{-05}$	$1.84 \cdot 10^{-07}$
0.01	190000	$9.17 \cdot 10^{-09}$	$1.18 \cdot 10^{-05}$	$6.04 \cdot 10^{-08}$

Total conversion times considering different initial concentrations of phosphine were computed and results collected in Table 6. Initial phosphine concentration shows a big effect on the kinetics of this reaction. From the initial value 0.05 mol·dm^{-3}, by increasing phosphine concentration the reaction rate increase too since the total conversion arrives earlier. On the other hand, if we decrease the initial phosphine concentration the reaction becomes slower. This not clear how to rationalize this since phosphine excess shifts the mono-phosphine/bis-phosphine exchange to bis-phosphine compounds, which are more stable, but some have higher barriers. We analyzed the concentrations of relevant species at different reaction times and found that the concentration of **B**, the catalyst resting state $Ni(PR_3)_2$, follows the same trend as the phosphine concentration (Table 5). The concentration of **B** at t=54s is low and it is higher for high phosphine concentration. Same happens with **F**, the bis-phosphine intermediate prior the reductive elimination, whose concentration is higher than **B** and also decreases when the phosphine concentration decreases. Therefore, the overall rate increases when the phosphine concentration increases because the concentration of the Ni/phosphine relevant catalytic species also increases. Phosphine excess thus provide a larger amount of Ni species available for catalysis.

In the experimental study[14] and during the course of the reaction conditions optimization, it was reported that when half of the phosphine was used (0.025M), the reaction reached 54% yield after 12h. In our study, when the initial concentration of phosphine 0.025M was used (Table 6), we evaluated that the 54% yield would be obtained at 42600s (11.8h), that is very similar to the experimental results.

In light of this, we decided to evaluate whether the relative stability of mono-phosphine and bis-phosphine compounds has kinetic relevance. These experiments consist in “modifying” the relative energies by first, changing the energy of the bis-phosphine intermediates at the same energy than the mono-phosphine, and

second, upside down, considering de mono-phosphine intermediates as stables than bis-phosohine intermediates. Then, compare how change the reaction rate. When we changed the energy of the bis-phosphine compounds making them less stable, we found that the velocity increases. Otherwise, when we changed the energy of the mono-phosphine compounds and make them more stable, the velocity is unaltered. That allows us to think that the reaction always there is the participation of the bis-phosphine compounds. Additionally, these results confirm our hypothesis of the participation of competitive reaction in the mechanism explained in section 4.3.3.

We observed that from the results in Table 6, this is from the relation between the initial concentration of phosphine and the reaction rate, a kind of reaction order can be extracted. If we plot the initial concentration of phosphine vs the time at 100% conversion, which is a measure of the inverse of the reaction rate, an exponential negative trend should be observed, being the value of the exponent the negative reaction order, as Figure 4-8 shows.

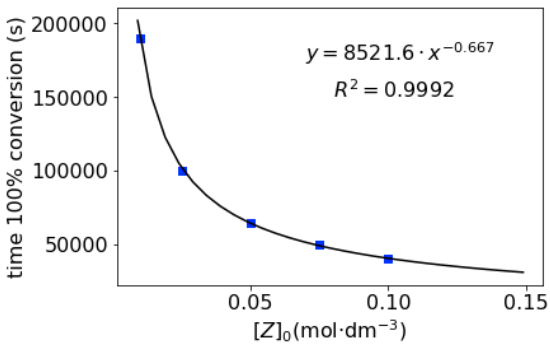

*Figure 4-8. Initial concentration of phosphine (**Z**) vs total conversion time plot with the corresponding potential regression with an R^2=0.9992.*

In Figure 4-8 we can see that the relation between the initial phosphine (Z) concentration and the time of total conversion fits perfectly the equation, so it would indicate that the order of the reaction with respect the phosphine is 0.667. This value would

indicate a complex reaction mechanism, but the way we just evaluated it is rather approximate. The way of measuring the reaction rate from the total conversion time is questionable, and it is improvable. With this example we wanted to demonstrate how to obtain kinetic data directly comparable with experiments from computational mechanistic studies.

*Table 7. Total conversion time for different initial concentrations of sodium phenolate (**D**).*

	[X](mol·dm^{-3})	Time total conversion (s)
D Sodium Phenolate	0.75	65000
	0.5	65000
	0.25	65000
	0.2	45000
	0.1	20000

We also studied the variation of the kinetics by varying the sodium phenolate initial concentration (see Table 6). From the initial value of 0.75 mol·dm^{-3}, we observed that the kinetics does not change when we decrease the concentration until the concentration is lower than the limiting reactant, and then the reaction becomes slower. These results indicate that it is really not necessary to have sodium phenolate in excess, since the reaction rate would keep high unless sub-stoichiometric concentrations are used. Therefore, according to our kinetic modelling, sodium phenolate is used in excess because its low solubility in THF.

4.4. CONCLUSIONS

In this chapter, we presented the microkinetic study of the borylation of aryl halides reaction, for which we determined its mechanism in the previous chapter.

We started the study taking the results of the most favourable mechanism of the DFT study of Martin reaction[14]. The results obtained suggested that some crucial aspects, affecting directly

the reaction rate, had probably not been taken into account in our model.

In order to improve results, we considered diffusion effects for the fastest and barrier-less bi-molecular reactions. The results obtained considering the diffusion effects are better than the ones without, but not fully satisfactory. We considered, also, competitive reactions that occurs in parallel to the most favourable mechanism. By analysing separately, the different alternative processes, we found that the process that change the reaction rate the most is the *cis*/*trans* isomerization of the intermediates.

Moreover, we explored how the phosphine and sodium phenolate initial concentrations affect to the rate reaction. We have seen that if we increase the phosphine initial concentration, the rate reaction increases. This change of concentration affects directly to the catalyst formation elemental step, as higher amount of phosphine more catalyst is formed. However, when we make the same study for the sodium phenolate initial concentration the results showed no modifications in the rate concentration until lower the limitan reactant concentrations. We thought that the reason that the phenolate is in excess is to avoid the low solubility in the solvent.

"Imagination is the Discovering Faculty, pre-eminently. It is that which penetrates into the unseen worlds around us, the worlds of Science." Ada Lovelace

CHAPTER 5

5. *NI/ CU-CATALYSED ARYL BORYLATION*

5.1. INTRODUCTION

The large presence of fluorocarbons in nature and its great stability encourage science community to found new methods to break the C-F bond of this compounds, because it could be used as a starting reactant in organic synthesis. The stability of aryl fluorides is given because its C-F bond is the strongest single bond

in the nature. That is its principal characteristic and the reason of it lack of reactivity.[63] For this reason, it is challenging for scientists found the manner for C-F cleavage. Remarkably aryl fluorides show an extraordinary metabolic activity, and this makes them especially attractive in the pharmaceutical industry.[64]

As mentioned in previous chapters, Hosoya's[15] and Martin's[14] groups reported an efficient C-F bond cleavage reaction via Ni-catalyst borylation, incited by the versatility and pivotal role of organoboron reagents (Figure 3-1). Later, other groups presented different variations of this borylation reaction testing different salts, catalysts, ligands and diboron agents.[18–21,29–31,65] Borylation of C-X bonds is therefore a topic of current interest that makes a computational study attractive. There are plenty of open questions regarding the mechanism, about the role of the base, and the reaction conditions.

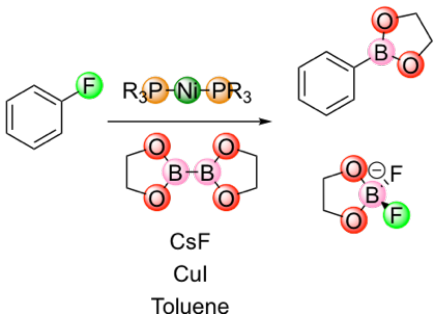

Figure 5-1. Scheme of the reaction proposed by Hosoya group[15].

In this chapter we present the computational study of Hosoya's reaction (Figure 5-1).[15] In a first glance, this reaction looks very similar to Martin's reaction. However, the participation of a copper salt, such is CuI, suggests that the mechanism is more comlpex. Therefore, we attempted to unveil the role that copper plays in this reaction, and to that, we contemplated several possibilities, namely, CuI as co-catalyst, or as a catalyst instead of nickel. Also,

we were interested whether the CsF salt behaves similarly to NaOPh in Martin's reaction.

5.2. Computational Details

All the calculations in this work were carried out using Gaussian 09[66] software. B3LYP[43,44,69] DFT level is used with the density functional dispersion correction D3[70] that takes into account non-covalent interactions. All the geometric structure optimizations, vibrational frequencies, and energies were calculated using the 6-311G** basis set[67] for atoms C, H, B, O, F and P; for Ni, Cu and Cs we have used the LANL2DZ basis set[67], which includes the effective core potential ECP. We included the SMD[47] solvent model for the solvent Toluene. Thermal corrections were evaluated at 298K. As well, we have used M06-2X[68] and ωB97XD[45] DFT methods to compare with B3LYP-D3[43,44,69,70] at the same conditions. All TS structures were additionally characterized by the corresponding IRC calculation. A data set collection of computational results is available in the ioChem-BD repository[81] and can be accessed via https:// doi.org/10.19061/iochem-bd-1-134.

5.3. Results and Discussion

The goal of the present study is to elucidate the mechanism of the borylation reaction of aryl fluorides catalysed by nickel complexes introduced by Hosoya's group.[15] This is very similar to Martin's reaction[14], but instead of NaPhO, this new reaction is assisted by CsF and CuI salts. As we have seen in other chapters, we might guess that CsF will act as a base, interacting with the diboron agent and form a stable adduct. However, in the Hosoya reaction, we found a new participant, CuI. The role of this iodine copper complex is unclear, and leads us to think that the reaction mechanism could be more sophisticated than the studied in previous chapters. We have two hypotheses for this new reactant. Our first hypothesis is that CuI could help in the transmetalation

step. Another possibility is that copper is the real catalyst and the nickel complex is a mere spectator. For this reason, we have carried out electronic structure calculations at the DFT level to explore the role of CuI in this reaction.

5.3.1. C-F Oxidative Addition

The catalytic cycle starts with the C-F oxidative addition. In this step, the metal atom of the catalyst moves into the C-F bond of the substrates. This action oxidases the Ni(0) to Ni(II) and breaks the aryl's C-F bond. Given that the catalyst and the aryl are the same as in Martin's reaction[14] (Chapter 3), we expect similar results since the only difference between the two reactions is the solvent, THF in Martin's reaction and toluene in Hosoya's reaction.

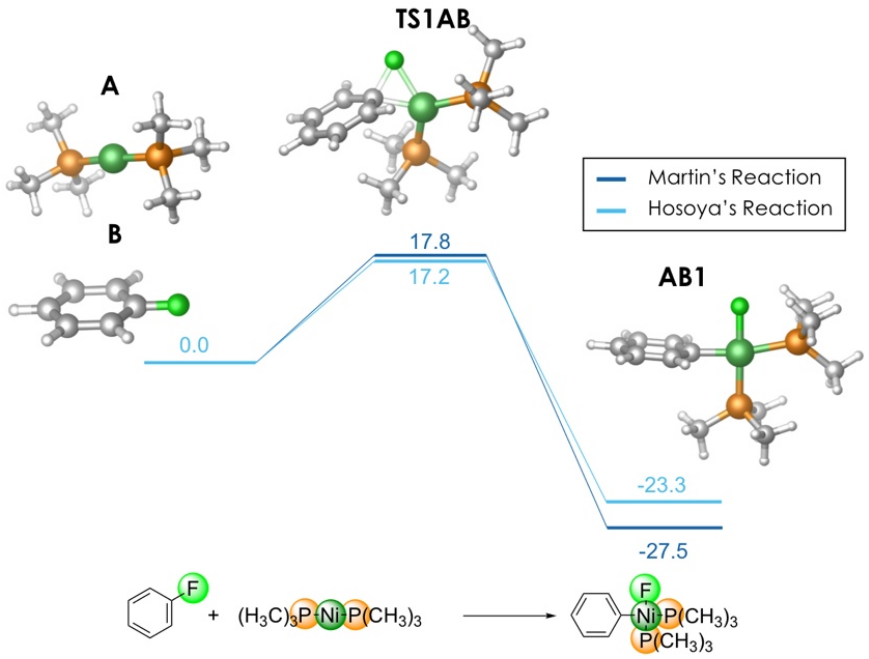

Figure 5-2. Free energies for the oxidative addition step. Light blue: Hosoya's reaction in toluene. Dark blue: Martin's reaction in THF.

We have carried out full geometry optimization of the reactants, the transition state (TS) and the products for this oxidative addition. Figure 5-2 shows the molecular model of the reactants (**A** and **B**), TS (**TS1AB**) and product (**AB1**). **TS1AB** represents the TS of this oxidative addition where the three-center C-Ni-F

arrangement is clearly identified. This TS gives the **AB1** product where the Ni(II) displays a square planar shape. Figure 5-2 depicts also the free energies of the oxidative addition of Hosoya's reaction (light blue). This data shows that the reaction is feasible with a barrier of 17.2 kcal·mol^{-1}, and that reaction is exergonic because the product obtained is more stable than the reactants. Moreover, comparing these results for the Hosoya's reaction with those for the Martin's reaction, there not are significant differences between the two solvents (17.2 kcal·mol^{-1} vs 17.8 kcal·mol^{-1}). The lower polarity of toluene affected the product in a larger extend than the TS. Since the dipole moment of **AB1** (9.99D) is larger than that of **TS1AB** (6.25D), the more polar THF solvent stabilizes more the product than the TS.

5.3.2. *CIS/ TRANS* ISOMERISATION

The reaction step following the oxidative addition is an isomerisation. The isomerisation consists in the pass from a structure where the two phosphine ligands are in *cis* disposition to a structure with the phosphines in *trans*. The molecular model of the isomer *cis*, isomer *trans* and the isomerisation TS are presented in Figure 5-3. In Figure 5-3 we can observe that the shape of the bis-phosphine TS is similar to a mono-phosphine TS (**TSAB1M**) because one of the phosphine ligands are completely unlinked. Both molecular models, **TSAB1** and **TSAB1M** in Figure 5-3, have a trigonal planar shape. Moreover, both structures have similar angles.

The diboron agents in the presence of Lewis base forms a B(sp2)-B(sp3) adduct, as previous studies in our group indicates.[74] In this adduct, the B-B bond is longer than the isolated diboron species. Additionally, in the adduct the boron linked to the base directly becomes positively charged, therefore, the other boron turns into the negatively charged atom. Consequently, the Lewis base activates the diboron agent and a boryl unit could be transferred to unsaturated substrates via metal-free reaction.[74]

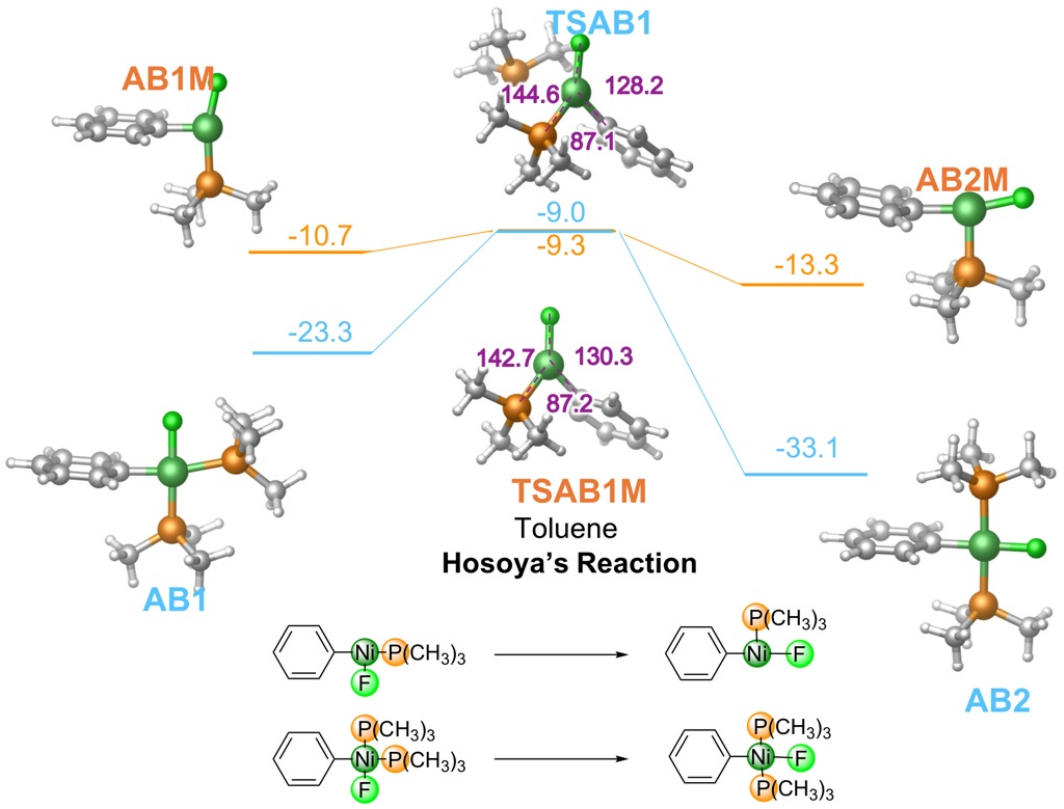

Figure 5-3. REP of mono-phosphine (orange) and bis-phosphine (blue) isomerisation of Hosoya's reaction. The angles of the TSs are represented in purple.

The B(sp2)-B(sp3) adducts had not been characterised by X-Ray until 2015 when Marder and co-workers reported the structures for this type of adducts. They characterised the adduct formed by the B_2pin_2 diboron and KO^{t}Bu salt,[78] and also the B_2pin_2/NMe_4F adduct[78]. This latter is very close to the adduct that will probably be formed between B_2pin_2 and CsF under Hosoya's reaction conditions. In the X-Ray structures, it was seen that the boron linked directly to the Lewis base gets a tetrahedral shape, whereas the other boron is still being a trigonal-planar shape. Moreover, they found that the counterion is coordinated to the other oxygen atoms of the diboron agent.

After these shreds of evidence, in Hosoya's reaction the next logical step would be the B-B activation with CsF, and as we will see below, this is indeed the case. However, the main question is whether CuI plays any role or not. For this reason, we made efforts to understand how CsF and CuI salts could work together trigering the boron transmetalation.

Actually, in the chemistry of copper is known that CuCl, in the presence of CsF, forms $[CuX_2]^-$ type complexes in water stabilising the Cu(I) oxidation state[97] Therefore, a kind of [CuFI]$^-$ compound could activate the B-B bond by forming the adduct diboron/[CuFI]. Moreover, the presence of Cu in this adduct could also help breaking the B-B bond. To explore this, we have carried out a DFT study on this sort of processes.

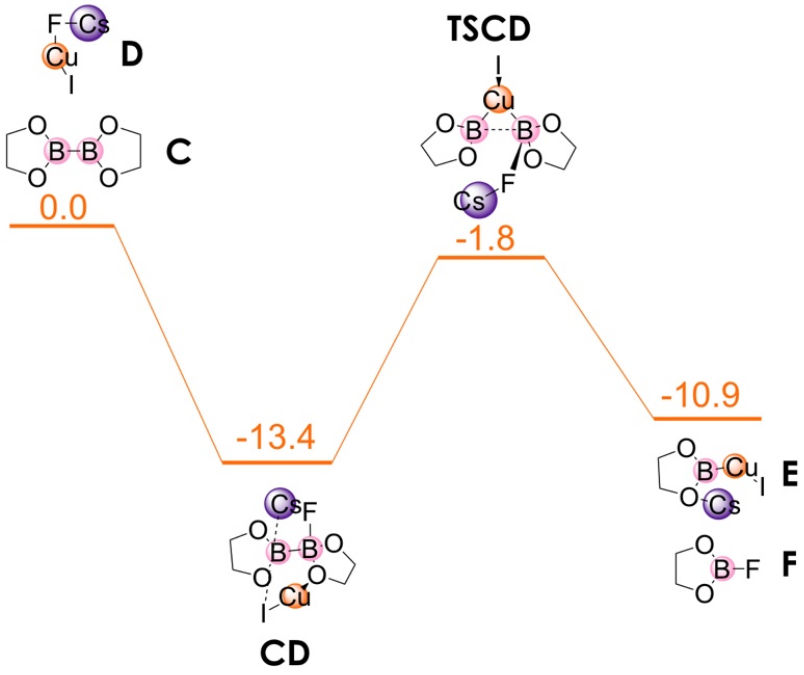

Figure 5-4. B-B activation with [CuFI]$^-$ and B-B bond break REP .

We found that the formation of Cs[CuFI] (**D**) is highly favoured by 50 kcal·mol^{-1}, being this species much more stable than the

reactants CuI and the CsF. That would confirm the stability of this adduct Cs[CuFI] when the CuI is in the presence of CsF. After that, it follows the formation of the diboron/Cs[CuFI] adduct, and then the breaking of the B-B bond. Figure 5-4 illustrates the energy profile of the species characterized computationally. The formation of the diboron/Cs[CuFI] adduct (**CD** in Figure 5-4) is a spontaneous reaction with a product more stable than the reactants by 13.4 kcal·mol^{-1}. Although the fluoride anion is bonded to Cu(I) in **D**, in the adduct **CD** it is not. The geometry of **CD** looks more similar to an adduct diboron/CsF/CuI than to a direct complex **C**/**D**. Extensive conformational exploration lead to that result.

Then, **CD** adduct can indeed easily progress with the B-B bond breaking through an intramolecular rearrangement. The B-B scission happens through **TSCD**, having an activation energy of 11.6 kcal·mol-1 as we can see in Figure 5-4. This reaction gives two products (**E** and **F** in Figure 5-4). **E** corresponds to the product where the boron negatively charged (boryl) is bonded to the CuI and the caesium cation is coordinated with the oxygen of the boryl and the iodine. On the other side, **F** corresponds to the byproduct, that is the second boron atom ended bonded to the fluorine, consequently with its formal positive charge. Therefore, these results suggest that CuI can effectively perform the B-B bond activation by breaking the B-B and generating a potentially catalytically active Cs[Cu(I)IBpin] species.

The next step is thus the transmetalation, i.e., the exchange of the fluorine ligand in the Ni(II) intermediate **AB2** or (**AB2M**) with the boryl group in the Cu(I) complex **E**. Then, the transmetalation step is the reaction between **AB2** or (**AB2M**) and **E**.

The transmetalation starts with the interaction of the copper atom in **E** with the fluorine atom in **AB2**. Figure 5-5 depicts the molecular models of the species that participate in the transmetalation. **E** plus **AB2** form compound **G**, which through **TSG** giving **G1**.

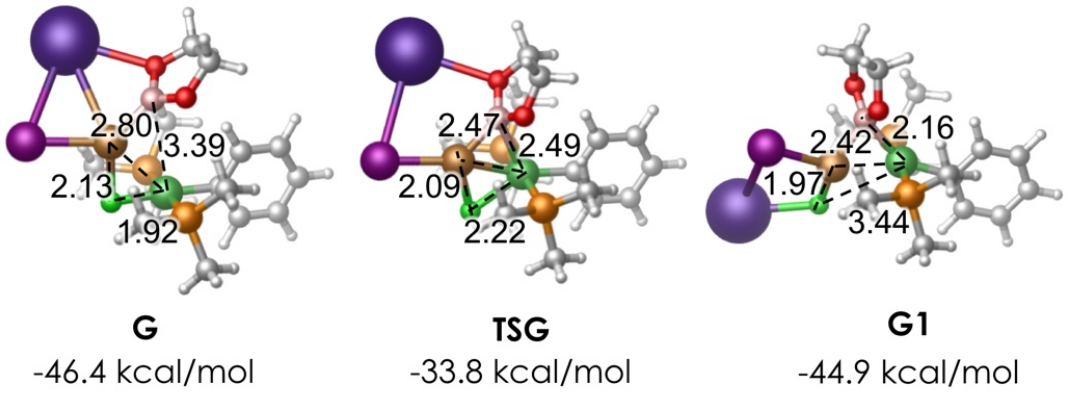

G
-46.4 kcal/mol

TSG
-33.8 kcal/mol

G1
-44.9 kcal/mol

Figure 5-5. Transmetalation species molecular model with their bond distances in black.

Figure 5-5 also illustrates the bond distances between the atoms that react. If we observe the different metal-F and metal-B bond distances in the transmetalation we can observe the exchange fluorine/boron, as the fluorine moves from the nickel to copper while the boryl transfers from the copper to nickel. On one hand, we can observe that the Cu-F bond distance decrease from **G** (2.13 Å) to **G1** (1.97 Å) and consequently, the Ni-F distance increase from **G** (1.92 Å) to **G1** (3.44 Å). On the other hand, the Ni-B distance decrease along the reaction, from **G** (3.39 Å) to **G1** (2.16 Å), however, this effect does not happen with the Cu-B distance that becomes smaller in **G1** (2.42 Å) than in **G** (2.80 Å).

The structures presented in Figure 5-5, in particular **G1**, are rather special, since it might feature a Ni-Cu metal-metal bond. For this reason, we analysed the electronic structure of **G**, **TSG** and **G1** under the framework of the topological analysis of the electronic charge density (ρ), the Laplacian of the electron density map ($\nabla^2\rho$), and non-covalent interactions (NCI). Figure 5-6 shows electron density maps (ρ), which basically show that almost all atoms involved in the reaction (Ni, B, F, Cu, and I) lie in the same

plane, the plane of the maps. It is worth noting that this coplanarity is kept from **G** to **TSG** and to **G1**.

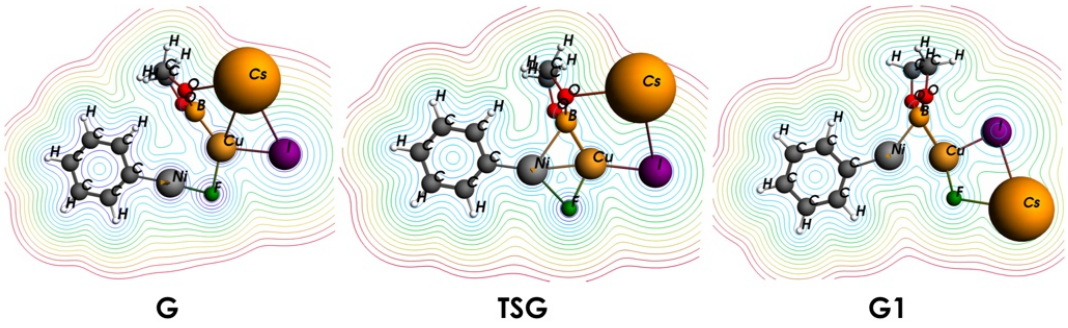

Figure 5-6. Electron Density map (ρ) of transmetalation participating species. The phosphine ligands (perpendicular to the plane) not plotted to facilitate the visualization.

In the topological analysis of the electron density introduced by Bader[48] the eigenvalues and eigenvectors of the Hessian of the electron density at the critical point permits its characterization. By this way, we found absolute maxima critical points CP (3,-3) for the atoms, the saddle point (3,-1) corresponds to a bond; the (3,+1) critical points correspond to rings in the molecule; and absolute minimum CP (3,+3) indicate the presence of a cage. Figure 5-7 shows the electron density topology (critical points and bond-paths) of the intermediates **G** and **G1**, and **TSG**. Figure 5-7 confirms the bonds between atoms suggested by the electron density maps above. Clearly only in **TSG** a (3,-1) Ni-Cu bond critical point could be characterized. Moreover, in Figure 5-7 we can observe a number of non-covalent bonds diboron/C-H_{ligand} and C_{aryl}/C-H_{ligand} highly curved, as banana bonds. This fact indicates a intricate web of non-bonding interactions between the ligand and the substrate, which could explain the critical choice of the diboron in some cases.

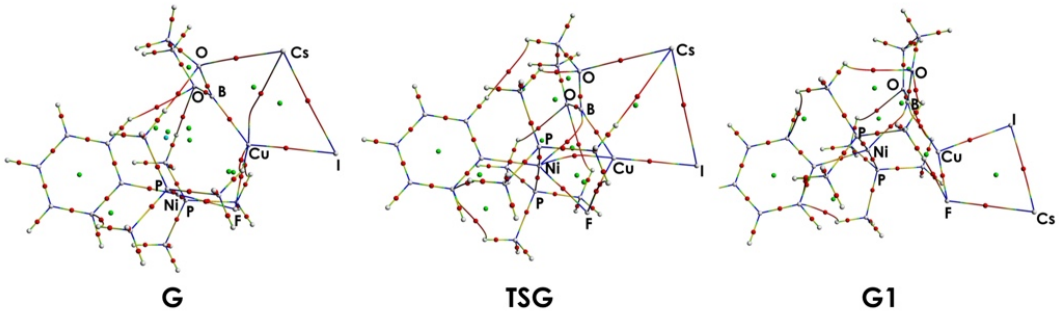

Figure 5-7. Electron density topology of the transmetalation intermediates and TS. Grey points: atoms (3,-3); red: bonds (3,-1); green: rings (3,+1); blue: cages (3,+3).

The Laplacian of the electron charge density is the scalar derivative of the gradient vector field of the electron density, the quantity $\nabla^2\rho$, and indicates where the charge is concentrated, $\nabla^2\rho<0$, and depleted, $\nabla^2\rho>0$. The local charge concentrations in the Laplacian provides a mapping with the number and position of electron lone-pairs according to the Lewis model. Figure 5-8 shows the Laplacian of the electron density of the transmetalation intermediates and TS. We can observe in Figure 5-8 the σ electrons of the aromatic ring, for instance, and the boryl lone-pair (yellow lines). The boryl group interacts with the cooper atom in **G**, and is easy to observe how from **TSG** to **G1**, the boryl lone-pair reorients to interact with copper and with nickel. Additionally, we can observe in Figure 5-8 that the fluorine in **G1** becomes less charged because is bonded to the caesium.

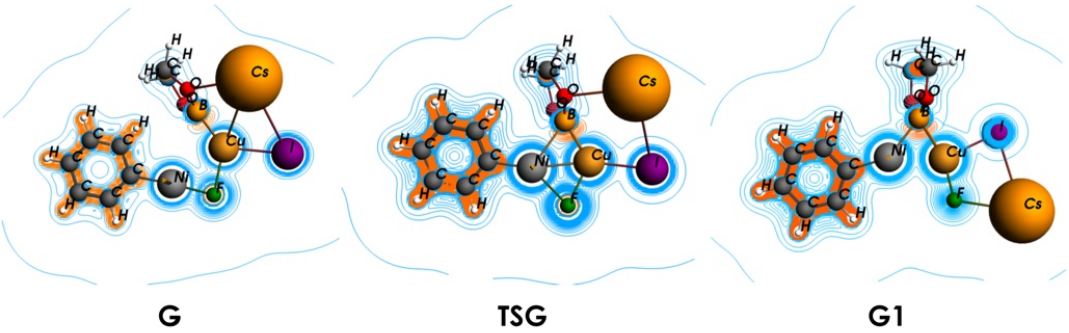

Figure 5-8. The Laplacian of the Electron Density map of the transmetalation participants. Negative values are represented in orange ($\nabla^2\rho<0$) and positive ones in blue ($\nabla^2\rho>0$). The phosphine ligands are obviated to facilitate the visualization.

The stabilising non-covalent interactions between different fragments in the transmetalation intermediates and TS were analysed in terms of noncovalent interactions (NCI) theory, as introduced by Yang and collaborators[49] In Figure 5-9 several stabilising interactions between the ligand and the aryl, within the ion pairs, and between the two metals, are clearly visible as coloured isosurfaces. Areas in green/yellow indicate attractive interactions, while areas in orange/red indicate strong non-bonded overlap. C-H/C-H interactions between the ligand and the aryl appear as localised spots in orange. However, the interaction between the ligand and the oxygens from the boryl (C-H/O) are yellow discs showing more attractive interactions than the C-H/C-H ones. The same yellow dishes are observed between Cs/O of boryl in **G** and **TSG**, and Cs/F in **G1**. It is of interest the green ring marked with a green arrow in Figure 5-9 representing the attractive interactions between the Cu/I.

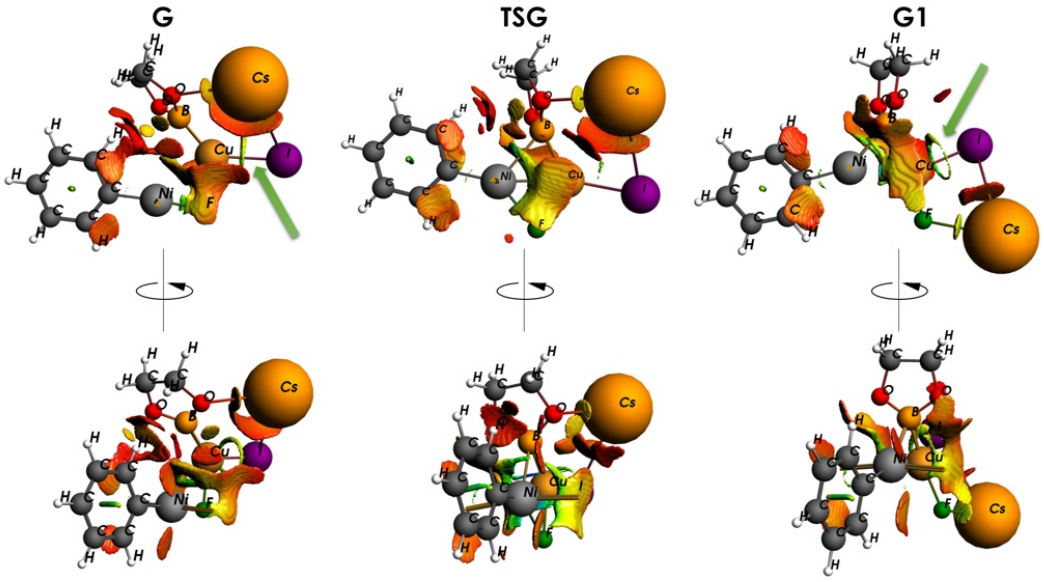

Figure 5-9. Noncovalent Interactions (NCI). Reduced density gradient isosurfaces (s=0.5) coloured according to the value of the second eigenvalue of the Hessian of the electron density for G, TSG, and G1 adducts. The colour scale indicates lamda2 values from 0.013 (red) to 0.05 (blue). The phosphine ligands are not shown to facilitate the visualization.

Once the interactions within these special set of species were analyzed, it lacks evaluating the energetics of the transmetalation step. As collected in Figure 5-5, the relative Gibbs energy of intermediates **G** (-46.4kcal·mol^{-1}) and **G1** (-44.9kcal·mol^{-1}), and the TS **TSG** (-33.8 kcal·mol^{-1}) indicates that this transmetalation step presents an activation energy of 12.6 kcal·mol^{-1}. This indicates that is a very favourable process, so the copper makes possible this mechanism for the transmetalation step. In the following section, we will study the reaction without the participation of the copper to see better this effect.

5.3.2.1. Diboron/CsF Adduct Formation without Cu participation

After having obtained strong proofs supporting the idea that the role that CuI could play in the transmetalation is not minor, it is still necessary to prove that the use of CuI improves the reaction rate. Then the diboron agent have to be activated by CsF only. We characterised the diboron/CsF adduct depicted in Figure 5-10 labelled **J1**. Figure 5-10 shows that the adduct **J1** molecular model closely ressembles that of Marder's results, in particular regarding the tetrahedral shape of the boron linked to the fluorine and the trigonal-planar coordination sphere of the second boron atom. Moreover, X-Ray data for the B-B distance (1.736 Å)[78] of a [nBu_4N][B_2pin_2] matches perfectly our results. The B-F distance (1.478 Å) also matches with our results. The X-Ray Cs-F and Cs-O bond distances are not available because the X-Ray data adduct has different counter ion, nBu_4N F distance is 4.47Å. The formation of this adduct is favourable in the free energy surface by -33.2 kcal·mol^{-1}.

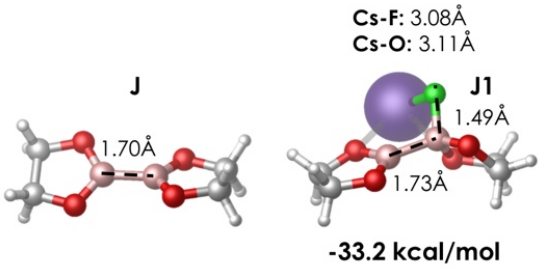

Figure 5-10. Molecular model of the diboron and the diboron/CsF adduct and its corresponding bond distances in black.

Despite intensive computational efforts, it was not possible to accommodate **J1** species nearby **AB2** in a reacting manner without observing spontaneous dissociation of one phosphine ligand. Consequently, the mono-phosphine **AB2M** complex was chosen instead, and it was found that **AB2M** interacted favourably with **J1** forming **JAB1** in Figure 5-11. The **JAB1** molecular model clearly the coordination of between cesium to both two fluorine atoms. Also, a Ni-O interaction in this adduct fixes the initial orientation of the diboron. All these interactions give high stability to this species, as much as -38 kcal·mol^{-1} in relative Gibbs energy. Also in Figure 5-11, **TSJAB1** molecular model shows clearly that the B-B bond is being broken and the new B-Ni bond is being formed. Analysis of **TSJAB1** molecular geometric parameters indicates that, in the TS, the caesium cation is interacting also with both fluorine atoms, one fluorine that coming from the diboron/CsF adduct, and the other one from **AB2M** intermediate, helping in the transmetalation.

From the relative free energies of **JAB1** and **TSJAB1**, this gives a barrier of 24 kcal·mol^{-1}. This value is higher than the one obtained for the Cu mediated transmelation, so at this point, we would conclude that copper contributes in the mechanism in an essential manner. In any case, the transmetalation has to end with decoordination of the byproduct and recovering of the phosphine, so to obtain the square-planar **H**, correspondent to **AB2** but with

the boryl ligand instead of fluorine. Then the reductive elimination proceeds from **H**.

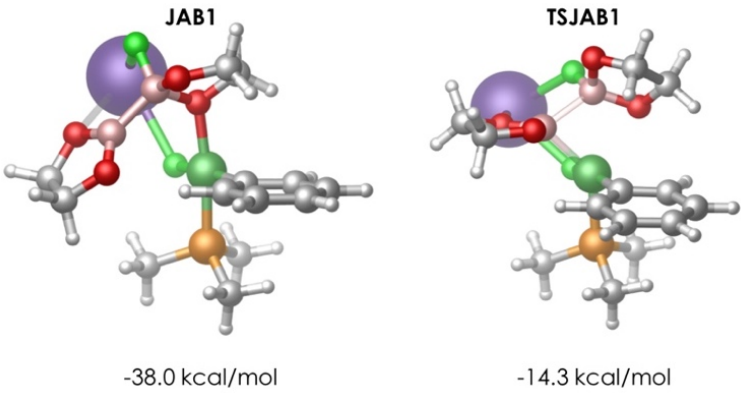

Figure 5-11. Adduct-Intermediate-Coordination and Transmetalation molecular models.

5.3.3. C-B Reductive Elimination

As mention above the step after the transmetalation is the reductive elimination. As in Martin's reaction, the reductive elimination occurs from the *trans* intermediate **H** has an intramolecular reaction and we obtain the desired product and we recover the catalyst. There is not a *trans*/*cis* isomerization.

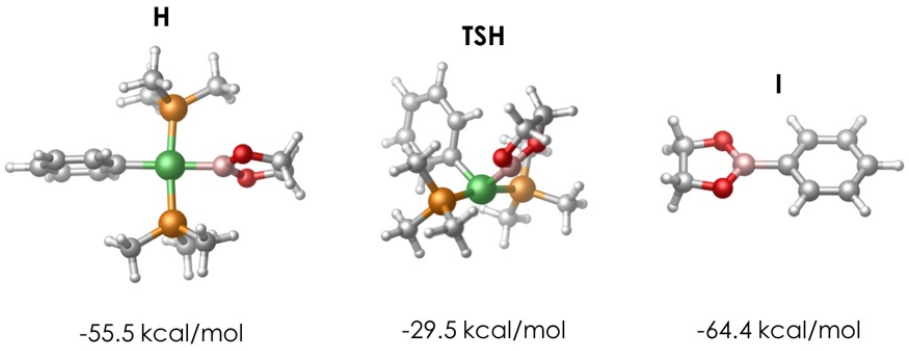

Figure 5-12. Molecular models of the reactant, TS and products of the reductive elimination step.

Figure 5-12 shows the molecular model of the reductive elimination step participants and their corresponding free energy. We can observe that the reductive elimination barrier is quite large (26 kcal·mol^{-1}). In previous studies (Chapter 3) we also found that the reductive elimination for bis-phosphine compounds showed a high barrier too.

5.3.4. Cu Direct Transmetalation

In 2017, so in the course of the realization of this work, Hosoya's group reported on the fact that the reaction works as well without nickel, only with a copper salt as metal catalyst and phosphine ligand[19]. Several copper salts, such as CuCl, CuBr, CuF_2, $CuCl_2$, $CuBr_2$, $Cu(OAc)_2$, and $Cu(OTf)_2$, efficiently catalysed the defluoroborylation, as they named the reaction. In contrast, using CsF as the base was crucial. Nonpolar solvents, such as toluene, benzene, and cyclopentyl methyl ether, were preferred. Similar to the bimetallic Ni/Cu system, bis(neopentyl glycolato)diboron $(Bnep)_2$ was unsuitable as the boron source.

Summarizing, the reaction proceeds with $(Bpin)_2$, the copper salt, phosphine ligand, or base. Under these experimental conditions, this borylation with copper only is very efficient, air-stable, scalable till decagramme-scale, and also applicable to di- and triborylation reactions.

Figure 5-13 depicts Hosoya's proposed mechanistic scheme to account for the role of the copper in the reaction. Note that, as the catalytically active species is supposed to be LCuCl (L=PCy_3), that in the presence of CsF forms the complex LCuF **K** in Figure 5-13, the oxidative addition of the fluoroarene seems unfeasible. As we demonstrated and discussed above, CuI/CsF can activate the diboron and carry out a transmetalation transformation giving ICu-Bpin.

It was proposed that **K** reacts with the diboron agent **C** and produces the heterolytic B-B bond breaking to give **L** and **F**. This reaction is similar to the transmetalation studied above, but here

a phosphine ligand stabilized the Cu(I) complex instead of iodine. After that, it was proposed that the substrate **A** is activated through a single electron transfer (SET) redox process by $LCu^{(I)}$-Bpin **L.** In this way, the copper becomes Cu^{II} (**O**) and the fluoroarene acquires radical character and is negatively charged (**M**). Then, another molecule of **L** (not oxidized by the substrate) transmetalates with **M** obtaining the product negatively charged **N** and recovering **K**. Finally, another molecule of substrate **A** take the electron from the product **N** and the desired product **I** is finally obtained together with an activated molecule of substrate **N**.

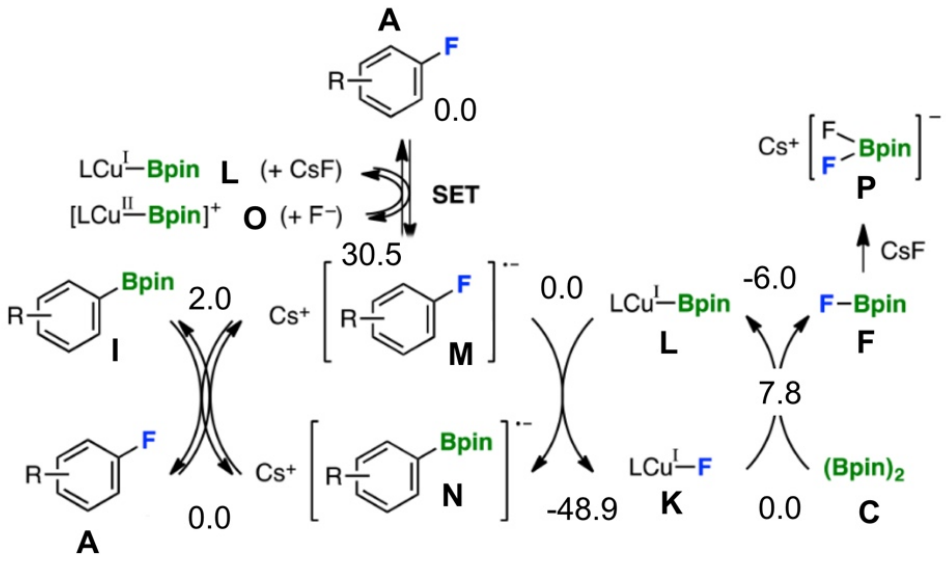

Figure 5-13. Mechanism scheme of Hosoya's hypothesis.

Figure 5-13 shows also the computed relative Gibbs energies for some steps of the proposed mechanism. We took as origin of energies the corresponding reactants of each step. At first glance all the reactions seem favourable. However, when we take a look to the SET process we can observe that its product is 30.5kcal·mol^{-1} less stable than the reactants, that means that the transition state should lie even at higher energy, so, the reaction is far to be reachable. Due to these results we decide to explore an alternative mechanism. We decided to study the transmetalation path without the SET process, a neutral transmetalation. Moreover, we thought

that the adduct **J1** studied above, could be a good starting point for the alternative mechanism given its stability.

Figure 5-14 illustrates the REP of the different possibilities that we have contemplated to explain the C-F boryltation without nickel participation. All the possibilities start in the same way, this is with the reaction between **K** and the adduct **J1**. Thanks to the presence of copper, the B-B bond could be broken very easily, with a TS of 6.5 kcal·mol^{-1}. This reaction gives product **P**, which have boron with tetrahedral shape, and **L** with a stability of -14.9 kcal·mol^{-1}. The barrier for the B-B breaking is lower than in the hypothetical mechanism suggested. Moreover, the products obtained are more stable than **L** and **F** and CsF in Figure 5-13. In yellow line is represented the mechanism proposed by Hosoya explained above, the formation of a less stable products (**O** and **M**) at +24.4 kcal·mol^{-1}. Since the transmetalation with negatively charged fluoroarene is not reachable, we contemplated the possibility of a transmetallation with **A** and **L** as reactants, a neutral transmetalation (blue line in Figure 5-14). However, the barrier of this neutral transmetalation is 40.3 kcal·mol^{-1}, too high to be reachable.

Ribas group in 2013 reviewed the importance of Cu^{III} compounds in homogeneous catalysis.[98] At some point during our research, that paper suggested that Cu^{III} compounds might play some role in this reaction. Firstly, we thought that a sort of Cu^{III} species, such is [Cu(PR3)FArBpin] **R** could form and lead to a kind of transmetallation TS. However, such structure **R** is a TS actually, as the magenta line in Figure 5-14 shows. However, the barrier for this transformation is also far to be reachable, with an energy of 44.1 kcal·mol^{-1}. Finally, we considered that since the products of the first step are a Cu^{I} compound (**Q**) (Figure 5-15) and F-Bpin (**F**) instead of Cu^{I} compound (**L**), the transmetalation path follow this Cu^{I} compound (**Q**). The transmetallation from compound **Q** can take place indeed through a Cu^{I} TS (**S** in Figure 5-14). This new barrier is about 26.8 kcal·mol^{-1}, lower than other values calculated until now. Figure 5-15 depicts de molecular structure of the

complex **Q** and TS **S**, and it is clear that the two are Cu^{I} complexes. This mechanism REP is represented in a purple line in Figure 5-14.

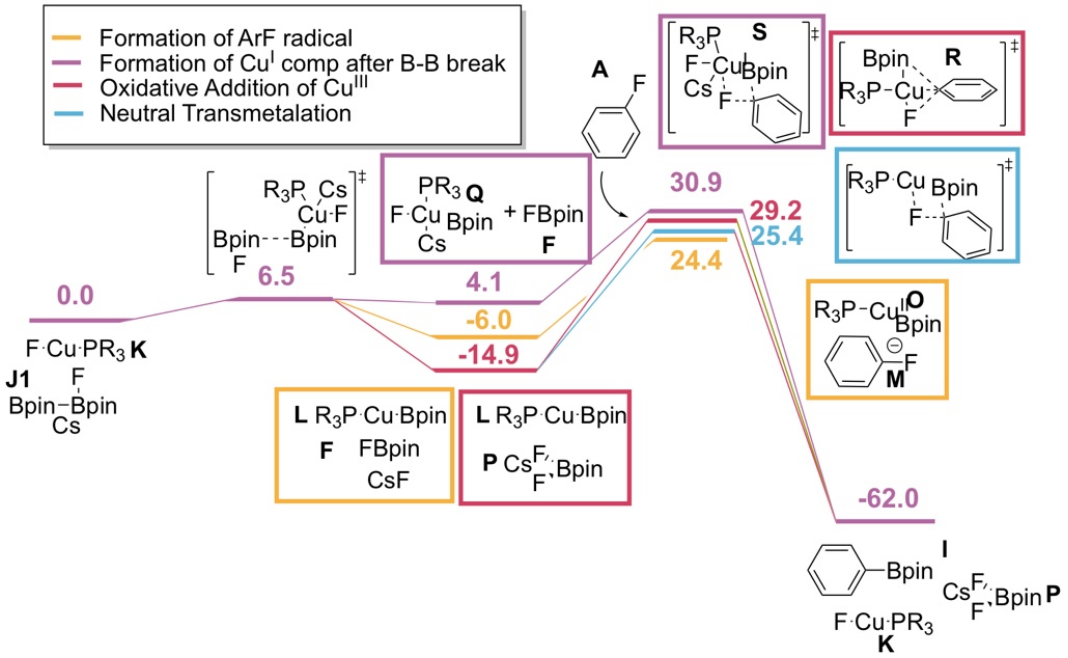

Figure 5-14. REP of the proposed mechanism for a neutral transmetalation.

Hosoya in its 2017 paper demonstrates that the aryl halide borylation works with copper only, so without nickel. However, on the basis of the present study, the mechanism that they proposed would hardly happen because the formation of the aryl halide radical through the formation of Cu^{II} would give products with an energy as high as 30 kcal·mol^{-1}. Note the barrier for such SET process would be even higher. Therefore, the mechanism we found is more favourable through a direct transmetalation with a Cu^{I} species, being ***Q*** the reactant formed in the previous reaction where the copper breaks the B-B bond. After that, **Q** reacts with the subtract **A**, and through the transmetalation TS **S**, the desired product **I** can be obtained. This process is more favourable than the mechanism proposed by Hosoya with a barrier of 26.8 kcal·mol^{-1}. All these results lead us to think that the reaction

reported by Hosoya in 2015 works fine without nickel via the mechanism proposed in Figure 5-14.

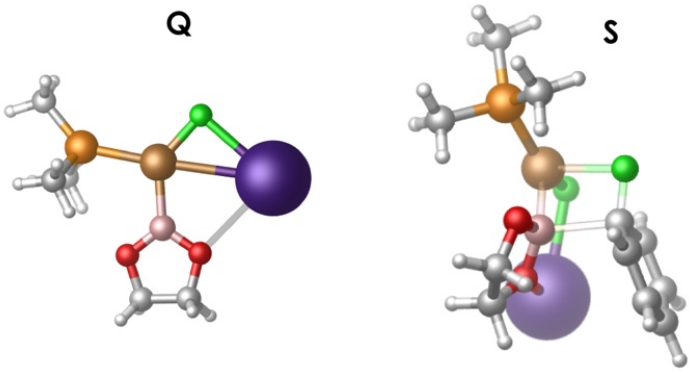

*Figure 5-15. Molecular model of Cu^{I} compound (**Q**) and Cu^{I} TS (**S**), product of the B-B break.*

5.4. CONCLUSIONS

In this chapter, we have carried out a computational study of the Hosoya's reaction,[15] which consist of the borylation of an aryl fluoride with Nickel/Copper catalyst. The computational analysis shows that this reaction happens as a modified cross-coupling mechanism with five steps. The reaction starts as a classical cross-coupling reaction, with the oxidative addition. In this step, the catalyst reacts with the aryl breaking the C-F bond. This step has similarities with the oxidative addition of Martin's reaction[14] (Chapter 3), for this reason, we have compared the two reactions given that the solvent is the only difference in order to see how the solvent could affect. We have not observed evident differences between the use of toluene or THF in the oxidative addition.

The following step that we have studied is the isomerization, where the plane-square product from the Oxidative addition passes from *cis* conformation to *trans*. We made the same comparison than in the previous step. At this point, we have found

a difference between the use of toluene instead of THF. With THF solvent the isomerization step is more favourable for the mono-phosphine compounds, however, under toluene solvent, the isomerization for mono-phosphine and bis-phosphine have the same cost. The next step is the key step in the reaction because it shows the role that plays copper iodine in the reaction. Copper iodide in the presence of CsF forms the salt Cs[CuIF] and this salt reacts with the diborane compound forming the corresponding adduct, which then reacts with copper and breaks the B-B bond, and we obtain the products **E** and **F**. **E** takes us to the next step in the reaction forming a second adduct (**G**) reacting with the product of the isomerization (**AB2**). The intramolecular reaction of this adduct we achieve the transmetalation with the exchange of the fluorine from **AB2** with the boron from **E**, though the TS **TSG** that gives **G1**. We have characterized the intermediates **G** and **G1** and the TS **TSG** because they are new compounds in this chemistry and wanyed to know more about its bond connections. Finally, the last step is the reductive elimination, when the **G1** decompose to give the plane-square compound **H**. At this step we obtain the desired product **I** and we recover the catalyst.

In this chapter, we also evaluated a second Hosoya's reaction reported in 2017, where they could make the reaction work without any nickel catalyst, only copper. As an explanation of this, they proposed a mechanism involving a SET. We proved this computationally and found that this mechanism is not possible. Instead, we found that the reaction begins as Hosoya's hypothesis, however the products after de B-B break is a Cu^{I} compound, which may react with the aryl halide obtaining the desired product.

"Science and everyday life cannot and should not be separated. Science, for me, gives a partial explanation of life." Rosalind Franklin

CHAPTER 6

6. *Ni-Catalysed Borylation into Benzofuran C2-O Bond*

6.1. Introduction

Yorimitsu and coworkers[18] presented a boron insertion reaction into the C-O bond of benzofuran (Figure 6-1) and obtained a boroncycle, which is of interest for the pharmaceutical industry

because it can be used as a synthetic intermediate. Borocycles are very similar to molecules that can be used as antifungals or antibacterials.[99] This reaction (Figure 6-1) differs from Martin's and Mori's reactions in the fact that the O atom does not act as a leaving group. The boron unit is inserted into the C-O bond, so the oxygen atom is present in the product. Figure 6-1 shows a scheme of the Yorimitsu reaction, where it can be seen that the reaction is catalysed in the presence of Cs_2CO_3 by a Ni(0) complex bearing a NHC ligand. We are interested in the study of this reaction because the classical transmetalation mechanism does not explain how the reaction occurs, since the oxygen atom is not acting as a leaving group. Additionally, in the classical cross-coupling reaction the salt Cs_2CO_3 does not participate. Then, neither the role of the base/salt in the reaction, nor the sequence of the reaction steps is clear.

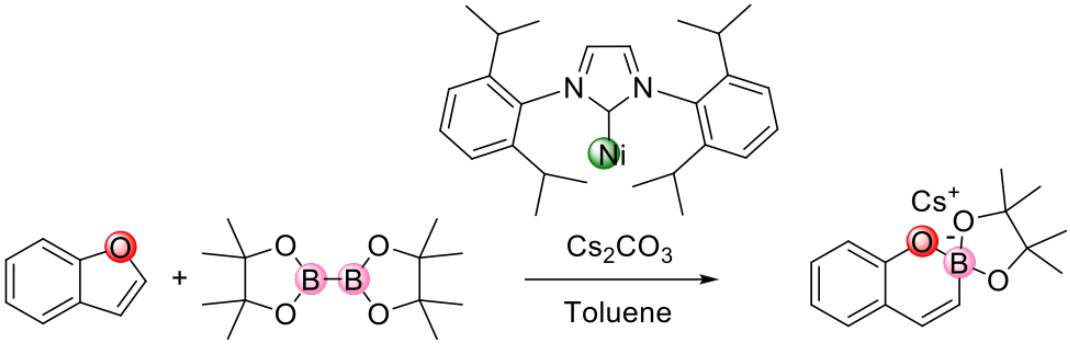

Figure 6-1. Yorimitsu's reaction scheme.

6.2. Computational Details

All the calculations in this chapter were carried out using the Gaussian 09[66] software package. Several Density Functional Theory (DFT) based methods were used. The hybrid functional B3LYP[43,44,69] with Grimme's empirical dispersion corrections D3[70] (B3LYP-D3) was used as primary method. Also, we considered M06-2X[68] and ωB97XD[45] functionals for the sake of comparison

with B3LYP-D3. All the structure optimisations, frequencies and energies were calculated using the 6-311G** basis set[67] for atoms C,H,B,O,F and N; we used the LANL2DZ basis set[67] for Ni and Cs atoms which includes the corresponding effective core potentials. Solvent effects were included explicitly using the SMD[47] standard parameters for THF. Thermal corrections at 298K were included in the standard manner. IRC calculations were realized for each TS structure. A data set collection of computational results is available in the ioChem-BD repository[81] and can be accessed via https:// doi.org/10.19061/iochem-bd-1-56.

6.3. Results and Discussion

The goal of this study is to shed light on the mechanism of the boron insertion reaction into the C-O bond of benzofuran. A first glance at the reaction suggests that it follows a classical cross-coupling mechanism.[37] This mechanism consists in three main steps: oxidative addition, transmetalation and reductive elimination and has four participants: the catalyst, the base, and two reactants. General understanding suggests that the catalyst reacts with one substrate via oxidative addition first. Then two reactants exchange fragments, like in the transmetalation step. Finally, the fragments get coupled in the reductive elimination and the product separates from the catalyst.

However, when we look carefully at the Yorimitsu reaction we find first an additional participant that we do not observe in the classical cross-coupling mechanism, the Cs_2CO_3 salt, and second there is actually any leaving group in the reactant. These facts lead us to suspect that the reaction mechanism could be more sophisticated than the classical cross-coupling reaction pathway. The new mechanism that we suggest here consists of the following steps: i) substrate pre-coordination, ii) oxidative addition, iii) boryl transfer, iv) reductive insertion, v) ring-contraction nucleophilic attack and vi) product release.

6.3.1. SUBSTRATE PRE-COORDINATION

The catalytic cycle starts with the C-O bond oxidative addition reaction. But prior to this, the substrate coordinates to the catalyst. This pre-coordination can take place because of the favourable interaction between the metal catalyst and the π system of the five-member ring of the substrate, actually the C2-C3 double bond. We studied this interaction in some cases, considering a model ligand (1,3-di(isopropyl)-2,3-dihydro-1H-imidazole-2-ylidene) and the real one (1,3-bis(2,6-diisopropylphenyl)-imidazol-2-ylidene), as well as two substrates, namely benzofuran and benzopyrrole (indole). Moreover, as catalyst, both [Ni(NHC)PR_3] as well as [Ni(NHC)] Ni(0) complexes were considered. The reason behind studying such complexes relies in the fact that we observed, during the oxidative addition, phosphine ligand decoordination when the real carbene ligand was used.

Figure 6-2 shows the optimised molecular structures of these adducts; **A** corresponds to the combination of [Ni(NHC)] and benzofuran; **A'** is the adduct between [Ni(NHC)PR_3] and benzofuran; **B** is the adduct formed by the real carbene Ni complex and benzofuran; and **C** is the adduct of the real carbene Ni complex and benzopyrrole; **D** is the adduct between [Ni(NHC)] and indole; **D'** is the adduct [Ni(NHC)PR_3] and indole.

In all adducts **A**, **A'**, **B**, **C**, **D** and **D'** in Figure 6-2 the interaction between the metal atom and the substrate takes place through the C-C double bond of the five-member ring. Analysis of the fragment molecular orbitals (FMO) concluded that the Ni(0)/substrate bonding is built up through classical π back-bonding mechanism, i.e. by mixing a filled d metal orbital with the empty π antibonding in the substrate. It is worth mentioning that several other coordination modes were found. For example, the heteroatom O or N can directly interact with the metal in different ways. Although such species were characterised as true minima in the potential

energy surface, they were found to be less stable than those in Figure 6-2.

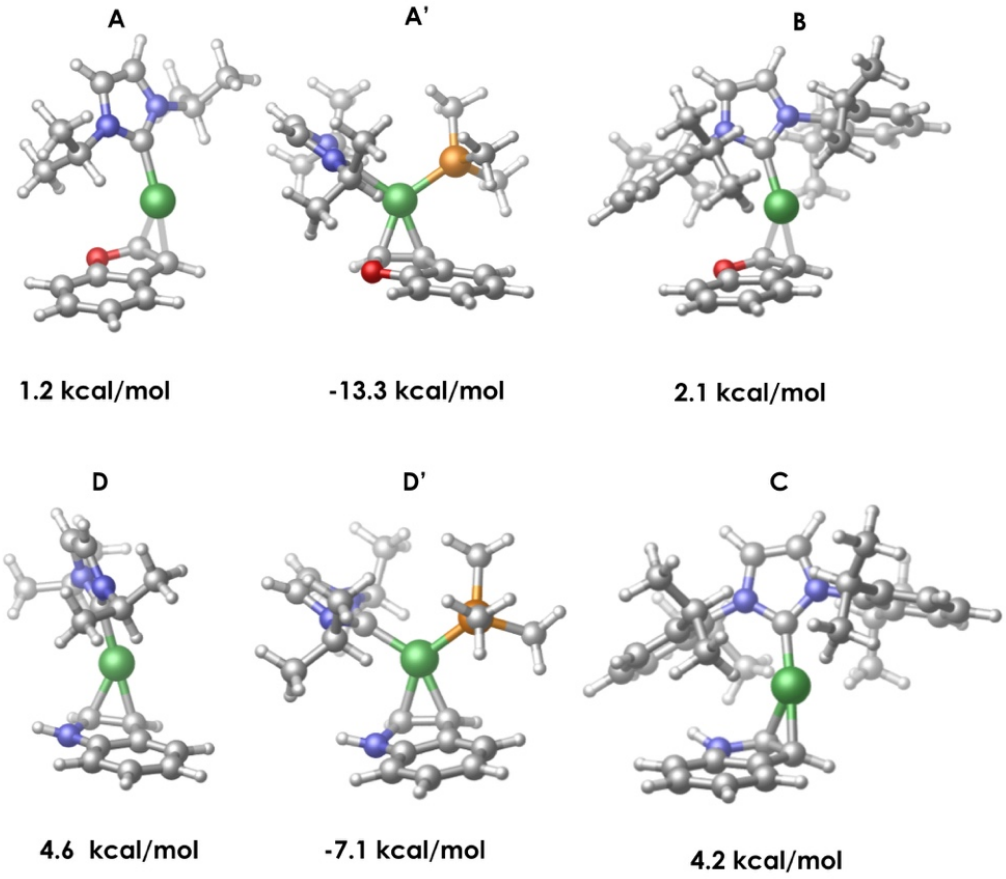

*Figure 6-2. Molecular models and interaction Gibbs energies with respect to [Ni(NHC)PR$_3$]. **A** is [Ni(NHC)] and benzofuran. **A'** [Ni(NHC)PR$_3$] and benzofuran. **B** is the adduct formed by [Ni(NHC$_{real}$)] and benzofuran. **C** is the adduct formed by [Ni(NHC$_{real}$)] and indole. **D** is the adduct formed by [Ni(NHC)] and indole. **D'** is the adduct formed by [Ni(NHC)PR$_3$] and indole.*

Figure 6-2 depicts the relative Gibbs energies for the adducts with respect to [Ni(NHC)PR$_3$] plus the substrate. The stabilisation for forming these bis-ligand catalyst adducts is large, more than 7 kcal·mol^{-1} in both cases, and it slightly depends on the nature of the reactant, less stable for indole. However, the mono-ligand adducts seem not stable because the origin of energies now includes Ni(NHC)-PR$_3$ bond. Actually the value for **A**, taking the zero with respect Ni(NHC) plus substrate, is as large as -25.8, -29.8 for **B** and -27.7 kcal·mol^{-1} for **C**, which are practically as large

as the interaction energy between Ni(NHC) and the phosphine. It is worth to note that, for real carbene catalyst, we could not find the bis-ligand adducts because the phosphine decoordinates since steric crashings.

Stabilising interactions between the ligand and the substrate in the adducts were analysed in terms of noncovalent interactions (NCI) theory as introduced by Yang and collaborators.[49] In Figure 6-3 several stabilising interactions between the ligand and the substrate, and within the ligand itself, are clearly visible as coloured isosurfaces. Areas in green/yellow indicate attractive interactions, while areas in orange/red indicate strong non-bonded overlap. C-H/C-H interactions within the ligand appear as localised spots in green. There is a large overlap area between the substrate and the catalyst, shown as an orange area in Figure 6-3 A, and indicating C-H/O interaction. This is because the hydrogen atoms of the isopropyl moieties in the ligand lie close to the aromatic ring in the substrate, thus creating a favourable C-H-π interaction. The increased interaction from **A** to **B** is made evident in Figure 6-3. Besides, the large red area indicates strong interaction of the oxygen atom in benzofuran with the ligand. In the case of benzopyrrole, **C** in Figure 6-3, the interaction is only slightly weaker, -27.7 kcal·mol^{-1}.

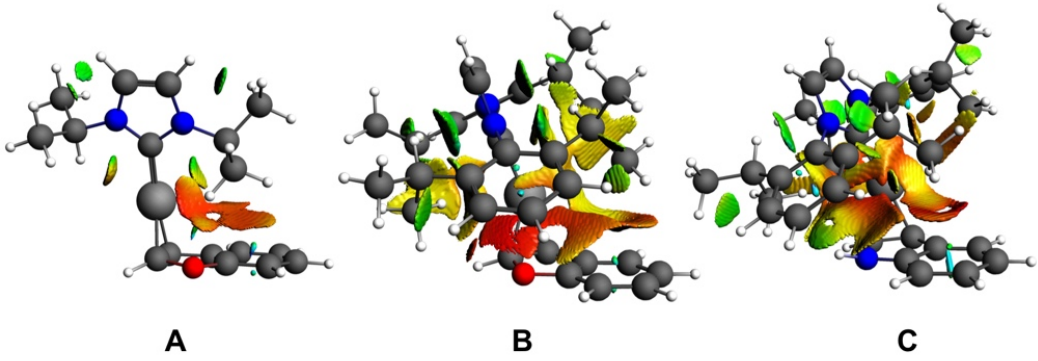

Figure 6-3. Noncovalent Interactions (NCI). Reduced density gradient isosurfaces (s=0.5) coloured according to the value of the second eigenvalue of the Hessian of the electron density for B and C adducts. The colour scale indicates lamda2 values from -0.05 (red) to 0.2 (blue).

Since all adducts that we studied presented very high stabilisation energies, we also wondered whether some sort of overstabilisation could be caused by the basis set superposition error (BSSE). The BSSE were computed following the counterpoise method for species A and B in Figure 6-2. For both A and B adducts, the BSSEs are 6.1 and 6.2 kcal·mol^{-1}, respectively. It is worth pointing out that the BSSE correction is significant, and it affects both systems almost equally.

6.3.2. C-O Oxidative Addition

The next step in the mechanism is the oxidative addition reaction. As we mentioned before, the oxidative addition consists in the insertion of the Ni(0) catalyst into the C-O bond of the substrate benzofuran. The metal atom is formally oxidised to Ni(II) in the process. As in the previous section, we considered two ligands: a model of the experimental ligand and the real ligand used in the experiments by Yorimitsu and co-workers. Besides, we likewise considered two substrates, namely benzofuran and indole. Note that the oxidative addition reaction could yield two possible products: one having the oxygen atom of the substrate *trans* to the ligand, and the other one having the carbon atom of the substrate *trans* to the ligand, which is 15 kcal.mol^{-1} less stable than the former. Therefore, we evaluated the reaction path towards the most stable product.

All the transition state structures (TSs) for the oxidative addition reaction were successfully characterised. **TS1A** corresponds to the transition state of the reaction between the mono-model ligand catalyst and benzofuran; **TS1A'** corresponds to the transition state of the reaction between the bis-model ligand catalyst and benzofuran; **TS1B** is the TS of the oxidative addition of the real ligand catalyst and benzofuran; and **TS1C** corresponds to the TS of real ligand catalyst and indole; **TS1D** corresponds to the transition state of the reaction between the mono-model ligand catalyst and indole; **TS1D'** corresponds to the transition state of

the reaction between the bis-model ligand catalyst and benzofuran.

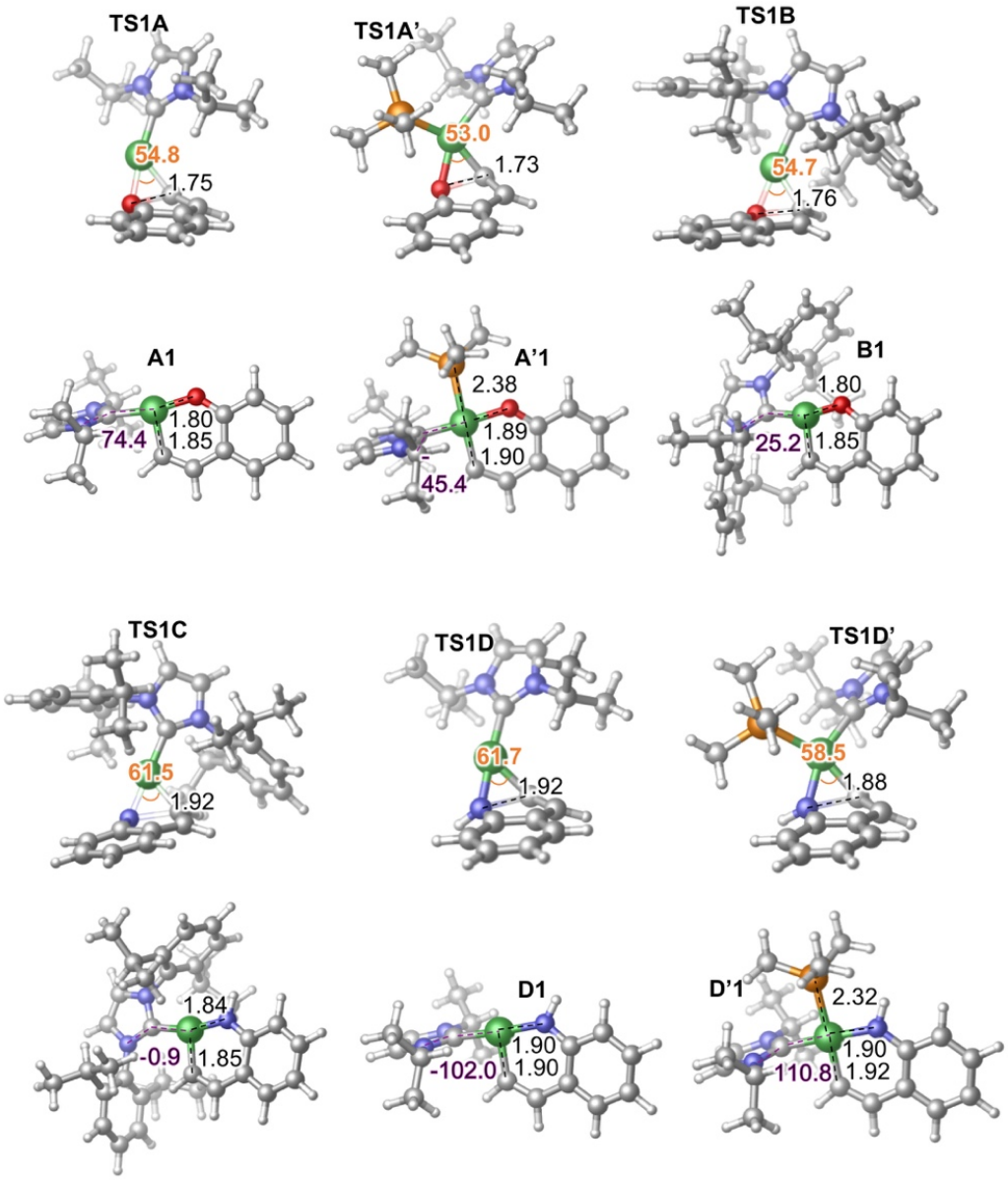

*Figure 6-4. Geometries of TSs and products for the oxidative addition step. **A** is [Ni(NHC)] and benzofuran. **A'** [Ni(NHC)PR$_3$] and benzofuran. **B** is the adduct formed by [Ni(NHC$_{real}$)] and benzofuran. **C** is the adduct formed by [Ni(NHC$_{real}$)] and indole. **D** is the adduct formed by [Ni(NHC)] and indole. **D'** is the adduct formed by [Ni(NHC)PR$_3$] and indole. Bond angles in orange, dihedral angles in purple and bond distances in black, and in Å.*

Some geometrical parameters are collected in Figure 6-4. For each structure in Figure 6-4, the C-Ni-O angle and the length of the C-O breaking-bond are indicated in each case. In this section we only centred in **TS1A**, **TS1B** and **TS1C** because the corresponding structures to **TS1A'** and **TS1D'** with the real ligand would not form because steric reasons.

The geometries of the three transition states look very similar. All four structures form a three-centre C-Ni-X ring (X=O for **TS1A**, **TS1B**, and X=N for **TS1C**). The C-Ni-X angle of this triangle shows few changes when compared to the four geometries and the C-Ni-O angles in **TS1A** and **TS1B** are almost the same. **TS1C** shows some wider angles, so the kind of the substrate affects the geometry of the oxidative addition TS. The C-O bond distances for **TS1A**, **TS1B**, and the C-N bond distance for **TS1C** are represented in Figure 6-4, in which we clearly see that the C-O and C-N distances increase as the angle C-Ni-X increases.

We also characterised the products of the oxidative addition reaction. Figure 6-4 shows the geometry of these products. **A1** represents the product obtained from the model ligand catalyst and benzofuran oxidative addition; **B1** is the product of the reaction of real ligand catalyst and the benzofuran; and **C1** corresponds to the product of the oxidative addition of real ligand catalyst and indole. These products are the result of the insertion of the Ni atom into the C-X bond (X=Oxygen for A and B; X=Nitrogen for C). Therefore, the 5-membered ring of benzofuran and indole evolves to a six-membered ring, where the new member is the nickel atom.

The Ni-C and Ni-O/Ni-N bond distances of the products are represented in Figure 6-4. The Ni-C bond distance has roughly the same value for products **A1**, **B1** and **C1**. Regarding the Ni-O bond distance, products **A1** and **B1** products have the same bond distance.

We have likewise described the N-C-Ni-C dihedral angle of products **A1**, **B1** and **C1**. These dihedral angles allow us to

visualise the relative position of the catalyst with respect to the substrate. This angle measures the angle between the N-heterocyclic carbene ring and the metallacycle just formed. The dihedral angle of **A1** is 74.4°, which indicates that the ligand in the catalyst adopts an almost perpendicular orientation with respect to the substrate. The dihedral angle is smaller for the **B1** products, which indicates that the catalyst tends to be on the same plane as the substrate. For this **B1** substrate, the interaction between the heterocyclic oxygen atom and the π system of a phenyl in the ligand catalyst favours the structure. Finally, this dihedral angle is practically zero for the **C1** product, which means that the carbene moiety in the catalyst is almost on the same plane than the substrate. Here, the H/π interaction between the N-H bond and C-H bonds from the benzofuran and the π systems of the phenyls of the catalyst gives **C1** its characteristic structure, Figure 6-4.

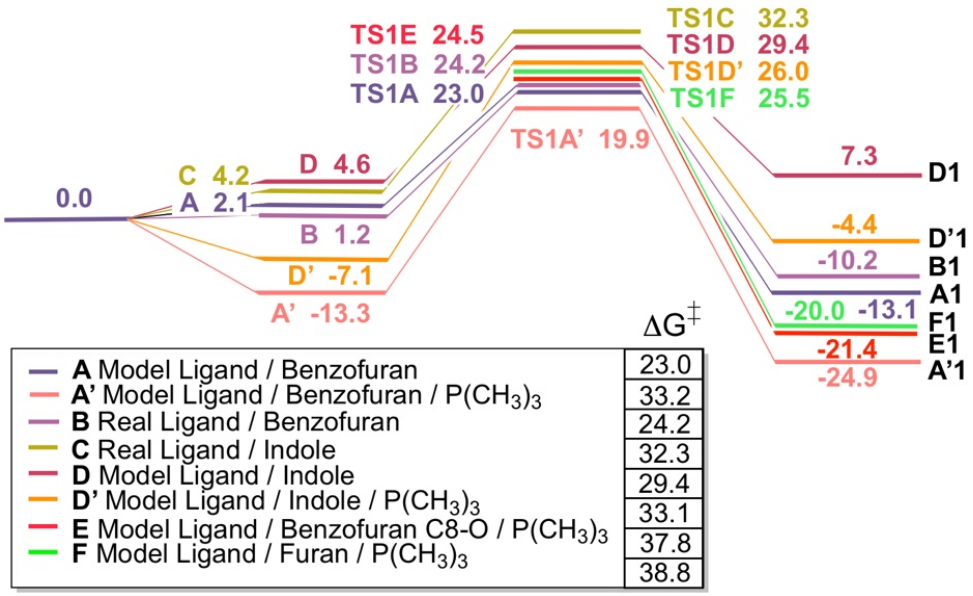

Figure 6-5. Relative Gibbs energies of Previous Coordination and Oxidative addition for different ligand catalysts and different substrates. Dark purple: model ligand catalyst and benzofuran; light purple: real ligand catalyst and benzofuran; green olive: real ligand catalyst and indole. All values are in kcal·mol^{-1}.

With these characterised TSs and products energies, we constructed the reaction energy profile (REP) in Figure 6-5, which shows that the activation barriers for the oxidative addition, taking as zero the catalyst [Ni(NHC)PR_3] plus the substrate, are 23.0 kcal·mol^{-1} for **A**, 24.2 for **B** and 32.3 for **C**. The products of this oxidative addition reaction are very stable. The oxidative addition of benzofuran, both in the model and in the real catalyst, gives products with an energy of about 10 kcal·mol^{-1} below the reactants (light and dark purple lines in Figure 6-5) and are much more stable than the corresponding adducts. However, it is worth stressing that the product for indole oxidative addition is less stable than its corresponding adduct (green olive line in Figure 6-5). Regarding the adducts [Ni(NHC)PR_3] (**A'** and **D'**), we can observe in Figure 6-5 that the oxidative addition barrier for this species is higher than that for the adducts with [Ni(NHC)], with barriers of 33.2 kcal·mol^{-1} for **A'** and 33.1kcal·mol^{-1} for **D'**, respectively. Although the free energy of **TS1A'** is the lowest of all the TSs found (19.9 kcal·mol^{-1}), the barrier from the corresponding adducts is the highest. These results suggest that the oxidative addition is easier if it takes place from adducts [Ni(NHC)] rather than from adducts [Ni(NHC)PR_3].

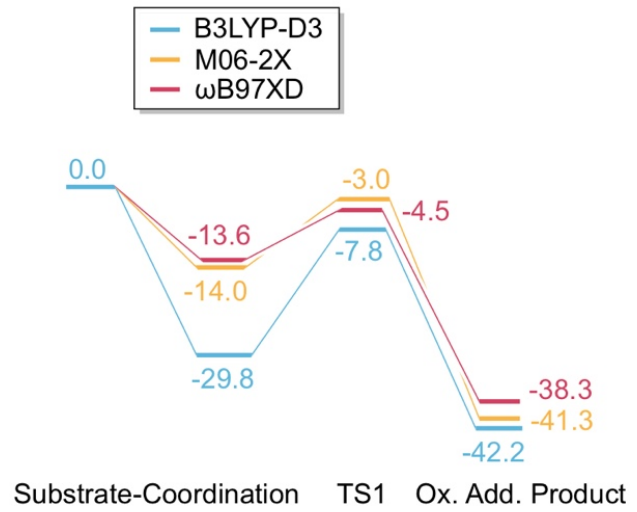

Figure 6-6. Gibbs energy reaction energy profile of the oxidative addition of benzofuran to the model ligand Ni(0) complex with different DFT methods: B3LYP-D3 in blue, M06-2X in yellow and ωB97XD in magenta. All values are in kcal·mol^{-1}.

At this point, we wanted to check the accuracy of some DFT functionals when describing the geometries and energies of these systems. We chose a meta-hybrid functional such as M06-2X and the range-separated ωB97XD. In Figure 6-6 we collect the results at the M06-2X and ωB97XD[80] levels, together with the results obtained at the B3LYP-D3 level for the model ligand and benzofuran system. Whereas the M06-2X and ωB97XD methods almost match the value, B3LYP-D3 over stabilises the adduct. This is due to the different treatment of the empirical dispersion corrections in the Grimme's D3 method, which seems that exaggerates the strength of the non-bonding stabilising interactions, thus giving lower energies for the pre-adduct. However, for the TS and the product of the oxidative addition, the three DFT methods provide a fully equivalent response. For this reason, we decided to continue using the B3LYP-D3 DFT method to study the subsequent steps. Also, the tinny differences between the model ligand and the real one justified choosing the smallest system to study the next steps.

6.3.3. Boryl Transfer

In the classical cross-coupling reaction mechanism, the transmetalation normally occurs after the oxidative addition step. However, in the present case, such transformation was not possible because there is no actual leaving group in the substrate. The two components of the C-O bond, which is broken during the oxidative addition, will be present in the product, therefore they do not need to be removed from the coordination sphere. We thus considered the possibility that the boryl moiety, assisted by Cs_2CO_3, could be directly added to the nickel(II) complex.

As mentioned in the above, the need for Cs_2CO_3, CsF or other bases as crucial additives in the reaction (Figure 6-1) suggests that this salt could somehow participate in the reaction mechanism and could even play a key role in the reaction, probably modifying the classical cross-coupling reaction mechanism.

In previous studies by our group, we found that Lewis bases can activate the B-B bond in diboranes by forming a Lewis base-diboron adduct.[74] This adduct is best described as a B(sp^2)-B(sp^3) species the B-B bond of which is longer than in the isolated diboron species. The boron directly linked to the Lewis base atom becomes positively charged while the second boron atom becomes negatively charged, thus acquiring boryl character. This activation enables the direct transfer of the boryl unit to unsaturated substrates in a metal-free manner.[74]

Moreover, Marder and coworkers have made the X-ray characterisation of such sort of adducts possible only very recently.[78] They characterised the adduct formation by the reaction of $B_2(pin)_2$ and the KO^tBu salt. Marder and his team found that $K[B_2pin_2O^tBu]$ forms a solid of infinite chains in parallel. Moreover, they found out that the potassium atoms interact with all the five oxygens in the $[B_2pin_2O^tBu]^-$ adduct in the solid state. The X-ray geometry for the $[B_2pin_2O^tBu]^-$ adduct anion shows that the B(sp^3) atom is tetrahedral, whereas the B(sp^2) keeps its planar coordination geometry. It is worth noting that these geometrical features fit perfectly with the DFT structures computed previously by our group.[74] Marder studied likewise the adduct formed by the interaction between $B_2(pin)_2$ and Me_4NF. The anion of this fluoride adduct ($[B_2(pin)_2F]^-$) presents similar geometrical features to the alkoxy adduct ($[B_2(pin)_2OtBu]^-$) indeed.

All this suggests that caesium carbonate, Cs_2CO_3, could somehow participate in the reaction probably by activating the diborane and forming an adduct similar to those just mentioned. Actually, we could characterise such adduct, which is shown in Figure 6-7 together with the diboron compound and some geometrical parameters.

In the isolated diboron compound, the B-B bond distance is 1.70 Å, whereas this distance becomes larger (1.74 Å) after the adduct is formed. The two boron atoms have a pseudo-tetrahedral shape because each boron atom is bonded to an oxygen of the

carbonate. The dihedral angle O-B-B-O becomes bigger after the adduct formation. Whereas, this dihedral is -39.0º for $B_2(pin)_2$, it decreases to -0.2º in the adduct. Likewise, Marder reported some alkoxy adducts,[78] the geometry of the adduct in Figure 7 shows caesium atoms coordinated to four oxygens, one on each side of the adduct.

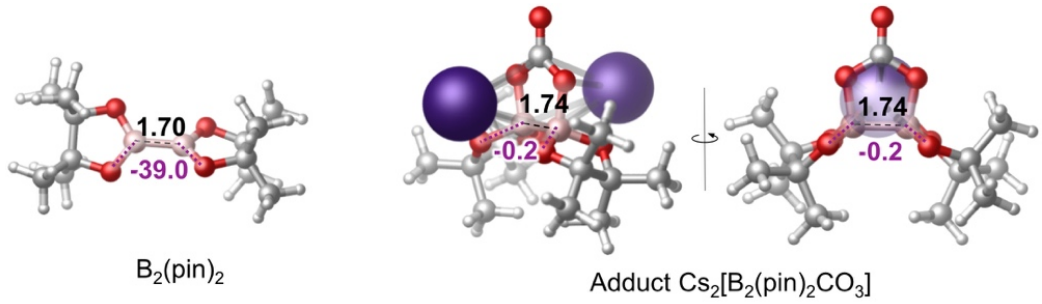

Figure 6-7. Diboron ($B_2(pin)_2$) and two views of the $Cs_2[B_2(pin)_2CO_3]$ adduct. B-B bond distances are in Å and in black. O-B-B-O dihedral angles are in degrees and in purple.

The Gibbs energy for the formation of the adduct, just computed without any additional entropic correction, is rather large, as much as -44.7 kcal·mol^{-1}. Although the negative value indicates that the adduct is much more stable than the salt and the diboron, the value is too large so we suspect that it is overestimated.[100] Note that the formation of this kind of adduct could help overcoming the low solubility of the caesium carbonate or CsF base. We will consider the diboron/base adduct as an initial reactant.

Then, the diboron/base reacts with the oxidative addition product just described. A boryl moiety from the diboron-carbonate adduct is transferred to the nickel atom (Figure 6-8). We have characterised the transition state and the products obtained when we considered both caesium cations in the molecular structures explicitly. It is worth mentioning that the two cations present in the adduct provide additional stability to the transition state for

this boryl group transfer, which could not be characterised otherwise. Moreover, when Mori et al.[11] studied the nickel-catalysed cross-coupling of methoxyarenes with arylboronic esters via C–O bond cleavage, both Cs^+ and F^- ions were included explicitly.

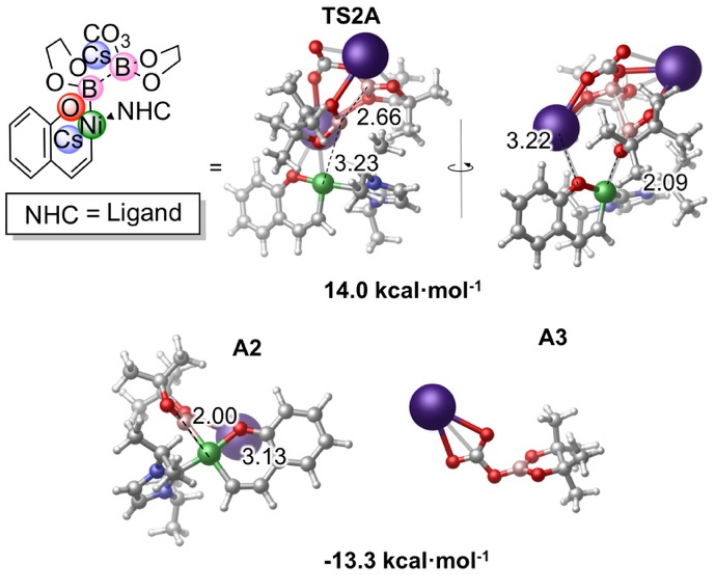

Figure 6-8. Scheme and two views of the TS molecular model of the boryl transfer path, its relative Gibbs energy. Bond distances shown in black and in Å.

The transition state for this boryl transfer consists in the breaking of the B-B bond and the formation of the new Ni-B bond. Two views of the molecular model of this transition state are represented in Figure 6-8. This model shows that one of the caesium cations is bonded to the oxygen of the product **A1** with a bond distance of 3.22Å. Besides, one oxygen atom of the boryl moiety presents bonding interaction with the nickel atom at 2.09Å. That gives stability to this transition state. The B-B distance in this TS is 2.66Å.

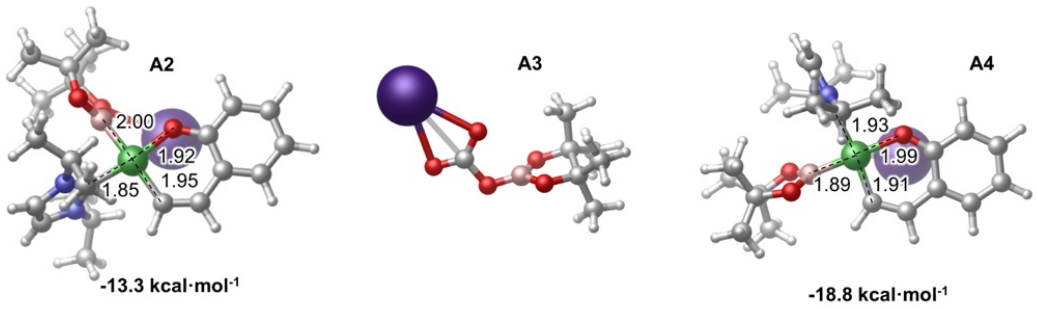

*Figure 6-9. Selected geometrical parameters (in Å) and Gibbs energy of the two isomers of the transmetalation product **A2** and **A4**, a subproduct **A3**.*

Figure 6-9 shows the molecular models of the two products that this reaction step produces. In the principal product **A2** in Figure 6-9, the boron is bonded to the nickel atom at 2.00Å bond distance. The caesium keeps interacting with the oxygen atom of benzofuran, as in the transition state **TS2A** with a bond distance similar to **TS2A**, and with the oxygen atom of the substrate. The subproduct formed during this step is the caesium boron-carbonate **A3** (Figure 6-9), in which the non-transferred boron unit is best described as a boronium unit, which plays the role of the second counter-ion neutralising the carbonate –2 charge.

Without taking into account any further correction the activation energy of this step is 27.1 kcal·mol^{-1}, which indicates that the transmetalation/boryl transfer step is rate determining. The products of this step are as stable as the sum of reactants **A1** and the carbonate/base adduct with an energy of -13.3kcal·mol^{-1}.

6.3.4. Reductive Insertion

After the boryl transfer step, the next transformation towards the desired product is the migration or insertion of the boron unit, which can take place either into the Ni-O bond or into the Ni-C bond. We will discuss below why this step is named reductive insertion. Firstly, note that the geometry of **A2** in Figure 6-9 , in which the boron and oxygen moieties lie in *cis* disposition, has the

right conformation for the boron insertion into the Ni-O bond to take place. According to such disposition, the boron cannot migrate into the Ni-C bond since B and C atoms lie in *trans* disposition. However, **A2** could experience an isomerisation process, so by exchanging the positions of the boryl and the carbene ligand, for instance, the B and C atoms would adopt the *cis* disposition thus enabling the boron migration into the Ni-C bond. As well as **A2** we characterised its isomer **A4** and are both shown in Figure 6-9.

The Ni-B distance in **A2** (2.00Å) the isomer obtained after the boryl transfer, is longer than that in its isomer **A4** (1.89Å). The opposite occurs for the Ni-O bond distance. The strong sigma-donor character of the boryl ligand[101] lengthens the metal-ligand bond distance of the ligand *trans* to the boryl. The Ni-C bond distance in **A2** (1.95Å), where the boryl ligand is in *trans*, is larger than the Ni-C bond in **A4** (1.91Å), where the carbene ligand is in *trans* position. The same happens with Ni-O bond distances, which are shorter in **A2** (1.92Å) than in **A4** (1.99Å), because in **A2** the Ni-O bond has the carbene ligand in *trans*, whereas in **A4** the boryl is in *trans* position with respect to the O-Ni bond.

Another difference between the two isomers is the coordination of the Cs^+ counterion. Whereas in **A2** the counter-ion interacts with the oxygen atom of benzofuran and an oxygen of the boron ester, in **A4** the caesium interacts with the π-system of the benzofuran double bond and its oxygen.

The relative Gibbs energy of the two isomers indicates that **A4** is slightly more stable by 5 kcal·mol^{-1}. This larger stability is not caused by different interactions with the caesium ion. In an earlier stage of this study, by considering a simpler model for the boron unit and without including in the model the caesium cation, the equivalent isomer **A4** was found to be 7 kcal·mol^{-1} more stable than the corresponding **A2**. Also, using such simpler model, a pseudo-tetrahedral structure was revealed as the transition state connecting both isomers. The barrier for this isomerisation is 23

kcal·mol^{-1}. However, taking into account the real ligand and boron species, we could not locate such transition state for the **A2**-**A4** isomerisation process. Note that **A4** could be formed in the case that the oxidative addition step had not produced **A1** but its isomer, in which the C atom of the substrate would lie trans to the ligand. As we mentioned above, such alternative oxidative addition product is 15 kcal.mol^{-1} less stable than **A1**.

In this step the boron unit migrates into the Ni-O bond starting from **A2**, whereas the isomer **A4** drives the migration towards Ni-C bond. Although the pathway through **A4** seems not reachable, the two possible transition states and the corresponding products of this step were fully characterised and are shown in Figure 10. Both two TSs present a triangular arrangement of the three atoms involved, namely Ni, B and O or C. In **TS3A2**, the triangular structure defines the formation of the new B-O bond, whereas **TS3A4** promotes the B-C bond formation.

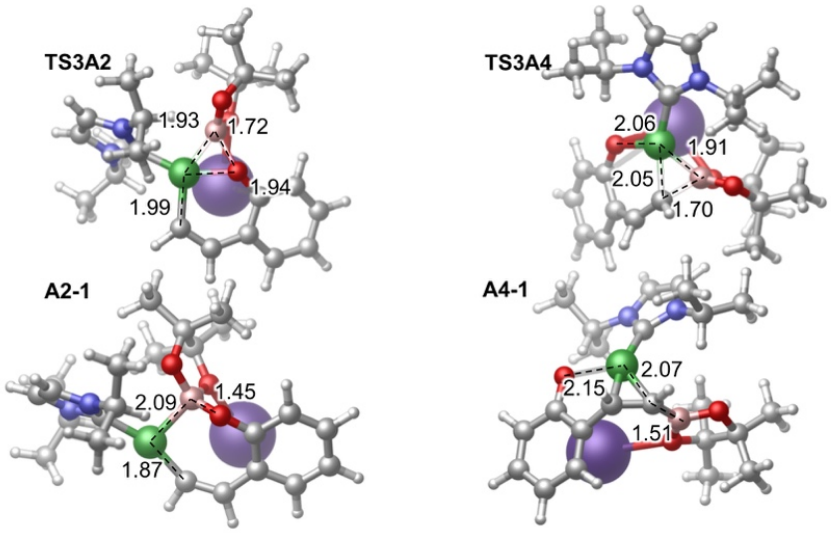

Figure 6-10. Molecular models for the B-O (left) and B-C (right) bond formation TSs and products, and selected interatomic distances in Å.

Figure 6-10 shows the two TSs and the two products and some relevant bond distances. **A2-1** is the product obtained after the B-

O reaction through **TS3A2**, whereas **A4-1** is the product of the B-C bond formation by the way of **TS3A4**. There are big differences regarding the geometry of these two products. **A2-1** forms a 7-member ring, which brings the B and C atoms in close distance, and ready to follow up the next and final step, the B-C bond formation. Note also that the caesium atom keeps interacting with both oxygen atoms of the substrate and the borane unit. However, in **A4-1** the ring is open and the expected Ni-B bond could not be formed. The geometry of this intermediate shows the borane unit in a coplanar arrangement with the C-C double bond, which in fact is acting as the ligand to nickel. The caesium cation keeps still interacting with the two oxygens (O in the substrate and one O atom in the borane unit), but displaces the O and B atoms very far away in such a way that it prevents the reaction to continue.

Table 8. NPA (Natural Population Analysis) and MPA (Mulliken Population Analysis) atomic charges for Ni, B, O and C atoms, and NCE (Natural Electron Configuration) for Ni in some intermediates.

		Reactants	A1	A2	A2-1	Products
		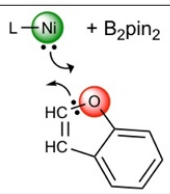	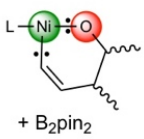	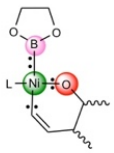	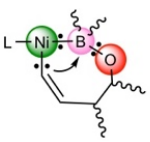	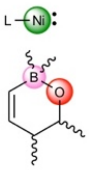
Ni	NPA	-0.213	0.402	0.505	0.148	-0.213
	MPA	-0.313	0.285	-0.007	-0.106	-0.313
B	NPA	0.778	0.778	0.705	1.100	1.054
	MPA	0.335	0.335	0.321	0.643	0.568
O	NPA	-0.470	-0.684	-0.791	-0.760	-0.717
	MPA	-0.280	-0.575	-0.549	-0.386	-0.400
C	NPA	0.153	-0.343	-0.596	-0.552	-0.444
	MPA	0.059	-0.293	-0.432	-0.395	-0.315
Ni	NEC	4s 0.9 3d 9.28 4p 0.03	4s 0.41 3d 8.92 4p 0.27	4s 0.42 3d 9.06 4p 0.01	4s 0.6 3d 9.24 4p 0.01	4s 0.9 3d 9.28 4p 0.03

The free energies of these intermediates and TSs reveal that the boron insertion into the cycle could proceed with low barriers, 13.8

kcal·mol^{-1} to form the B-O bond (**TS3A2**) and 9.6 kcal·mol^{-1} to form the B-C bond (**TS3A4**). Although the reaction path through the **A4** isomer has a lower barrier and the product **A4-1** is also quite stable (-27.1 kcal·mol^{-1}), this reaction path does not drive the reaction any further.

As we mentioned above, we refer to this reaction step as reductive insertion upon the analysis of the evolution of the electron distribution. Table 8 collects the NPA and MPA atomic charges for the main Ni, B, C and O atoms. The oxidative addition step (Reactants to **A1**) brings electron density from the Ni(0) atom to both the C and O atoms of the substrate. NBO analysis (see Supporting Information) indicates that the nickel atom in **A1** lost one lone pair, that the oxygen holds three lone pairs, and that the Ni-C bond is occupied by1.89e and slightly polarized towards the C atom (40%Ni/60%C). In the boryl transfer step (**A1** to **A2**), a new Ni-B bond is formed with 1.77e in the NBO bonding orbital and 0.44 in the anti-bonding, slightly polarized towards B (40%Ni / 60%B). This addition strongly affects the Ni-C bond trans to the new Ni-B bond, being the C atom the one that increases its negative charge the most. The Ni-C NBO bond is actually broken and its place we found a lone pair on C 1.56e. The negative charge on the boryl fragment is thus strongly delocalized through the Ni to the C atom. It is precisely during the present step (**A2** to **A2-1**) when the boryl unit loses out an important amount of electron density, by evolving to a boronium species which is tetrahedrically bonded to three O atoms and to nickel. Electron density is transferred to Ni, and the Ni-B bond (1.79e bonding, 0.22 antibonding 69%Ni / 31% C) has opposite polarization than in **A2**. Importantly, the Ni-C bond is now more polarized towards the C atom, with an important anti-bonding population, which triggers the next transformation. Although the number of NBO lone pairs on the Ni atom is still 4, the electron density on the Ni has clearly increased, therefore we named this step reductive insertion. Note in Table 1 the natural electron configuration (NEC) of the Ni atom, which suggests the reduction of Ni(II) to N(0) in two steps.

6.3.5. RING-CONTRACTING NUCLEOPHILIC ATTACK

Once the reductive insertion of the boron unit is completed, the last step in a classical mechanism would be the reductive elimination to form the C-B bond. Instead we refer to this transformation as a ring-contracting nucleophilic attack of the C atom over the B center. Taking into account that the nickel atom is already partly reduced, that the B atom is positively charged and the C atom is negatively charged, we consider that this transformation is better understood as a nucleophilic attack of the C atom over the B center rather than a classical reductive elimination. The reaction between the boron and the carbon atoms will close the cycle to form the final 6-member ring. We characterised both the TS and the product of this step. Figure 6-11 illustrates the molecular structures of the B-C transition state (**TS4A2**) and the product **A5**. Actually, **A5** is not the final product of the global reaction, but the product plus the catalyst, in which the π-system of the C-C double bond in the product remains coordinated with the nickel catalyst.

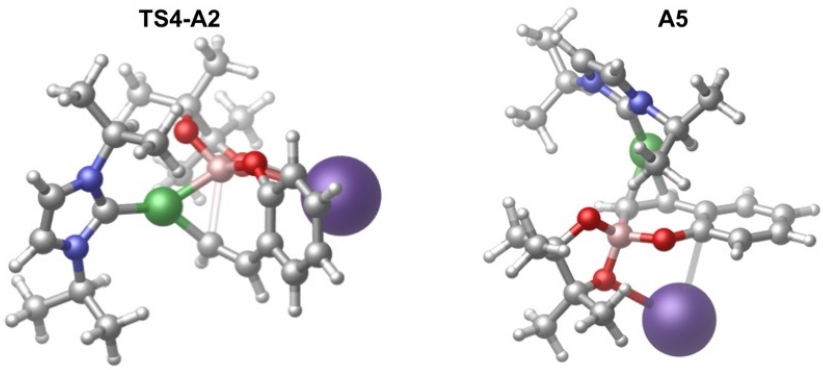

Figure 6-11. Molecular models for TS4-A2 and A5 product

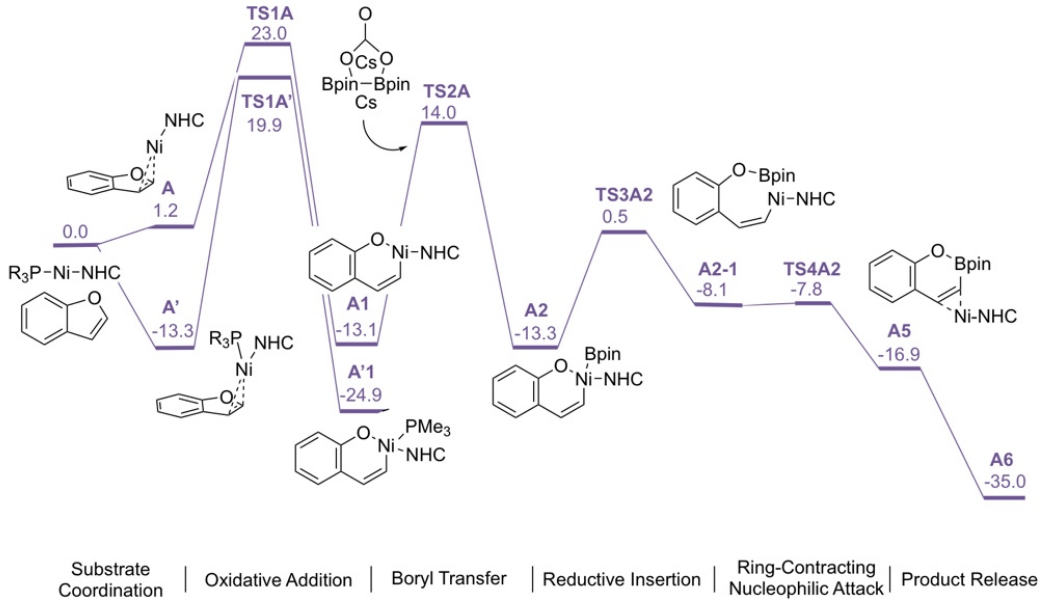

Figure 6-12. Reaction Gibbs energy profile for the whole transformation. All values in kcal·mol^{-1}.

Finally, Figure 6-12 shows the Gibbs energy profile for the whole transformation. The barrier to reach the last transition state **TS4A2** from **A2-1** is very low, and the product is more stable than the initial reactants by 16.9 kcal·mol^{-1}. The last step of the reaction is thus the decoordination of the product for recovering the catalyst which is an barrierless process with a product 35 kcal·mol^{-1} more stable than the reactants.

6.4. CONCLUSIONS

We have carried out a computational study on the mechanism of the boron insertion reaction into the C-O bond of benzofuran.[18] The results obtained have led us to propose that this reaction follows a modified cross-coupling reaction mechanism which consists of finally six steps. The first step is the formation a catalyst/substrate adduct, in which a number of C-H/π interactions between methyl groups in the catalyst and the substrate aromatic ring develop in addition to the metal-alkene bonding. Non-bonded interactions were characterised by means of

NCI maps. The Lewis base Cs_2CO_3 plays the role of B-B bond activator by forming a very stable diboron-carbonate adduct, where the two boron atoms present a pseudo-tetrahedral shape

Once the two initial adducts have been characterised, the next step is the oxidative addition. This path works with the insertion of the nickel catalyst into the C-O bond. The activation energy of this step is about 23 kcal·mol^{-1}. The performance of different DFT methods, namely, B3LYP-D3, M06-2X and ωB97XD functionals, in describing this reaction step has been investigated. We found that the M06-2X and ωB97XD functionals give less stable pre-adducts. However, for the rest of the species studied, for both intermediates and transition states, the three methods gave very similar energies.

In the classical cross-coupling reaction, transmetalation is the next step after the oxidative addition step. However, in the present case, there is no actual leaving group available. Therefore, we propose that a simple boryl transfer occurs. This addition consists in the reaction between the boron-carbonate adduct and the product of the oxidative addition. This step produces two products: the Ni-benzofuran with a boryl ligand on the nickel and the subproduct $CsBpinCO_3$. In the next step, the boron group migrates into the cycle after the boryl transfer via partial Ni(II) reduction. Our study shows that the formation of the B-C bond is slightly more favourable than the B-O bond. However, the path for migrating boron into the B-C bond would be not operative since, firstly, the stereochemistry of the intermediate that is formed directly after the oxidative addition is not correct, and secondly, if the B-C bond forms first, then the nucleophilic attack of C to B centre is unlikely to take place. Therefore, the boron gets inserted into the Ni-O bond, and the subsequent nucleophilic attack occurs with a low barrier that drives the reaction to the final product.

Regarding other substrates with C-N bonds, for instance indole, we have studied the oxidative addition step only. Indole would be more difficult to activate than benzofuran since the computed

energy barrier is larger, but still viable. The product of the oxidative addition, featuring such C-Ni-N metallacycle motif, is more stable than the corresponding isolated reactants, and is almost isoenergetic with the catalyst-substrate adduct at the present level of theory. Taking into account that the substrate is not directly involved in the boryl transfer step, and that the barriers for the boron insertion and reductive elimination steps are relatively low, the present study suggests that the borylation of indole via C-N bond cleavage should be possible.

"I am among those who think that science has great beauty."
Marie Skłodowska-Curie

CHAPTER 7

7. CONCLUSIONS

This Thesis talk about the computational study of aryl halide borylations with nickel catalysts. In the recent, years scientists have been studied how break the C-F, C-O bonds and similar for the substitution by a boryl that is better leaving group than F or O. For this reason, we decide to realize a computational study to shedding light theses process and if they have some key steps in common.

Below we summarize the most relevant conclusions for each chapter of this Thesis. A more detailed description can be found in the last section of each chapter.

7.1. Chapter 4: Ni Aryl Halide Borylation

At the Chapter 4 we have treated the study of the aryl borylation assisted by nickel catalyst studied experimentally by Ruben Martin[94]. In a first glance, we thought, as Martin group, that the reaction could follow a classic cross-coupling mechanism. However, the presence of the sodium phenolate changes the classic mechanism introducing a new participant. Additionally, the classical mechanism could be modified by the dephosphination considering the lability of the phosphine ligand.

The Martin reaction follows a Cross-coupling mechanism except for the formation of Bsp^3-Bsp^2 adduct and the presence of mono-phosphines intermediates that modify the transmetallation step that is more reachable than if it happens as a classical way. In this reaction, the participation of the sodium phenolate is essential for the activation of the diboron agent forming the mentioned Bsp^3-Bsp^2 adduct. The reaction starts with the oxidative addition path with the bis-phosphine catalyst. The next favourable step is the isomerization of the mono-phosphine compounds. Then, there is a dephosphination and then the isomerization. The following favourable step is the formation of the transmetalation pre-adduct formed by the interaction of the mono-isomerization product and the phenolate-diboron adduct. Then, the transmetalation step happens with the reaction between the diboron-phenolate adduct and the mono-phosphine intermediate. At this time, we obtain the first product of this reaction and the second intermediate composed by the boryl instead of the fluoride. As in the Cross-coupling mechanism the follow step is the reductive elimination but without previous isomerization. The reductive elimination takes place from the trans-intermediate giving the desired product and recovering the catalyst as in any catalytic cycle.

The participation of the salt sodium phenolate is key for the activation of the B-B bond of the diboron agent. Likewise, the role

of the catalyst is activate de C-F bond, that is the strongest single bond in the nature as we mentioned at the Introduction.

7.2. Chapter 5: Kinetic Study Ni Aryl Borylation

In the Chapter 5, we presented the microkinetic study of the borylation of aryl halides reaction which we determined its mechanism in the Chapter 4.

We started the study taking the results of the most favourable mechanism of the DFT study of Martin reaction[14]. The results obtained were not satisfactory and allow us to consider some aspects that affect directly to the reaction rate. We contemplated to consider the diffusion effects for the faster or barrierless bi-molecular reactions. The results obtained considering the diffusion effects are satisfactory. However, we consider other options that can affect at the system rate. We studied, also, the competitive reactions that occurs in parallel to the most favourable mechanism.

We thought that the other possible mechanisms could be competitive reaction. We considered separately the different alternative process, and we found that the process that change the rate reaction is the *cis/trans* isomerization of the intermediates. Considering these reactions, the results are in agree with Martin reaction results.

Moreover, we explored how the phosphine and sodium phenolate initial concentrations affect to the rate reaction. We obtained interesting results, because we have seen that if we decrease the phosphine initial concentration linearly, the rate reaction increases potentially. This change of concentration affects directly to the catalyst formation elemental step, as higher amount of phosphine more catalyst is formed. However, when we make the

same study for the sodium phenolate initial concentration the results showed no modifications in the rate concentration if we decrease the initial amount of sodium phenolate until its amount is lower than the limitant reactant. We thought that the reason that the phenolate is in excess is to avoid the low solubility in the solvent.

This kinetic study allowed us to understand better how can affect the different factors to the Martin reaction[94]. Kinetic analysis cannot substitute the DFT study because we need it for the rate constant calculation. However, microkinetic analysis affords additional information of the system.

7.3. Chapter 6: Ni/Cu Aryl Borylation

At Chapter 6, we have carried out the computational study of the Hosoya's reaction[15] which consist, as Martin's reaction[14], of the borylation of an aryl fluoride with Nickel catalyst. The computational study will shed in light on this reaction that, unlike Martin's reaction, have the presence of CsF that have the role of sodium phenolate in Chapter 4 and the presence of CuI, which we do not know haw role will play.

The computational analysis shows that this reaction happens as a modifies Cross-coupling mechanism with five steps. As in Chapter 4, the reaction starts as a classical Cross-coupling reaction, with the oxidative addition. At this step, the catalyst reacts with the aryl breaking the C-F bond. The only difference with Martin's reaction is the solvent, we have not observed evident differences between the use of toluene or THF in the oxidative addition. The following step that we have studied is the isomerization, where the plane-square product from the Oxidative Addition passes from *cis* conformation to trans.

The next step is the key step in the reaction because show the role that plays the copper iodine in the reaction. The copper in the presence of CsF forms the salt Cs[CuIF] and this salt reacts with the diborane compound forming the corresponding Bsp^3-Bsp^2 adduct. This adduct makes an intramolecular reaction and breaks the B-B bond and we obtain a product that have the copper linked to a boryl, and FBpin. The Cu-Bpin with the product of the isomerization forms the pre-adduct for the transmetalation step. The intramolecular reaction of this adduct we achieve the transmetalation with the exchange of the fluorine the boryl giving a stable post-adduct. We have characterized the pre-adduct, post-adduct and the TS because they are new compounds in the organometallic chemistry and know more about its bond connections. Finally, the last step is the reductive elimination, where we obtain the desired product and we recover the catalyst.

Moreover, at this chapter, we evaluate a second Hosoya's reaction of 2017, where they reproduce the reaction without nickel catalyst. As an explanation of this, they propose a mechanism with a SET. We prove this computational and we found that this mechanism is far to be possible. After the computational analysis, we found that the reaction could happen by the formation of a Cu^I compound after the break of B-B bond. This compound reacts with the aryl halide and gives the desired product.

Chapter 7 reaffirms the need of a salt for the activation of B-B bond. Moreover, the participation of copper could act as a co-catalyst with nickel making the reaction reachable. Additionally, we have demonstrated that with the participation of copper the nickel is not needed.

7.4. Chapter 7: C-O benzofuran Boron Insertion

At Chapter 7, we have carried out a computational study on the mechanism of the boron insertion reaction into the C-O bond of benzofuran, a reaction that was introduced by Yorimitsu and coworkers.[18] The results obtained have led us to propose that this reaction follows a modified cross-coupling reaction mechanism which consists of seven steps. The first step is the formation of a diboron/carbonate adduct. The Lewis base plays the role of B-B bond activator by forming a very stable diboron-carbonate adduct, where the two boron atoms present a pseudo-tetrahedral shape. Before the oxidative addition step takes place, the catalyst and the substrate form an especially stable species, in which a number of C-H-π interactions between methyl groups in the catalyst and the substrate aromatic ring develop in addition to the metal-alkene bonding. Non-bonded interactions were characterised by means of NCI maps.

Once the two initial adducts have been characterised, the next step is the oxidative addition. This path works with the insertion of the nickel catalyst into the C-O bond. The activation energy of this step is about 23 kcal·mol^{-1}. The performance of different DFT methods, namely, B3LYP-D3, M06-2X and ωB97XD functionals, in describing this reaction state has been investigated. We found that the M06-2X and ωB97XD functionals give less stable pre-adducts. However, for the rest of the species studied, for both intermediates and transition states, the three methods gave very similar energies.

In the classical cross-coupling reaction, transmetalation is the next step after the oxidative addition step. However, in the present case, there is no leaving group available. Therefore, we propose that a direct boryl addition occurs. This addition consists in the reaction between the borane-carbonate adduct and the product of the oxidative addition. This step produces two products: the Ni-benzofuran with a boryl ligand on the nickel and the subproduct

$CsBpinCO_3$. In the next step, the boron atom is inserted into the cycle after the boryl addition. Our study shows that the formation of the B-C bond is slightly more favourable than the B-O bond. However, the path for inserting boron into the B-C bond would be not operative since, firstly, the stereochemistry of the intermediate that is formed directly after the oxidative addition is not correct, and secondly, if the B-C bond forms first, then the reductive elimination does not take place. Therefore, the boron gets inserted into the B-O bond, and the subsequent reactive elimination occurs with a low barrier that drives the reaction to the final product.

Regarding other substrates with C-N bonds, for instance benzopirrole, we have studied the reactive addition step only. Benzopirrole would be more difficult to activate than benzofurane since the computed energy barrier is larger, but still viable. The product of the oxidative addition, featuring such C-Ni-N metalacycle motif, is more stable than the corresponding isolated reactants, and is almost isoenergetic with the catalyst-substrate adduct at the present level of theory. Taking into account that the substrate is not directly involved in the boryl addition step, and that the barriers for the boron insertion and reductive elimination steps are relatively low, the present study suggests that the borylation of benzopyrrole via C-N bond cleavage should be possible.

REFERENCES

(1) Dolbier, W. R. Fluorine Chemistry at the Millennium. https://doi.org/10.1016/j.jfluchem.2004.09.033.

(2) Mesganaw, T.; Garg, N. K. Ni- and Fe-Catalyzed Cross-Coupling Reactions of Phenol Derivatives. *Org. Process Res. Dev.* **2013**, *17* (1), 29–39. https://doi.org/10.1021/op300236f.

(3) Yamaguchi, J.; Muto, K.; Itami, K. Recent Progress in Nickel-Catalyzed Biaryl Coupling. *European J. Org. Chem.* **2013**, *2013* (1), 19–30. https://doi.org/10.1002/ejoc.201200914.

(4) Correa, A.; Cornella, J.; Martin, R. Nickel-Catalyzed Decarbonylative C-H Coupling Reactions: A Strategy for Preparing Bis(Heteroaryl) Backbones. *Angew. Chemie Int. Ed.* **2013**, *52* (7), 1878–1880. https://doi.org/10.1002/anie.201208843.

(5) Tobisu, M.; Chatani, N. Catalytic Transformations Involving the Activation of Sp2 Carbon–Oxygen Bonds; Springer, Berlin, Heidelberg, 2012; pp 35–53. https://doi.org/10.1007/3418_2012_42.

(6) Rosen, B. M.; Quasdorf, K. W.; Wilson, D. A.; Zhang, N.; Resmerita, A.-M.; Garg, N. K.; Percec, V. Nickel-Catalyzed Cross-Couplings Involving Carbon−Oxygen Bonds. *Chem. Rev.* **2011**, *111* (3), 1346–1416. https://doi.org/10.1021/cr100259t.

(7) Li, B.-J.; Yu, D.-G.; Sun, C.-L.; Shi, Z.-J. Activation of "Inert" Alkenyl/Aryl C-O Bond and Its Application in Cross-Coupling Reactions. *Chem. - A Eur. J.* **2011**, *17* (6), 1728–1759. https://doi.org/10.1002/chem.201002273.

(8) Yu, D.-G.; Li, B.-J.; Shi, Z.-J. Exploration of New C−O Electrophiles in Cross-Coupling Reactions. *Acc. Chem. Res.* **2010**, *43* (12), 1486–1495. https://doi.org/10.1021/ar100082d.

(9) Cornella, J.; Gomez-Bengoa, E.; Martin, R. Combined Experimental and Theoretical Study on the Reductive Cleavage of Inert C-O Bonds with Silanes: Ruling out a Classical Ni(0)/Ni(II) Catalytic Couple and Evidence for Ni(I)

Intermediates. *J. Am. Chem. Soc.* **2013**, *135* (5), 1997–2009. https://doi.org/10.1021/ja311940s.

(10) Hall, D. Boronic Acids Volume 2 Preparation and Applications in Organic Synthesis, Medicine and Materials Second Completely Revised Edition Preface. In *Boronic Acids, Vol 2: Preparation and Applications in Organic Synthesis, Medicine and Materials, 2nd Edition*; Hall, D. G., Ed.; Wiley-V C H Verlag Gmbh: Univ Alberta, Dept Chem, Centennial Ctr Interdisciplinary Sci 4 010, Edmonton, AB T6G 2G2, Canada. Hall, D (reprint author), Univ Alberta, Dept Chem, Centennial Ctr Interdisciplinary Sci 4 010, Edmonton, AB T6G 2G2, Canada., 2011; pp XV–XVII.

(11) Miyaura, N.; Yamada, K.; Suzuki, A. A New Stereospecific Cross-Coupling by the Palladium-Catalyzed Reaction of 1-Alkenylboranes with 1-Alkenyl or 1-Alkynyl Halides. *Tetrahedron Lett.* **1979**, *20* (36), 3437–3440.

(12) Educafreechemistry. Suzuki-Miyaura Reaction https://commons.wikimedia.org/wiki/File:Mechanism_of_Suzuki_coupling_reaction.png.

(13) Council, N. R. *The Role of the Chemical Sciences in Finding Alternatives to Critical Resources*; National Academies Press: Washington, D.C., 2012. https://doi.org/10.17226/13366.

(14) Liu, X.-W.; Echavarren, J.; Zarate, C.; Martin, R. Ni-Catalyzed Borylation of Aryl Fluorides via C-F Cleavage. *J. Am. Chem. Soc.* **2015**, *137* (39), 12470–12473. https://doi.org/10.1021/jacs.5b08103.

(15) Niwa, T.; Ochiai, H.; Watanabe, Y.; Hosoya, T. Ni/Cu-Catalyzed Defluoroborylation of Fluoroarenes for Diverse C-F Bond Functionalizations. *J. Am. Chem. Soc.* **2015**, *137* (45), 14313–14318. https://doi.org/10.1021/jacs.5b10119.

(16) Zhou, J.; Kuntze-Fechner, M. W.; Bertermann, R.; Paul, U. S. D.; Berthel, J. H. J.; Friedrich, A.; Du, Z. T.; Marder, T. B.; Radius, U. Preparing (Multi)Fluoroarenes as Building Blocks for Synthesis: Nickel-Catalyzed Borylation of Polyfluoroarenes via C-F Bond Cleavage. *J. Am. Chem. Soc.* **2016**, *138* (16), 5250–5253. https://doi.org/10.1021/jacs.6b02337.

(17) Zarate, C.; Manzano, R.; Martin, R. *Ipso*- Borylation of Aryl Ethers via Ni-Catalyzed C–OMe Cleavage. *J. Am. Chem. Soc.* **2015**, *137* (21), 6754–6757. https://doi.org/10.1021/jacs.5b03955.

(18) Saito, H.; Otsuka, S.; Nogi, K.; Yorimitsu, H. Nickel-Catalyzed Boron Insertion into the C2–O Bond of Benzofurans. *J. Am. Chem. Soc.* **2016**, *138* (47), 15315–15318. https://doi.org/10.1021/jacs.6b10255.

(19) Niwa, T.; Ochiai, H.; Hosoya, T. Copper-Catalyzed Ipso-Borylation of Fluoroarenes. *ACS Catal.* **2017**, *7* (7), 4535–4541. https://doi.org/10.1021/acscatal.7b01448.

(20) Sakaguchi, H.; Uetake, Y.; Ohashi, M.; Niwa, T.; Ogoshi, S.; Hosoya, T. Copper-Catalyzed Regioselective Monodefluoroborylation of Polyfluoroalkenes En Route to Diverse Fluoroalkenes. *J. Am. Chem. Soc.* **2017**, *139* (36), 12855–12862. https://doi.org/10.1021/jacs.7b08343.

(21) Zhang, J.; Dai, W.; Liu, Q.; Cao, S. Cu-Catalyzed Stereoselective Borylation of Gem -Difluoroalkenes with B 2 Pin 2. *Org. Lett.* **2017**, *19* (12), 3283–3286. https://doi.org/10.1021/acs.orglett.7b01430.

(22) Ogawa, H.; Minami, H.; Ozaki, T.; Komagawa, S.; Wang, C.; Uchiyama, M. How and Why Does Ni 0 Promote Smooth Etheric C-O Bond Cleavage and C-C Bond Formation? A Theoretical Study. *Chem. - A Eur. J.* **2015**, *21* (40), 13904–13908. https://doi.org/10.1002/chem.201502114.

(23) Xu, L.; Chung, L. W.; Wu, Y.-D. Mechanism of Ni-NHC Catalyzed Hydrogenolysis of Aryl Ethers: Roles of the Excess Base. *ACS Catal.* **2016**, *6* (1), 483–493. https://doi.org/10.1021/acscatal.5b02089.

(24) Wititsuwannakul, T.; Tantirungrotechai, Y.; Surawatanawong, P. Density Functional Study of Nickel N-Heterocyclic Carbene Catalyzed C-O Bond Hydrogenolysis of Methyl Phenyl Ether: The Concerted β-H Transfer Mechanism. *ACS Catal.* **2016**, *6* (3), 1477–1486. https://doi.org/10.1021/acscatal.5b02058.

(25) Liu, X.; Hsiao, C.-C.; Kalvet, I.; Leiendecker, M.; Guo, L.; Schoenebeck, F.; Rueping, M. Lewis Acid Assisted Nickel-Catalyzed Cross-Coupling of Aryl Methyl Ethers by C−O Bond-Cleaving Alkylation: Prevention of Undesired β-Hydride Elimination. *Angew. Chemie Int. Ed.* **2016**, *55* (20), 6093–6098. https://doi.org/10.1002/anie.201510497.

(26) Kelley, P.; Edouard, G. A.; Lin, S.; Agapie, T. Lewis Acid Accelerated Aryl Ether Bond Cleavage with Nickel: Orders of Magnitude Rate Enhancement Using $AlMe_3$. *Chem. - A Eur. J.* **2016**, *22* (48), 17173–17176. https://doi.org/10.1002/chem.201604160.

(27) Wang, B.; Zhang, Q.; Jiang, J.; Yu, H.; Fu, Y. Mechanistic Study on Nickel-Catalyzed Silylation of Aryl Methyl Ethers. *Chem. - A Eur. J.* **2017**, *23* (68), 17249–17256. https://doi.org/10.1002/chem.201703266.

(28) Jain, A.; Ong, S. P.; Chen, W.; Medasani, B.; Qu, X.; Kocher, M.; Brafman, M.; Petretto, G.; Rignanese, G.-M.; Hautier, G.; et al. FireWorks: A Dynamic Workflow System Designed for High-Throughput Applications. *Concurr. Comput. Pract. Exp.* **2015**, *27* (17), 5037–5059. https://doi.org/10.1002/cpe.3505.

(29) Schwarzer, M. C.; Konno, R.; Hojo, T.; Ohtsuki, A.; Nakamura, K.; Yasutome, A.; Takahashi, H.; Shimasaki, T.; Tobisu, M.; Chatani, N.; et al. Combined Theoretical and Experimental Studies of Nickel-Catalyzed Cross-Coupling of Methoxyarenes with Arylboronic Esters via C–O Bond Cleavage. *J. Am. Chem. Soc.* **2017**, *139* (30), 10347–10358. https://doi.org/10.1021/jacs.7b04279.

(30) Lee, Y.; Baek, S. Y.; Park, J.; Kim, S. T.; Tussupbayev, S.; Kim, J.; Baik, M. H.; Cho, S. H. Chemoselective Coupling of 1,1-Bis[(Pinacolato)Boryl]Alkanes for the Transition-Metal-Frec Borylation of Aryl and Vinyl Halides: A Combined Experimental and Theoretical Investigation. *J. Am. Chem. Soc.* **2017**, *139* (2), 975–984. https://doi.org/10.1021/jacs.6b11757.

(31) Lim, S.; Song, D.; Jeon, S.; Kim, Y.; Kim, H.; Lee, S.; Cho, H.; Lee, B. C.; Kim, S. E.; Kim, K.; et al. Cobalt-Catalyzed C–F Bond Borylation of Aryl Fluorides. *Org. Lett.* **2018**, *20* (22), 7249–7252. https://doi.org/10.1021/acs.orglett.8b03167.

(32) Minami, H.; Otsuka, S.; Nogi, K.; Yorimitsu, H. Palladium-Catalyzed Borylation of Aryl Sulfoniums with Diborons. *ACS Catal.* **2018**, *8* (1), 579–583. https://doi.org/10.1021/acscatal.7b03841.

(33) Verma, P. K.; Mandal, S.; Geetharani, K. Efficient Synthesis of Aryl Boronates via Cobalt-Catalyzed Borylation of Aryl Chlorides and Bromides. *ACS Catal.* **2018**, *8* (5), 4049–4054. https://doi.org/10.1021/acscatal.8b00536.

(34) Kuehn, L.; Jammal, D. G.; Lubitz, K.; Marder, T. B.; Radius, U. Stoichiometric and Catalytic Aryl-Cl Activation and Borylation Using NHC-Stabilized Nickel(0) Complexes. *Chem. - A Eur. J.* **2019**. https://doi.org/10.1002/chem.201900937.

(35) Lu, X.; Zhang, Z.; Yu, L.; Zhang, B.; Wang, B.; Gong, T.; Tian, C.; Xiao, B.; Fu, Y. Free Radical Pathway Cleavage of C—O Bonds for the Synthesis of Alkylboron Compounds. *Chinese J.*

Chem. **2019**, *37* (1), 11–18. https://doi.org/10.1002/cjoc.201800500.

(36) Besora, M.; Maseras, F. Microkinetic Modeling in Homogeneous Catalysis. *Wiley Interdiscip. Rev. Comput. Mol. Sci.* **2018**, *8* (6), e1372. https://doi.org/10.1002/wcms.1372.

(37) van Leeuwen, P. W. N. M. *Homogeneous Catalysis Understanding Art*; 2004; Vol. 30. https://doi.org/10.2307/1320653.

(38) File:Potential Energy Surface and Corresponding Reaction Coordinate Diagram.png - Wikimedia Commons https://commons.wikimedia.org/wiki/File:Potential_Energy_Surface_and_Corresponding_Reaction_Coordinate_Diagram.png (accessed Jul 23, 2019).

(39) Koch, W.; Holthausen, M. C. *A Chemist's Guide to Density Functional Theory*; Wiley, 2001. https://doi.org/10.1002/3527600043.

(40) Hohenberg, P.; Kohn, W. Inhomogeneous Electron Gas. *Phys. Rev.* **1964**, *136* (3B), B864–B871. https://doi.org/10.1103/PhysRev.136.B864.

(41) Kohn, W.; Sham, L. J. Self-Consistent Equations Including Exchange and Correlation Effects. *Phys. Rev.* **1965**, *140* (4A), A1133–A1138. https://doi.org/10.1103/PhysRev.140.A1133.

(42) Becke, A. D. Density-functional Thermochemistry. III. The Role of Exact Exchange. *J. Chem. Phys.* **1993**, *98* (7), 5648–5652. https://doi.org/10.1063/1.464913.

(43) Becke, A. D. A New Mixing of Hartree–Fock and Local Density-functional Theories. *J. Chem. Phys.* **1993**, *98* (2), 1372–1377. https://doi.org/10.1063/1.464304.

(44) Becke, A. D. Density-Functional Exchange-Energy Approximation with Correct Asymptotic Behavior. *Phys. Rev. A* **1988**, *38* (6), 3098–3100. https://doi.org/10.1103/PhysRevA.38.3098.

(45) Chai, J. D.; Head-Gordon, M. Long-Range Corrected Hybrid Density Functionals with Damped Atom-Atom Dispersion Corrections. *Phys. Chem. Chem. Phys.* **2008**, *10* (44), 6615–6620. https://doi.org/10.1039/b810189b.

(46) Miertuš, S.; Scrocco, E.; Tomasi, J. Electrostatic Interaction of a Solute with a Continuum. A Direct Utilizaion of AB Initio

Molecular Potentials for the Prevision of Solvent Effects. *Chem. Phys.* **1981**, *55* (1), 117–129. https://doi.org/10.1016/0301-0104(81)85090-2.

(47) Marenich, A. V; Cramer, C. J.; Truhlar, D. G. Universal Solvation Model Based on Solute Electron Density and on a Continuum Model of the Solvent Defined by the Bulk Dielectric Constant and Atomic Surface Tensions. *J. Phys. Chem. B* **2009**, *113* (18), 6378–6396. https://doi.org/10.1021/jp810292n.

(48) Bader, R. F. W. *Atoms in Molecules : A Quantum Theory*; Clarendon Press, 1990.

(49) Johnson, E. R.; Keinan, S.; Mori-Sánchez, P.; Contreras-García, J.; Cohen, A. J.; Yang, W. Revealing Noncovalent Interactions. *J. Am. Chem. Soc.* **2010**, *132* (18), 6498–6506. https://doi.org/10.1021/ja100936w.

(50) Mulliken, R. S. Electronic Population Analysis on LCAO–MO Molecular Wave Functions. I. *J. Chem. Phys.* **1955**, *23* (10), 1833–1840. https://doi.org/10.1063/1.1740588.

(51) Weinhold, F.; Landis, C. R. Natural Bond Orbitals and Extensions of Localized Bonding Concepts. *Chem. Educ. Res. Pr.* **2001**, *2* (2), 91–104. https://doi.org/10.1039/B1RP90011K.

(52) Von Smoluchowski, M. Mathematical Theory of the Kinetics of the Coagulation of Colloidal Solutions. *Z. Phys. Chem* **1917**, *92*, 129–168.

(53) D'hooge, D. R.; Reyniers, M.-F.; Marin, G. B. The Crucial Role of Diffusional Limitations in Controlled Radical Polymerization. *Macromol. React. Eng.* **2013**, *7* (8), 362–379. https://doi.org/10.1002/mren.201300006.

(54) D'Hooge, D. R.; Van Steenberge, P. H. M.; Reyniers, M. F.; Marin, G. B. The Strength of Multi-Scale Modeling to Unveil the Complexity of Radical Polymerization. *Prog. Polym. Sci.* **2016**, *58*, 59–89. https://doi.org/10.1016/j.progpolymsci.2016.04.002.

(55) Bentein, L.; D'hooge, D. R.; Reyniers, M.-F.; Marin, G. B. Kinetic Modeling as a Tool to Understand and Improve the Nitroxide Mediated Polymerization of Styrene. *Macromol. Theory Simulations* **2011**, *20* (4), 238–265. https://doi.org/10.1002/mats.201000081.

(56) Desmet, G. B.; D'Hooge, D. R.; Omurtag, P. S.; Espeel, P.;

Marin, G. B.; Du Prez, F. E.; Reyniers, M. F. Quantitative First-Principles Kinetic Modeling of the Aza-Michael Addition to Acrylates in Polar Aprotic Solvents. *J. Org. Chem.* **2016**, *81* (24), 12291–12302. https://doi.org/10.1021/acs.joc.6b02218.

(57) Wachsstock, D. Tenua: The Kinetics Simulator for Java. 2007.

(58) Hoops, S.; Sahle, S.; Gauges, R.; Lee, C.; Pahle, J.; Simus, N.; Singhal, M.; Xu, L.; Mendes, P.; Kummer, U. COPASI--a COmplex PAthway SImulator. *Bioinformatics* **2006**, *22* (24), 3067–3074. https://doi.org/10.1093/bioinformatics/btl485.

(59) Martínez-Núñez, E. An Automated Method to Find Transition States Using Chemical Dynamics Simulations. *J. Comput. Chem.* **2015**, *36* (4), 222–234. https://doi.org/10.1002/jcc.23790.

(60) Sameera, W. M. C.; Maeda, S.; Morokuma, K. Computational Catalysis Using the Artificial Force Induced Reaction Method. *Acc. Chem. Res.* **2016**, *49* (4), 763–773. https://doi.org/10.1021/acs.accounts.6b00023.

(61) Dewyer, A. L.; Zimmerman, P. M. Finding Reaction Mechanisms, Intuitive or Otherwise. *Org. Biomol. Chem.* **2017**, *15* (3), 501–504. https://doi.org/10.1039/C6OB02183B.

(62) Guan, Y.; Ingman, V. M.; Rooks, B. J.; Wheeler, S. E. AARON: An Automated Reaction Optimizer for New Catalysts. *J. Chem. Theory Comput.* **2018**, *14* (10), 5249–5261. https://doi.org/10.1021/acs.jctc.8b00578.

(63) Shi, Z. J. *Homogeneous Catalysis for Unreactive Bond Activation*; Wiley, 2014.

(64) Wang, J.; Sanchez-Rosello, M.; Acena, J. L.; del Pozo, C.; Sorochinsky, A. E.; Fustero, S.; Soloshonok, V. A.; Liu, H. Fluorine in Pharmaceutical Industry: Fluorine-Containing Drugs Introduced to the Market in the Last Decade (2001-2011). *Chem. Rev.* **2014**, *114* (4), 2432–2506. https://doi.org/10.1021/cr4002879.

(65) Zhou, J.; Kuntze-Fechner, M. W.; Bertermann, R.; Paul, U. S. D.; Berthel, J. H. J.; Friedrich, A.; Du, Z.; Marder, T. B.; Radius, U. Preparing (Multi)Fluoroarenes as Building Blocks for Synthesis: Nickel-Catalyzed Borylation of Polyfluoroarenes via C–F Bond Cleavage. *J. Am. Chem. Soc.* **2016**, *138* (16), 5250–5253. https://doi.org/10.1021/jacs.6b02337.

(66) Frisch, M. J.; Trucks, G. W.; Schlegel, H. B.; Scuseria, G. E.; Robb, M. A.; Cheeseman, J. R.; Scalmani, G.; Barone, V.; Petersson, G. A.; Nakatsuji, H.; et al. Gaussian 09, Revision D.01. Gaussian Inc.: Wallingford CT 2016.

(67) Schuchardt, K. L.; Didier, B. T.; Elsethagen, T.; Sun, L. S.; Gurumoorthi, V.; Chase, J.; Li, J.; Windus, T. L. Basis Set Exchange: A Community Database for Computational Sciences. *J. Chem. Inf. Model.* **2007**, *47* (3), 1045–1052. https://doi.org/10.1021/ci600510j.

(68) Zhao, Y.; Schultz, N. E.; Truhlar, D. G. Design of Density Functionals by Combining the Method of Constraint Satisfaction with Parametrization for Thermochemistry, Thermochemical Kinetics, and Noncovalent Interactions. *J. Chem. Theory Comput.* **2006**, *2* (2), 364–382. https://doi.org/10.1021/ct0502763.

(69) Lee, C. T.; Yang, W. T.; Parr, R. G. Development of the Colle-Salvetti Correlation-Energy Formula into a Functional of the Electron Density. *Phys. Rev. B* **1988**, *37* (2), 785–789. https://doi.org/10.1103/PhysRevB.37.785.

(70) Grimme, S.; Antony, J.; Ehrlich, S.; Krieg, H. A Consistent and Accurate Ab Initio Parametrization of Density Functional Dispersion Correction (DFT-D) for the 94 Elements H-Pu. *J. Chem. Phys.* **2010**, *132* (15), 19. https://doi.org/10.1063/1.3382344.

(71) Martin, R. L.; Hay, P. J.; Pratt, L. R. Hydrolysis of Ferric Ion in Water and Conformational Equilibrium. **1998**. https://doi.org/10.1021/JP980229P.

(72) Álvarez-Moreno, M.; de Graaf, C.; López, N.; Maseras, F.; Poblet, J. M.; Bo, C. Managing the Computational Chemistry Big Data Problem: The **IoChem-BD** Platform. *J. Chem. Inf. Model.* **2015**, *55* (1), 95–103. https://doi.org/10.1021/ci500593j.

(73) Taube, H. Rates and Mechanisms of Substitution in Inorganic Complexes in Solution. *Chem. Rev.* **1952**, *50* (1), 69–126. https://doi.org/10.1021/cr60155a003.

(74) Bonet, A.; Pubill-Ulldemolins, C.; Bo, C.; Gulyas, H.; Fernandez, E. Transition-Metal-Free Diboration Reaction by Activation of Diboron Compounds with Simple Lewis Bases. *Angew. Chemie-International Ed.* **2011**, *50* (31), 7158–7161. https://doi.org/10.1002/anie.201101941.

(75) Wu, H.; Garcia, J. M.; Haeffner, F.; Radomkit, S.; Zhugralin, A. R.; Hoveyda, A. H. Mechanism of NHC-Catalyzed Conjugate Additions of Diboron and Borosilane Reagents to Alpha,Beta-Unsaturated Carbonyl Compounds. *J. Am. Chem. Soc.* **2015**, *137* (33), 10585–10602. https://doi.org/10.1021/jacs.5b06745.

(76) Farre, A.; Soares, K.; Briggs, R. A.; Balanta, A.; Benoit, D. M.; Bonet, A. Amine Catalysis for the Organocatalytic Diboration of Challenging Alkenes. *Chem. Eur. J.* **2016**, *22* (49), 17552–17556. https://doi.org/10.1002/chem.201603979.

(77) Fernández, E.; Whiting, A. *Synthesis and Application of Organoboron Compounds*; Fernández, E., Whiting, A., Eds.; Topics in Organometallic Chemistry; Springer International Publishing: Cham, 2015; Vol. 49. https://doi.org/10.1007/978-3-319-13054-5.

(78) Pietsch, S.; Neeve, E. C.; Apperley, D. C.; Bertermann, R.; Mo, F. Y.; Qiu, D.; Cheung, M. S.; Dang, L.; Wang, J. B.; Radius, U.; et al. Synthesis, Structure, and Reactivity of Anionic Sp(2)-Sp(3) Diboron Compounds: Readily Accessible Boryl Nucleophiles. *Chem. Eur. J.* **2015**, *21* (19), 7082–7098. https://doi.org/10.1002/chem.201500235.

(79) Chen, P.-P.; Cheng, F.; Cheng, B.; Zhang, S.-Q.; Lu, Z.; Meng, F.; Hong, X. How Solvent Controls the Stereospecificity of Ni-Catalyzed Miyaura Borylation of Allylic Pivalates. *ACS Catal.* **2019**.

(80) Sperger, T.; Sanhueza, I. A.; Kalvet, I.; Schoenebeck, F. Computational Studies of Synthetically Relevant Homogeneous Organometallic Catalysis Involving Ni, Pd, Ir, and Rh: An Overview of Commonly Employed DFT Methods and Mechanistic Insights. *Chem. Rev.* **2015**, *115* (17), 9532–9586. https://doi.org/10.1021/acs.chemrev.5b00163.

(81) Alvarez-Moreno, M.; de Graaf, C.; Lopez, N.; Maseras, F.; Poblet, J. M.; Bo, C. Managing the Computational Chemistry Big Data Problem: The IoChem-BD Platform. *J. Chem. Inf. Model.* **2015**, *55* (1), 95–103. https://doi.org/10.1021/ci500593j.

(82) Lewars, E. *Computational Chemistry : Introduction to the Theory and Applications of Molecular and Quantum Mechanics*; Springer, 2011.

(83) Pérez, P. J.; Braga, A. A. C.; Urbano, J.; Sameera, W. M. C.; Maseras, F.; Fructos, M. R.; Besora, M. A Computational View

on the Reactions of Hydrocarbons with Coinage Metal Complexes. *J. Organomet. Chem.* **2014**, *784*, 2–12. https://doi.org/10.1016/j.jorganchem.2014.10.009.

(84) Fructos, M. R.; Besora, M.; Braga, A. A. C.; Díaz-Requejo, M. M.; Maseras, F.; Pérez, P. J. Mechanistic Studies on Gold-Catalyzed Direct Arene C–H Bond Functionalization by Carbene Insertion: The Coinage-Metal Effect. *Organometallics* **2017**, *36* (1), 172–179. https://doi.org/10.1021/acs.organomet.6b00604.

(85) Gava, R.; Fuentes, M. Á.; Besora, M.; Belderrain, T. R.; Jacob, K.; Maseras, F.; Etienne, M.; Caballero, A.; Pérez, P. J. Silver-Catalyzed Functionalization of Esters by Carbene Transfer: The Role of Ylide Zwitterionic Intermediates. *ChemCatChem* **2014**, *6* (8), 2206–2210. https://doi.org/10.1002/cctc.201402241.

(86) Hartenbach, A. E.; Hofstetter, T. B.; Aeschbacher, M.; Sander, M.; Kim, D.; Strathmann, T. J.; Arnold, W. A.; Cramer, C. J.; Schwarzenbach, R. P. Variability of Nitrogen Isotope Fractionation during the Reduction of Nitroaromatic Compounds with Dissolved Reductants. *Environ. Sci. Technol.* **2008**, *42* (22), 8352–8359. https://doi.org/10.1021/es801063u.

(87) Kelly, C. P.; Cramer, C. J.; Truhlar, D. G. Aqueous Solvation Free Energies of Ions and Ion−Water Clusters Based on an Accurate Value for the Absolute Aqueous Solvation Free Energy of the Proton. *J. Phys. Chem. B* **2006**, *110* (32), 16066–16081. https://doi.org/10.1021/jp063552y.

(88) Michalak, A.; Ziegler, T. Stochastic Simulations of Polymer Growth and Isomerization in the Polymerization of Propylene Catalyzed by Pd-Based Diimine Catalysts. *J. Am. Chem. Soc.* **2002**, *124* (25), 7519–7528. https://doi.org/10.1021/ja012144z.

(89) Olson, E. J.; Isley, W. C.; Brennan, J. E.; Cramer, C. J.; Bühlmann, P. Electrochemical Reduction of 2,4-Dinitrotoluene in Aprotic and PH-Buffered Media. *J. Phys. Chem. C* **2015**, *119* (23), 13088–13097. https://doi.org/10.1021/acs.jpcc.5b02840.

(90) Fernández-Alvarez, V. M.; Nappi, M.; Melchiorre, P.; Maseras, F. Computational Study with DFT and Kinetic Models on the Mechanism of Photoinitiated Aromatic Perfluoroalkylations. *Org. Lett.* **2015**, *17* (11), 2676–2679. https://doi.org/10.1021/acs.orglett.5b01069.

(91) Kefalidis, C. E.; Davi, M.; Holstein, P. M.; Clot, E.; Baudoin, O. Mechanistic Study of the Selectivity of Olefin versus Cyclobutene Formation by Palladium(0)-Catalyzed Intramolecular C(Sp^3)–H Activation. *J. Org. Chem.* **2014**, *79* (24), 11903–11910. https://doi.org/10.1021/jo501610x.

(92) Wei, D.; Roisnel, T.; Darcel, C.; Clot, E.; Sortais, J.-B. Hydrogenation of Carbonyl Derivatives with a Well-Defined Rhenium Precatalyst. *ChemCatChem* **2017**, *9* (1), 80–83. https://doi.org/10.1002/cctc.201601141.

(93) Funes-Ardoiz, I.; Nelson, D. J.; Maseras, F. Halide Abstraction Competes with Oxidative Addition in the Reactions of Aryl Halides with [$Ni(PMe_n Ph_{(3-n)})_4$]. *Chem. - A Eur. J.* **2017**, *23* (66), 16728–16733. https://doi.org/10.1002/chem.201702331.

(94) Liu, X.-W.; Echavarren, J.; Zarate, C.; Martin, R. Ni-Catalyzed Borylation of Aryl Fluorides via C–F Cleavage. *J. Am. Chem. Soc.* **2015**, *137* (39), 12470–12473. https://doi.org/10.1021/jacs.5b08103.

(95) Eyring, H. The Activated Complex in Chemical Reactions. *J. Chem. Phys.* **1935**, *3*, 107. https://doi.org/10.1063/1.1749604.

(96) Donnell, P.; Banaji, M.; Marginean, A.; Pantea, C. CoNtRol: An Open Source Framework for the Analysis of Chemical Reaction Networks. *Bioinformatics* **2014**, *30* (11), 1633–1634. https://doi.org/10.1093/bioinformatics/btu063.

(97) Massey, A. G.; Johnson, B. F. G. G.; Thompson, N. R. *The Chemistry of Copper*.

(98) Casitas, A.; Ribas, X. The Role of Organometallic Copper(Iii) Complexes in Homogeneous Catalysis. *Chem. Sci.* **2013**, *4* (6), 2301–2318. https://doi.org/10.1039/c3sc21818j.

(99) Ni, N. T.; Wang, B. H. Applications of Boronic Acids in Chemical Biology and Medicinal Chemistry. *Boronic Acids* **2011**, 591–620. https://doi.org/10.1002/9783527639328.ch13.

(100) The Overstabilisation Could Arise from the Basis Set Superposition Error (BSSE), Which Can Be Easily Quantified Using the Counter-Poise Method. This Calculation Gives a Quite Large BSSE of 17.4 $kcal \cdot mol^{-1}$.

(101) Dang, L.; Lin, Z.; Marder, T. B. Boryl Ligands and Their Roles in Metal-Catalysed Borylation Reactions. *Chem. Commun.*

2009, *0* (27), 3987. https://doi.org/10.1039/b903098k.

UNIVERSITAT
ROVIRA i VIRGILI